Complexity reduction of fluid-structure systems at low forcing frequencies

Thesis by

Maysam Shamai

In Partial Fulfillment of the Requirements for the
Degree of
Doctor of Philosophy in Aeronautics

CALIFORNIA INSTITUTE OF TECHNOLOGY
Pasadena, California

2021
Defended May 6, 2021

Maysam Shamai
ORCID: 0000-0002-1099-1456

Dedicated to my parents and sister

ACKNOWLEDGEMENTS

"...A fragrant clump of dirt
was handed to me by a friend one day

I asked it, 'Are you musk or perfume?
As I find your fragrance intoxicating.'

It replied, 'I was a worthless handful of dirt
But for a while I sat with flowers

And their essence affected me
Otherwise, I would still be the same clump of dirt."

- Saadi, 13th century Persian poet

Before starting my graduate studies at Caltech, I knew I would come across many brilliant individuals. Indeed I was not let down, but what really surprised me was the care and compassion each one of them placed in everything they do. I will try to acknowledge some of those people here but hope that anyone I forget forgives the oversight.

The first person I would like to thank is my advisor, Beverley McKeon. For good reason, it has become an ongoing saying among her students, including myself, that most of our conversations in the group office end with us expressing how grateful we are to have her as our advisor. Not only did she provide extremely insightful scientific guidance related to my research, but the example she set as a leader was always just as inspiring. I am certain that my experience at Caltech would not be nearly as productive and memorable were it not for her guidance and mentorship, and I am forever grateful for that.

Next, I would like to thank the members of my thesis committee: Mory Gharib, Tony Leonard, and Mike Plesniak. I am very appreciative for all of their excellent comments and advice that proved invaluable in shaping this work. On numerous occasions, they provided profound input that helped me advance the work.

Beyond my thesis committee, I would like to thank Mike Plesniak and Ian Carr for their collaboration on the surface mounted hemisphere project. They graciously provided us with the datasets that enabled the work in Chapter 5 of this thesis.

Furthermore, they provided valuable guidance and expertise that helped shape the resulting analysis.

Two additional individuals who merit thanks are Alex Techet and Shai Revzen. I was pleased to have had the opportunity to collaborate with Alex regarding vortex dynamics in the oscillating cylinder's wake. Were it not for her expert eye, we would have had a much harder time analyzing the system. Similarly, Shai asked a simple, yet insightful question during one of the MURI reviews that sparked an interesting line of research regarding quasi-steady analysis of the oscillating cylinder's wake. In addition, I want to thank Scott Dawson and Igor Mezić for their collaboration and input on the quasi-steady time scaling analysis and the resulting publication.

Within Caltech, it has been a pleasure to be a member of the GALCIT community. In particular, I would like to thank Christine Ramirez, Jamie Meighen-Sei, Denise Ruiz, and Liza Bradulina for the assistance they provided during my graduate career. I can recall numerous occasions where they met my concern and stress with smiles and support. I would also like to thank the Rose Hills Foundation for supporting my first year of graduate studies at Caltech through a Rose Hills Fellowship.

Some of the best memories of my graduate career came from right inside the (windowless) group office! From our Secret Santa gift exchange to the group retreats, I consider myself lucky to have been part of such a truly special group. I also want to acknowledge Morgan Hooper, with whom I completed the flow visualization studies presented in Chapter 3. Her experimental prowess was instrumental in the acquisition of stunning images that ended up landing us in the 2019 Gallery of Fluid Motion.

I am indebted to many friends and family outside the Caltech community as well. Indeed there are too many to count, but I appreciate each and every one of them for all the good memories. In particular, I want to express my gratitude to my uncle, Mehdi Taghiei. Beyond being an exemplary scientist, he epitomizes many of the qualities I aspire to. From my earliest memories of him, his patience, understanding, and support were evident. His mentorship throughout my life has helped me grow into the individual I am today, and for that I am profoundly grateful.

My sister, Mahya, also deserves appreciation, and not only for her patience having me as a little brother growing up! She is by far the most creative and detail oriented person I have ever met and I am honored to have had her as a role model during my life. Our conversations often gravitate from the pinnacle of science to the apex of

contemporary art, and I have learned multitudes from her along the way.

Finally, I want to thank my parents. Undoubtedly, not a single page of this thesis would be possible without their support. The love, compassion, and patience they have given me throughout my life has no bounds, and any good in me comes from them. It would be impossible for me to express everything they have done for me and all the sacrifices they've made, but suffice it to say, all the gratitude I can ever give them will only be but a drop in the ocean.

*This work was supported through an Army Research Office MURI grant# W911NF-17-1-0306.

ABSTRACT

This thesis addresses complexity reduction in periodic fluid-structure systems at low forcing frequencies. A novel quasi-steady time scaling framework is developed to relate the dynamics of a forced system to a corresponding unforced system.

Particle Image Velocimetry and dye flow visualization are used to study the streamwise-oscillating cylinder's wake at a mean Reynolds number $Re_0 = 900$. Forcing frequencies both one and two orders of magnitude below the stationary shedding frequency are considered. Forcing amplitudes are such that the instantaneous Reynolds number remains above the critical value at all times. It is shown that this forcing regime is synonymous with the development of both frequency and amplitude modulation in the wake. While frequency modulation is linked to vortex shedding, amplitude modulation arises due to symmetric reorganization of the wake at certain phases in the forcing cycle. Furthermore, Dynamic Mode Decomposition is used to extract underlying flow structures and quasi-steady time scaling is employed to relate dynamics to the corresponding unforced system. Specifically, forcing regimes where quasi-steady shedding can develop are identified and time is scaled to transform the system to resemble the stationary cylinder at the same mean Reynolds number.

Experimental flowfields are also used to analyze the wake of a surface mounted hemisphere subject to a highly pulsatile freestream, characterized by a forcing amplitude equal to the mean. Although this flow sees regular shedding of hairpin vortices in the unforced case, pulsatile forcing leads to significant deviations. For a nominal mean Reynolds number $\overline{Re_R} = 1000$, analysis of the wake shows that forcing at a frequency much smaller than that associated with hairpin shedding can lead to frequency modulated shedding. Consequently, time scaling is employed to reduce system complexity associated with hairpin shedding and to relate wake dynamics to the analogous unforced system.

PUBLISHED CONTENT AND CONTRIBUTIONS

Shamai, M., Dawson, S. T. M., Mezic, I., and McKeon, B. J. (2021). "Unsteady dynamics in the streamwise-oscillating cylinder wake for forcing frequencies below lock-on". In: *Physical Review Fluids*. DOI: 10.1103/PhysRevFluids.00.004700.

Designed the experimental campaign, performed the experiments, developed the analysis presented therein, and was the primary author of the paper.

Hooper, M., Shamai, M., and McKeon, B. J. (2019). "A Blacklight Ballet: Flow visualization reveals intricacies in the wake of a streamwise-oscillating cylinder". In: *72nd Annual Meeting of the APS Division of Fluid Dynamics*. DOI: 10.1103/APS.DFD.2019.GFM.V0017.

Collaborated in design, completion, and analysis of the experiments.

TABLE OF CONTENTS

Acknowledgements . . . iv
Abstract . . . vii
Published Content and Contributions . . . viii
Table of Contents . . . ix
List of Illustrations . . . xi
List of Tables . . . xvii
Chapter I: Introduction . . . 1
1.1 Motivation . . . 1
1.2 Periodic Behavior in Unsteady Flows . . . 2
1.3 Complexity Reduction and Reduced-Order Modeling . . . 3
1.4 Background . . . 5
1.4.1 Streamwise-Oscillating Cylinders . . . 5
1.4.2 Flow Around Surface-Mounted Hemispheres . . . 7
1.4.3 Koopman Analysis and Dynamic Mode Decomposition . . . 8
1.5 Outline of Thesis . . . 9
Chapter II: Methods . . . 11
2.1 Experimental Facilities . . . 11
2.1.1 NOAH Free-Surface Water Channel . . . 11
2.1.2 Captive Trajectory System . . . 12
2.1.3 Benchtop Pulsatile Wind Tunnel . . . 12
2.1.4 Forcing Trajectories . . . 13
2.2 Diagnostics . . . 17
2.2.1 Particle Image Velocimetry . . . 17
2.2.2 Fluorescent Dye Flow Visualization . . . 20
2.3 Data Analysis and Decomposition . . . 20
2.3.1 Phase Averaging . . . 20
2.3.2 Welch's Method . . . 20
2.3.3 Dynamic Mode Decomposition . . . 21
2.3.4 Γ_2 Vortex Identification . . . 22
2.3.5 Sparse Sensor Placement . . . 23
2.4 Quasi-Steady Time Scaling . . . 24
2.4.1 Quasisteadiness Parameter . . . 24
2.4.2 Time Scaling . . . 25
2.4.3 Implementation . . . 26
Chapter III: Characterization of the Streamwise-Oscillating Cylinder's Wake . 27
3.1 Stationary Cylinder . . . 27
3.1.1 Dynamic Mode Decomposition and Power Spectrum . . . 30
3.2 Oscillating Cylinder . . . 30
3.2.1 Observed States in the Wake . . . 30

3.2.2 Dynamic Mode Decomposition of the Oscillating Cylinder's Wake . . . 35
3.3 Vortex Dynamics . . . 39
3.3.1 Starting Vortex Generation . . . 39
3.3.2 Vortex Identification . . . 46
Chapter IV: Complexity Reduction of the Streamwise Oscillating Cylinder Wake . . . 52
4.1 Quasisteadiness . . . 52
4.2 Quasi-Steady Time Scaling . . . 54
4.3 Quasi-Steady Shedding Regimes . . . 55
4.4 Reduced-Order Flow Reconstruction . . . 59
4.5 Limitations of Time Scaling . . . 64
Chapter V: Complexity Reduction of the Flow Around a Hemisphere in Pulsatile Flow . . . 66
5.1 Flow Structures in the Absence of Pulsatility . . . 66
5.2 Analysis of the Hemisphere Wake with Pulsatile Forcing . . . 67
5.2.1 Hairpin Shedding Regime . . . 68
5.2.2 Phase-Locked Regime . . . 72
5.2.3 Dynamic Mode Decomposition . . . 75
5.3 Complexity Reduction via Time Scaling . . . 76
5.4 Sensor Placement . . . 81
5.5 Flow Reconstruction . . . 85
5.6 Chapter Summary and Outlook . . . 86
Chapter VI: Conclusion . . . 90
6.1 Summary . . . 90
6.2 Future Work . . . 92
Bibliography . . . 93

LIST OF ILLUSTRATIONS

Number *Page*

1.1 Dye flow visualization of vortex shedding in the wake of a stationary cylinder (top) and qualitative diagram of underlying flow structures (bottom). 4

2.1 Test section of NOAH water channel with Captive Trajectory System. Flow is from left to right. 12

2.2 Schematic of Benchtop Pulsatile Wind Tunnel (BPWT) used to study the flow around a surface-mounted hemisphere. From Carr (2019). . 13

2.3 Instantaneous Reynolds number experienced by cylinder. 14

2.4 Ratios of amplitude, A/D, and wavelength, λ/D, for streamwise forcing trajectories. The vertical dashed line represents the amplitude ratio for the nominal lock-on frequency, $St_f \approx St_0$. 15

2.5 Pulsatile forcing profiles. From Carr (2019). 16

2.6 (a) Schematic of PIV setup used in used in oscillating cylinder experiments; (b) clear acrylic cylinder mounted in the test section of the NOAH water channel. 18

3.1 Snapshots of (a) fluorescent dye, (b) vorticity, ω_z, (c) transverse velocity, v/U_∞, and (d) streamwise velocity, u/U_∞, for the stationary cylinder. The cross-section of the cylinder at the measurement plane is represented by $\oplus$ and the shaded circle corresponds to an obstruction in the field of view due to the bottom of the cylinder. The location of the interrogation point is denoted by $\times$. Flow is from right to left. $Re_0 = 900$. 28

3.2 Time trace of velocity measured at interrogation point for the stationary cylinder at $Re_0 = 900$. 29

3.3 Interrogation point spectra for stationary cylinder at $Re_0 = 900$ 29

3.4 DMD spectrum (a) and modes (b) for the stationary cylinder at $Re_0 = 900$. With the exception of the mean mode ($St = 0$), the colored circles on the spectrum represent shedding modes. The colored mode labels correspond to the circles of the same color on the spectrum. The black dot-dashed line represents the stationary shedding frequency. 31

3.5 DMD eigenvalues for the stationary cylinder at $Re_0 = 900$. The colored symbols correspond to the modes shown in Fig. 3.4. 32

3.6 Flow around a streamwise oscillating cylinder, $Re_0 = 900$, $\frac{Re_q}{Re_0} = 0.35$, $\frac{St_f}{St_0} = 0.18$. The top row corresponds to the position of the cylinder in the forcing cycle. The second row corresponds to visualization of the flow using fluorescent dye. The third row corresponds to vorticity ω_z. The fourth and fifth rows correspond to the transverse and streamwise components of velocity, $\frac{\mathrm{v}}{\mathrm{U}_\infty}$ and $\frac{\mathrm{u}}{\mathrm{U}_\infty}$, respectively. From left to right, the columns correspond to $\frac{t}{\tau_f} = 0, 0.25, 0.50$, and 0.75, respectively. The $\bigoplus$ symbol represents the cross-section of the cylinder at the measurement plane while the shaded circle represents an obstruction in the field of view due to the bottom of the cylinder. Flow is from right to left. 33

3.7 Time trace of velocity measured at the interrogation point. The dashed line is proportional to the instantaneous Reynolds number. $Re_0 = 900$, $Re_q/Re_0 = 0.35$, $St_f/St_0 = 0.18$. 34

3.8 Time trace of velocity measured at the interrogation point. The dashed line is proportional to the instantaneous Reynolds number. $Re_0 = 900$, $Re_q/Re_0 = 0.35$, $St_f/St_0 = 0.036$. 35

3.9 Interrogation point spectra corresponding to (a) $Re_q/Re_0 = 0.35$, $St_f/St_0 = 0.18$ and (b) $Re_q/Re_0 = 0.35$, $St_f/St_0 = 0.036$; $Re_0 = 900$ 35

3.10 DMD spectrum (a) and modes (b) for oscillating cylinder, $Re_0 = 900$, $Re_q/Re_0 = 0.35$, $St_f/St_0 = 0.18$. The colored mode labels correspond to the circles of the same color on the spectrum. The black dot-dashed line represents the stationary shedding frequency while the purple dashed line denotes the forcing frequency. The additional colored symbols on the spectrum indicate shedding modes. 37

3.11 DMD spectrum (a) and modes (b) for oscillating cylinder, $Re_0 = 900$, $Re_q/Re_0 = 0.35$, $St_f/St_0 = 0.036$. 38

3.12 Phase averaged vorticity (left) and transverse velocity (right), $Re_0 = 900$, $Re_q/Re_0 = 0.35$, $St_f/St_0 = 0.18$. From top to bottom, snapshots correspond to $t/\tau_f = 0$, $t/\tau_f = 0.25$, $t/\tau_f = 0.50$, and $t/\tau_f = 0.75$, respectively. 40

3.13 Flow visualization showing the generation and evolution of starting vortices. 41

3.14 Streamlines of phase-averaged velocity field before formation of starting vortex at $t/\tau_f = 0.4$ (left) and during formation of starting vortex $t/\tau_f = 0.5$ (right). $Re_0 = 900$, $Re_q/Re_0 = 0.35$, $St_f/St_0 = 0.18$. . . . 42
3.15 Vortex formation time for the streamwise-oscillating cylinder. Dashed horizontal lines correspond to critical value based on the respective definition. $Re_0 = 900$, $Re_q/Re_0 = 0.35$, $St_f/St_0 = 0.18$. 44
3.16 Vortex formation time for the streamwise-oscillating cylinder. $Re_0 = 900$, $Re_q/Re_0 = 0.35$, $St_f/St_0 = 0.036$. 44
3.17 DMD spectrum (a) and modes (b) for phase-averaged time series, $Re_0 = 900$, $Re_q/Re_0 = 0.35$, $St_f/St_0 = 0.18$. Note that phase averaging leads to a lower frequency resolution in the DMD spectrum. 45
3.18 Instantaneous snapshot of vortex identification via the Γ_2 criterion for a stationary cylinder at $Re_0 = 900$. 47
3.19 Vortex trajectories in the stationary cylinder's wake at $Re_0 = 900$. Trajectories on the top of the cylinder start further downstream due to PIV shadow. 47
3.20 Instantaneous snapshot of vortex identification via the Γ_2 criterion for an oscillating cylinder. $Re_0 = 900$, $Re_q/Re_0 = 0.35$, $St_f/St_0 = 0.18$. 48
3.21 Vortex trajectories in the streamwise-oscillating cylinder's wake corresponding to specified portion of forcing cycle. $Re_0 = 900$, $Re_q/Re_0 = 0.35$, $St_f/St_0 = 0.18$. 50
3.22 Secondary vortex generation in the oscillating cylinder wake. Arrows indicate secondary vortices. 51
4.1 (a) Phase portrait showing change in τ and $\dot{\tau}$ during forcing cycle. Line width is proportional to speed in phase-space. (b) Quasi-steadiness parameter plotted for streamwise forcing trajectory. 53
4.2 Comparison of predicted and observed dominant frequencies, $Re_0 = 900$, $St_f/St_0 = 0.18$. The solid lines represent the predicted dominant frequencies while the $\times$ symbols represent the actual dominant frequencies observed in experiments. 55
4.3 Variation in scaled time, $\tilde{t}$, with lab time, t. 56
4.4 Experimental sampling rate in lab time (top) and corresponding scaled time (bottom). Vertical lines correspond to snapshot acquisition in the experiment. For the sake of clarity, the number of samples shown has been significantly decreased relative to the actual experiment. 56

4.5 Time-trace of transverse velocity at interrogation point. $Re_0 = 900$, $Re_q/Re_0 = 0.35$, $St_f/St_0 = 0.18$. 57
4.6 Time-trace of transverse velocity at interrogation point. $Re_0 = 900$, $Re_q/Re_0 = 0.35$, $St_f/St_0 = 0.036$. 58
4.7 Interrogation point spectra for scaled system. (a) $Re_q/Re_0 = 0.35$, $St_f/St_0 = 0.18$, (b) $Re_q/Re_0 = 0.35$, $St_f/St_0 = 0.036$. $Re_0 = 900$. . . 58
4.8 Comparison of interrogation point power spectra before (left) and after (right) application of quasi-steady time scaling. 59
4.9 DMD spectrum (a) and modes (b) for oscillating cylinder with quasi-steady time scaling, $Re_0 = 900$, $Re_q/Re_0 = 0.35$, $St_f/St_0 = 0.18$. . . 60
4.10 DMD spectrum (a) and modes (b) for oscillating cylinder with quasi-steady time scaling, $Re_0 = 900$, $Re_q/Re_0 = 0.35$, $St_f/St_0 = 0.036$. . 61
4.11 Instantaneous snapshot reduced-order flow reconstruction in lab time, t. The location of the interrogation point is denoted by ×. $Re_0 = 900$, $Re_q/Re_0 = 0.35$, $St_f/St_0 = 0.18$. 62
4.12 Time trace of reconstructed velocity measured at interrogation point. $Re_0 = 900$, $Re_q/Re_0 = 0.35$, $St_f/St_0 = 0.18$. 63
4.13 Instantaneous snapshot reduced-order flow reconstruction in lab time, t. The location of the interrogation point is denoted by ×. $Re_0 = 900$, $Re_q/Re_0 = 0.35$, $St_f/St_0 = 0.036$. 63
4.14 Time trace of reconstructed velocity measured at interrogation point. $Re_0 = 900$, $Re_q/Re_0 = 0.35$, $St_f/St_0 = 0.036$. 63
5.1 Flow structures in the wake of a surface-mounted hemisphere. From Acarlar and Smith (1987). 68
5.2 Hairpin generation and shedding frequency for a surface-mounted hemisphere subject to a steady freestream. From Tamai et al. (1987). 69
5.3 Pulsatile forcing cycle for $St_f/St_0 = 0.05$ measured at interrogation pointed located approximately $2R$ upstream of cylinder and $3R$ away from the wall (furthest upstream point in PIV domain). The + symbols correspond to the snapshots shown in Fig. 5.4. 69

5.4 Flow around a hemisphere in pulsatile flow, $\overline{Re_R} = 1000$, $Re_q/\overline{Re_R} = 1$, $St_f/St_0 = 0.05$. The top row corresponds to vorticity ω_z. The second and third rows correspond to the streamwise and wall-normal components of velocity, $u/\overline{U}$ and $v/\overline{U}$, respectively. From left to right, the columns correspond to $t/\tau_f = 0, 0.25, 0.50$, and 0.75, respectively. The $\times$ symbol represents the location of the interrogation point. Flow is from left to right. 71
5.5 Trace of instantaneous freestream and velocity measured at interrogation point, $St_f/St_0 = 0.05$. 73
5.6 Flow around a hemisphere in pulsatile flow, $\overline{Re_R} = 1000$, $Re_q/\overline{Re_R} = 1$, $St_f/St_0 = 0.5$. The top row corresponds to vorticity ω_z. The second and third rows correspond to the streamwise and wall-normal components of velocity, $u/\overline{U}$ and $v/\overline{U}$, respectively. From left to right, the columns correspond to $t/\tau_f = 0, 0.25, 0.50$, and 0.75, respectively. The $\times$ symbol represents the location of the interrogation point. Flow is from left to right. 74
5.7 Pulsatile forcing cycle for $St_f/St_0 = 0.5$. The + symbols correspond to the snapshots shown in Fig. 5.6. 75
5.8 Trace of instantaneous freestream and velocity measured at interrogation point, $St_f/St_0 = 0.5$. 76
5.9 DMD spectrum (a) and modes (b) for the hemisphere in pulsatile flow for $St_f/St_0 = 0.05$. With the exception of the mean mode and forcing modes ($St = 0$ and $St = 0.01$), the colored circles on the spectrum represent shedding modes. The colored labels in (b) correspond to the circles of the same color on the spectrum. The black dot-dashed line represents the stationary shedding frequency while the purple dashed line denotes the forcing frequency. 77
5.10 DMD spectrum (a) and modes (b) for the hemisphere in pulsatile flow for $St_f/St_0 = 0.5$. 78
5.11 Fitted pulsatile forcing profile, $St_f/St_0 = 0.05$. 79
5.12 Power-law fit to data from Tamai et al. (1987). 80
5.13 Quasisteadiness, Ω, and scaled time, $\tilde{t}$, computed for pulsatile forcing cycle shown in Fig. 5.11, $St_f/St_0 = 0.05$. 80
5.14 Time trace of velocity measured at interrogation point of scaled flowfield, $St_f/St_0 = 0.05$. 82

5.15 DMD spectrum (a) and modes (b) for the hemisphere in pulsatile flow under quasi-steady time scaling. $St_f/St_0 = 0.05$. 83
5.16 Sparse sensor placement in pulsatile flowfield, $St_f/St_0 = 0.05$. 85
5.17 Snapshot of full flowfield (top) and flow reconstruction (bottom) using a small subset of DMD modes, $t/\tau_f = 0.75$. 87
5.18 Time trace of velocity measured at interrogation point in full flowfield (top) and flow reconstruction (bottom). 88

LIST OF TABLES

Number *Page*

2.1 Forcing parameters used in oscillating cylinder experiments. 14

2.2 Forcing parameters used in surface-mounted hemisphere experiments. 16

Chapter 1

INTRODUCTION

1.1 Motivation

From the flow of blood inside our veins, to a deep sea oil rig violently swaying back and forth during a hurricane, fluid-structure interaction is ubiquitous in the world around us. The introduction of additional boundary conditions to a flowfield via the presence of a structure lies at the core of this discipline. The resulting flow structures and aerodynamic loads can vary drastically depending on the flow regime that develops. Consequently, understanding of fluid-structure systems is vital both in the design and validation of numerous engineering systems. The collapse of the Tacoma Narrows Bridge in 1940, where a resonant torsional vibration mode was excited by the oncoming wind, thereby resulting in aerodynamic loads beyond the bridge's design limit (Amman et al., 1941), highlights the need for comprehensive understanding of such systems. Not all fluid-structure systems sit at the scale of the Tacoma Narrows Bridge, however. Examples including the flow of blood through the heart (Gharib et al., 2006), the flow of air over oscillating vocal folds (Mittal et al., 2013), and energy harvesting via wind turbines capture the breadth of applications. Often, fluid-structure interaction serves as the starting point to the analysis of such systems. Even in seemingly disparate applications, a similarity between the underlying physics and consequent behavior can often be observed. As such, a profound understanding of even the simplest fluid-structure phenomena can enable the analysis of various, seemingly unrelated systems.

Although a multitude of open questions exist regarding the modeling and analysis of fluid-structure systems, the work in this thesis will use periodic forcing to study relevant unsteady flow-phenomena and address facets related to complexity reduction in such systems. It should be noted that fluid-structure interaction typically denotes configurations where body motion is coupled with the flow. A significant focus of this thesis, in particular, is the relation between unsteady flow phenomena in forced and unforced systems. Namely, which subset of dynamics observed in the absence of forcing carries over to the forced system, especially if the forcing frequency is small relative to the system's characteristic frequency. In the case that similar dynamics are observed in the forced and unforced systems, the path towards

complexity reduction is not immediately evident. Thus, it will be shown that under certain circumstances, the forced system can indeed be transformed to resemble its unforced counterpart. Consequently, the core mechanisms at play within the system can also be identified. In so doing, an avenue is opened, allowing scientists and engineers alike to use their knowledge of an unforced system to guide design and analysis of a corresponding forced system. Not only are unforced systems typically characterized by relatively simpler dynamics, but forced fluid-structure systems are considerably more difficult to study. Thus, relation of a forced system to an analogous unforced system can also facilitate understanding and characterization of forcing regimes outside the reach of experiment.

1.2 Periodic Behavior in Unsteady Flows

Periodic motion is the cornerstone to an important subset of fluid-structure systems. An important distinction resulting from periodic motion is the introduction of a timescale associated with the periodicity, beyond timescales inherent to the flow. For example, a rigid cylinder subject to a steady freestream sheds vortices of opposing rotation when the Reynolds number, a relevant non-dimensional parameter, exceeds the critical value of $Re_{cr} = 47$ (Fey et al., 1998), as seen in Fig. 1.1a. A compliant cylinder subject to the same freestream, however, can exhibit vortex-induced vibration (VIV), one of the canonical examples of a periodic fluid-structure system. Similarly, the wake of a cylinder undergoing VIV can vary significantly from its stationary analog (Williamson and Govardhan, 2004). Periodic fluid-structure systems can also arise due to external forcing, a prime example of which is dynamic stall on harmonically pitched airfoils (McCroskey, 1981), a phenomenon considered in numerous studies (Corke and Thomas, 2015). Similarly, many studies have also considered harmonic forcing and dynamic stall in the context of wind turbines for energy harvesting applications (Hansen and Butterfield, 1993; Simao Ferreira et al., 2010; Dunne and McKeon, 2015).

The separation of scales, or lack thereof, between flow and forcing frequencies also plays an important role in the resulting dynamics. This notion will be an important focus of the work in this thesis, primarily for forcing frequencies, f_f, much smaller than the system's characteristic frequency, f_0. This forcing regime, $f_f \ll f_0$, corresponds to numerous physical systems of scientific and engineering interest. The aforementioned example of vortex shedding from an airfoil undergoing dynamic stall falls into this regime. Tidal flows around bluff bodies often correspond to low frequency ratios as well. More exotic applications include the flow around

one body in the wake of another, where the oncoming flow can be characterized by a similar frequency ratio. This scenario holds particular significance for modeling the disturbance environment in potential energy harvesting applications, where a deeper understanding of low forcing frequencies is vital. An extreme example presented by Beal et al. (2006) showed that a dead fish could passively produce thrust and move upstream when situated in the wake of a bluff body.

1.3 Complexity Reduction and Reduced-Order Modeling

Analytical approaches to address of fluid-structure phenomena have been hindered by the lack of a general solution to the governing equations of fluid mechanics,

$$\nabla \cdot \mathbf{u} = 0 \tag{1.1}$$

$$\frac{\partial \mathbf{u}}{\partial t} + \mathbf{u} \cdot \nabla \mathbf{u} = -\frac{\nabla p}{\rho} + \mathbf{g} + \nu \nabla^2 \mathbf{u}, \tag{1.2}$$

also known as the Navier-Stokes equations, where $(t, p, \rho, \nu, \mathbf{u}, \mathbf{g})$ denote the time, pressure, density, kinematic viscosity, velocity, and gravitational acceleration, respectively. Equations (1.1) and (1.2) shown here correspond to the case of an incompressible fluid. Although the Navier-Stokes equations govern even the most chaotic and complicated flows, many systems are characterized by relatively simple, low-order dynamics. A prime example of this is the Kármán vortex street that develops in the wake of a cylinder when $Re > 47$, as seen in Fig. 1.1a. The dye flow visualization shown in Fig. 1.1a alludes to the presence of relatively simple underlying flow structures akin to the qualitative diagram shown in Fig. 1.1b. This notion, that a flow may be characterized by a limited number of underlying structures, is not unique to the cylinder wake and, in the absence of a general solution to Eqs. (1.1) and (1.2), motivates the use of modal decompositions to analyze many fluid dynamic phenomena. The identification of simple, low-order flow structures via modal analysis sheds significant insight into the underlying flow physics and tends to a reduction in system complexity (Rowley and Dawson, 2017; Taira et al., 2017). Beyond their utility extracting underlying dynamics, modal decompositions have also proven invaluable in the development of reduced order models (Rowley and Dawson, 2017; Taira et al., 2017). Resulting reduced-order models are often used to guide design and control of fluid-structure systems and are thus an important consequence of modal analyses.

The variety of modal analysis and decomposition techniques spans a space nearly as large the applications themselves, but, they can often be sorted into two categories:

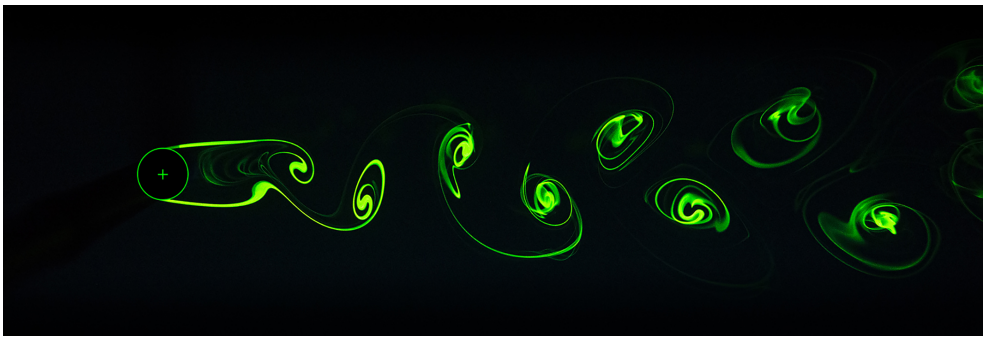

(a)

(b)

Figure 1.1: Dye flow visualization of vortex shedding in the wake of a stationary cylinder (top) and qualitative diagram of underlying flow structures (bottom).

data-driven and equations based. Data-driven techniques are agnostic of the governing equations and rely on the identification of dynamics embedded inside the data. Common methods include Proper Orthogonal Decomposition (POD) and Dynamic Mode decomposition (DMD) (Schmid, 2010). On the other hand, equation-based methods, such as Resolvent Analysis (McKeon and Sharma, 2010) and Koopman Analysis (Mezic, 2005), build on the structure of governing equations in order to analyze the flow. It will be shown in this thesis that forced fluid-structure systems can benefit from the application of such techniques, both to facilitate a better understanding of the underlying dynamics and to develop simple reduced-order models.

In addition to modal analysis techniques, fluid dynamicists often employ quasi-steady approximations to further reduce system complexity associated with disparate time scales. Although the use of quasi-steady approximations is not unique to fluid mechanics, the underlying theme is unifying. That is, a system exhibiting activity spanning multiple time scales can be simplified greatly if the time scales are

sufficiently separated such that the dynamics at one scale can be considered steady relative to the others (Segel and Slemrod, 1989; Van Cutsem and Vournas, 1998). This assumption has proven invaluable in the understanding and modeling of fluid flows. One example includes the work of Sane and Dickinson (2002) who used a quasi-steady model to characterize different phenomena contributing to the force exerted on a flapping wing. One objective of the current study is the development of a framework that can be used to identify forcing regimes where the assumption of quasi-steady dynamics is appropriate.

1.4 Background

In this thesis, two configurations are studied, namely the wake of a streamwise oscillating cylinder and the flow around a surface mounted hemisphere. A brief overview of the configurations, as well as the analysis techniques used to study them, are provided in this section.

1.4.1 Streamwise-Oscillating Cylinders

An expansive body of work considers the flow around oscillating cylinders (Williamson and Roshko, 1988; Williamson and Govardhan, 2004). Examining the literature, however, reveals that only a small subset of studies considers streamwise oscillations. This is primarily due to significant interest in transverse oscillations and their role in vortex-induced vibration. In contrast to transverse oscillations, streamwise forcing induces relatively stronger changes in the instantaneous Reynolds number, adding interest to the problem as well as delineating it from the transverse case. Hence, understanding the dynamics of the streamwise-oscillating cylinder could prove useful in categorizing structures seen in the wake of an unsteady body into those generated by changes in the Reynolds number and those specific to the body's geometry. Within the body of work considering streamwise oscillations, the majority of studies consider forcing frequencies, f_f, of the same order of magnitude (or higher) than the stationary shedding frequency, f_0. This regime is of interest due to the lock-on phenomenon, the synchronization between the shedding frequency, f_s, and forcing frequency, f_f, that occurs when the streamwise forcing frequency is approximately equal to the stationary shedding frequency (Barbi et al., 1986). Previous studies have also shown the development of periodic activity at subharmonics of the shedding frequency both in the case of external forcing (Leontini et al., 2013) and in response to the flow (Van Atta and Gharib, 1987). Furthermore, it is has previously been shown that streamwise forcing not corresponding to lock-on can

lead to wake patterns that significantly deviate from the classic Kármán vortex street (Barbi et al., 1986; Griffin and Ramberg, 1976; Leontini et al., 2011; Leontini et al., 2013).

The phenomena that arise due to streamwise forcing are intricately related to vortex dynamics as well as the forcing frequency and amplitude. Leontini et al. (2011) studied the streamwise-oscillating cylinder using two-dimensional computations with mean Reynolds number, $Re_0 = 175$. They considered a forcing frequency equivalent to the stationary shedding frequency and deduced that the development of frequency modulation in the wake is governed by the forcing frequency while vortex interactions lead to the development of amplitude modulation. Leontini et al. (2013) parametrically studied the streamwise-oscillating cylinder for $75 \leq Re_0 \leq 250$ and forcing frequencies in the range $1 \leq f_f/f_0 \leq 2$.

Konstantinidis et al. (2020) studied a cylinder allowed to oscillate in-line with the flow subject to a steady freestream. In an effort to model the force on the cylinder, they conducted a parametric study of the system at low Reynolds numbers. They presented the development of a resonant oscillation mode corresponding to the synchronization between shedding and body motion. Even though both the shedding and oscillation were synchronized, it was seen that the relative phase between the two played an important role in determining the force felt by the cylinder. A deeper understanding of the phase-dependent dynamics plays a vital role in understanding and modeling the system.

Glaz et al. (2017) used Koopman analysis to analyze the temporal behavior of a streamwise-oscillating cylinder with mean Reynolds number, $Re_0 = 53$ (close to the critical value). They considered a forcing frequency two orders of magnitude less than the stationary shedding frequency for various oscillation amplitudes. Koopman analysis was performed in parallel to two-dimensional flow simulations and the results were in good agreement. Glaz et al. showed that the flow in this regime was marked by instances of strong vortex shedding which were then replaced by periods of suppressed shedding and weak oscillatory behavior, a phenomenon they referred to as "quasi-periodic intermittency." Additionally, they observed that streamwise forcing led to the extraction of additional flow structures (modes) related to vortex shedding as well as a broadening of the associated spectral peak.

1.4.2 Flow Around Surface-Mounted Hemispheres

The flow around a surface-mounted hemisphere has received considerable attention in previous studies, especially for the overlap between observed wake structures, such as hairpin vortices, with other fluid flows. Acarlar and Smith (1987) experimentally characterized the three-dimensional flowfield around a surface mounted hemisphere subject to a steady freestream for $30 \leq Re_R \leq 3400$. Beyond $Re_R \approx 120$, they observed the onset of periodic behavior in the form of hairpin vortex shedding. Hairpin shedding was observed up to $Re_R \approx 3400$ at which point the wake started to show signs of irregularity. Additionally, Acarlar and Smith (1987) noted the development of a horseshoe vortex located upstream of the hemisphere with legs stretching downstream around the sides of the hemisphere. The presence of the horseshoe vortex was shown to affect the structure of the hairpin vortices and also led to the generation of secondary flows structures. Tamai et al. (1987) extended the results of Acarlar and Smith (1987) to a higher range of Reynolds numbers, specifically, up to $Re_R = 12000$. They observed an important distinction at $Re_R = 2000$ regarding the hairpin vortices. Namely, if $Re_R > 2000$, multiple hairpins coalesced in the near wake to form a single hairpin vortex which was then shed downstream. Consequently, Tamai et al. (1987) observed that the hairpin formation and shedding frequency differed beyond $Re_R = 2000$.

The effect of a time-varying freestream on the flow around a surface mounted hemisphere has received significantly less attention. In particular, only a handful of studies have considered the surface-mounted hemisphere in highly pulsatile flow, where the amplitude of freestream fluctuations equals its mean. Carr and Plesniak (2016), Carr (2019), and Carr et al. (2020) characterized this flow regime for flow parameters overlapping with human phonation. In particular, Carr (2019) and Carr et al. (2020) considered experiments and simulations at various pulsatile forcing frequencies and showed that the flowfield permitted segments of hairpin shedding when the forcing frequency was much smaller than the unforced shedding frequency. When the forcing frequency was of the same order as the shedding, however, the wake displayed phase-locked dynamics associated with the generation of a single rear arch vortex during each forcing cycle. They also showed that the resulting rear arch vortex propagated upstream as the freestream velocity approached zero and related its resulting motion to the dynamics of a vortex ring.

1.4.3 Koopman Analysis and Dynamic Mode Decomposition

First proposed in the early 20$^{\text{th}}$ century (Koopman, 1931), the Koopman operator is a linear, infinite-dimensional composition operator which acts on the observables of a dynamical system, such as velocity or pressure. Following the analysis of Rowley et al. (2009), the Koopman operator can be defined in a discrete-time setting as follows. Let $\mathbf{x}_k$ denote the full state of the system at time $t = k\Delta t$, evolving according to the relation

$$\mathbf{x}_{k+1} = \mathbf{f}(\mathbf{x}_k). \tag{1.3}$$

Expressing an observable of the system as $\mathbf{g}(\mathbf{x})$, the Koopman operator, $\mathcal{K}$, is defined by the relation

$$\mathcal{K}\mathbf{g}(\mathbf{x}) = \mathbf{g}(\mathbf{f}(\mathbf{x})). \tag{1.4}$$

It should be noted that the Koopman operator is linear even if the underlying dynamics, namely $\mathbf{f}(\mathbf{x})$, are not. Observables are typically expanded in terms of eigenvalues, λ, eigenfunctions, ϕ, and eigenmodes, $\mathbf{v}$, of the Koopman operator, such that

$$\mathbf{g}(\mathbf{x}_k) = \sum_{i=1}^{\infty} \lambda_i^k \phi_i(\mathbf{x}_0)\mathbf{v}_i. \tag{1.5}$$

Thus, the Koopman eigenvalues, λ_i, capture the temporal dynamics of the spatial structure in the corresponding Koopman mode, $\mathbf{v}_i$. In practice, computation of Koopman modes and eigenvalues from experimental or computational flowfields can be achieved, at least approximately, via various data-driven algorithms. As shown by Rowley et al. (2009), Koopman modes and eigenvalues can be approximated using Dynamic Mode Decomposition.

The Dynamic Mode Decomposition (DMD) refers to the eigen-decomposition of the linear operator that best approximates system dynamics (Schmid, 2010). The power of DMD lies in its ability to extract flow structures that are of spatio-temporal importance (Schmid, 2010; Rowley et al., 2009). One advantage of DMD is its ability to extract the temporal growth rate of spatial structures (modes) (Chen et al., 2012). Many spectral analysis techniques, such as the temporal Discrete Fourier Transform (DFT), only yield mode frequencies and not growth rates, limiting the insight they give into systems with high degrees of unsteadiness or transient behavior. Also, in contrast to the temporal DFT, the set of frequencies extracted by DMD does not have to be equally spaced (Chen et al., 2012), making DMD a good candidate for studying systems with dynamics distributed over a range of unequally spaced frequencies. As such, DMD has been used extensively to study a wide range

of systems (Rowley and Dawson, 2017), specifically to identify dominant linear dynamics and to inform reduced complexity flow models.

1.5 Outline of Thesis

This thesis focuses on complexity reduction and analysis of forced fluid-structure systems. Although a broad body of work revolves around stationary, or unforced systems, the connection with analogous forced systems occupies a much smaller space. To this end, the research presented here seeks to provide a foundation to relate the two. Beyond the development of such a framework, the flowfield and underlying dynamics of two forced fluid-structure systems will be studied. Specifically, it will be shown that for certain forcing regimes, the aspects of the flow around a streamwise-oscillating cylinder and surface mounted hemisphere in highly pulsatile flow can be related to the corresponding unforced systems.

In Chapter 2, the experimental methods employed in the research will be presented. Details regarding the experimental facilities, forcing trajectories, and measurement diagnostics will be discussed. The analytical techniques, such as DMD, used in the thesis will also be presented. Similarly, the quasi-steady time scaling framework used to relate forced and unforced dynamics will also be developed.

The streamwise-oscillating cylinder wake will be studied in Chapter 3 for forcing frequencies much lower than those required for lock-on, a regime largely overlooked in previous studies. It will be shown that this forcing regime corresponds to the development of both frequency and amplitude modulation in the wake. DMD and Welch's method will be used to show that frequency modulation arises from vortex shedding across a range of frequencies. Phase-averaged flowfields will also be presented in Chapter 3 to study the generation of starting vortices and their role in the observed amplitude modulation.

In Chapter 4, the quasi-steady time scaling framework developed in Chapter 2 will be used to reduce the complexity of the streamwise-oscillating cylinder's wake. It will be shown that during certain portions of the forcing cycle, wake dynamics arise from vortex shedding similar to the unforced case at the corresponding instantaneous Reynolds number. Furthermore, time will be scaled to transform the system such that resulting dynamics resemble that of the stationary cylinder at the mean Reynolds number. The consequent complexity reduction due to time scaling will be used to generate a simple reduced-order model of the flow.

Analysis of the flow around a surface mounted hemisphere subject to highly pulsatile

forcing will be presented in Chapter 5. It will be shown that for low forcing frequencies, certain portions of the pulsatile forcing cycle permit the development of frequency modulated shedding. Although the resulting flowfield is highly unsteady and three-dimensional, time will be scaled to transform the system such that certain aspects of the flow can be related to the unforced case. In so doing, it will be shown that the hemisphere exhibits quasi-steady shedding analogous to the case of a steady freestream.

A brief summary, including major findings of the research will be presented in Chapter 6, and various paths forward in future work will also be discussed.

Chapter 2

METHODS

Portions of this chapter will appear in the forthcoming journal publication:

Shamai, M., Dawson, S. T. M., Mezic, I., and McKeon, B. J. (2021). "Unsteady dynamics in the streamwise-oscillating cylinder wake for forcing frequencies below lock-on". In: *Physical Review Fluids*. DOI: 10.1103/PhysRevFluids.00.004700.

In this chapter, the experimental and theoretical methods used in the thesis are developed. Experimental facilities and diagnostics used to acquire flowfields considered in subsequent chapters are summarized. Specifically, setups are presented corresponding to oscillating cylinder experiments as well as surface-mounted hemisphere studies. Streamwise-oscillating cylinder experiments were performed in the NOAH free-surface water channel at Caltech. Surface-mounted hemisphere experiments, however, were performed using the Benchtop Pulsatile Wind Tunnel at the George Washington University by Dr. Ian Carr and Professor Michael Plesniak (Carr, 2019)[1]. Beyond the experimental approach, this chapter will highlight the analytical methods used in the thesis, along with the quasi-steady time scaling developed to reduce system complexity.

2.1 Experimental Facilities

2.1.1 NOAH Free-Surface Water Channel

Streamwise-oscillating cylinder experiments were performed in the NOAH free-surface water channel at Caltech. In order to reduce turbulent fluctuations and swirl in the freestream, the flow is conditioned using a set of perforated plates, honeycombs, and metal screens before entering the test section. A 4:1 contraction, located downstream of the flow conditioners, is used to increase the flow speed before entering the test section. The test section has a length of 150 cm, width of 46 cm, and (water) depth of 46 cm. The sides and bottom of the test section consist of transparent glass panels allowing optical access for measurement diagnostics. Streamwise-oscillating cylinder experiments were all performed with a freestream

[1] Surface-mounted hemisphere experiments were carried out by Ian A. Carr and Michael W. Plesniak. We are extremely grateful to them for sharing the data with us as well as invaluable discussions and insight.

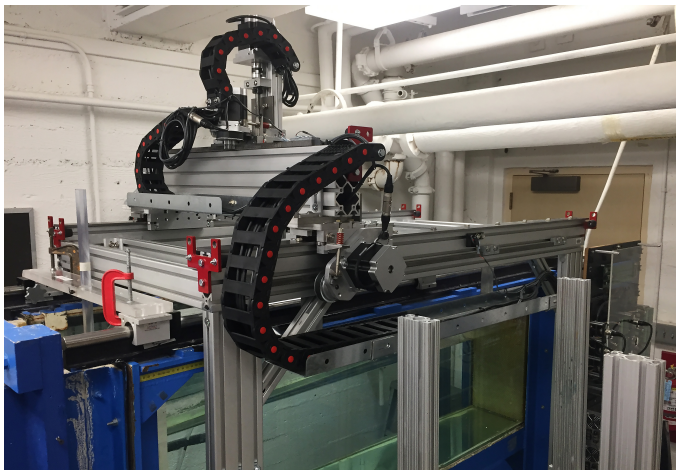

Figure 2.1: Test section of NOAH water channel with Captive Trajectory System. Flow is from left to right.

velocity of $U_\infty = 4.7$ cm/s. At this velocity, the mean turbulence intensity in the test section was measured to be $u'_{rms}/\overline{U} \approx 4\%$.

2.1.2 Captive Trajectory System

The parameter space accessible via experiments using the NOAH water channel has been expanded with the recent addition of a Captive Trajectory System (CTS). The CTS enables actuation of a body, such as an airfoil, within the channel's test section. The CTS spans the entirety of the water channel's test section, as seen in Fig. 2.1, and allows for translation along the three Cartesian axis. The system is configured such that translation in the streamwise, spanwise, and vertical directions correspond to actuation along the x, y, and z-axes of the CTS, respectively. Similarly, variation of pitch angle, α, corresponds to rotation about the z-axis. Motion is achieved using multiple stepper motors enabling position control with sub-millimeter accuracy. To ensure smooth motion even at low speeds, the smallest allowable step size was used for the streamwise stepper motors. The gain of the Proportional-Derivative (PD) controller governing the stepper motors was also adjusted to ensure resulting trajectories tracked position and velocity commands accurately and smoothly. Experiments made use of a predetermined forcing trajectory which was followed by the CTS during each experimental run.

2.1.3 Benchtop Pulsatile Wind Tunnel

The flow around a surface-mounted hemisphere subject to a highly pulsatile freestream was studied using the the Benchtop Pulsatile Wind Tunnel (BPWT) at the George

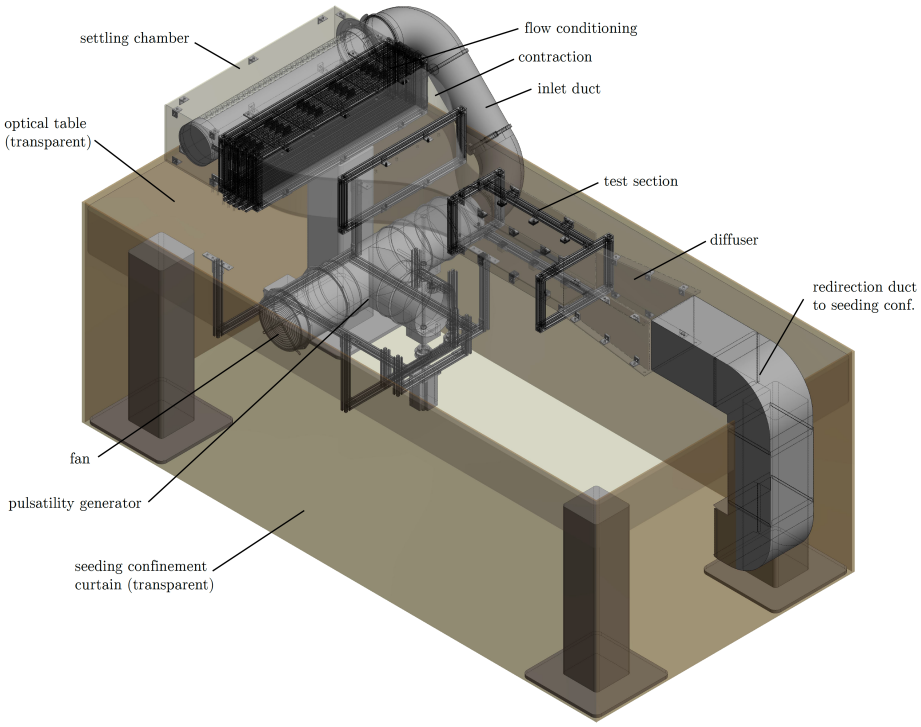

Figure 2.2: Schematic of Benchtop Pulsatile Wind Tunnel (BPWT) used to study the flow around a surface-mounted hemisphere. From Carr (2019).

Washington University. The surface-mounted hemisphere experiments analyzed in this thesis were first presented in Carr (2019). The specifications of the BPWT are summarized here briefly, but for additional details, one can refer to Carr (2019). The BPWT is a purpose-built wind tunnel capable of producing highly pulsatile flows. It has a test section height of 15 cm, width of 15 cm, and length of 50 cm. The walls of the test section have been constructed using clear acrylic for optical access. Before entering the test section, flow is conditioned using a honeycomb and multiple screen meshes before entering the 5:1 contraction upstream of the test section (shown in Fig. 2.2). Pulsatility is achieved through the use of two butterfly valves located upstream of the settling chamber and flow conditioners. One valve redirects flow back to the seeding confinement chamber while the other valve diverts flow to the settling chamber and through the flow conditioners. The valves are oriented such that the open cross-sectional area remains constant at all times. The pulsatile frequency is determined by the frequency at which the valves are cycled.

2.1.4 Forcing Trajectories

Oscillating cylinder experiments utilized a sinusoidal forcing trajectory consisting of oscillation in the streamwise direction with angular frequency $\omega_f = 2\pi/\tau_f$. The

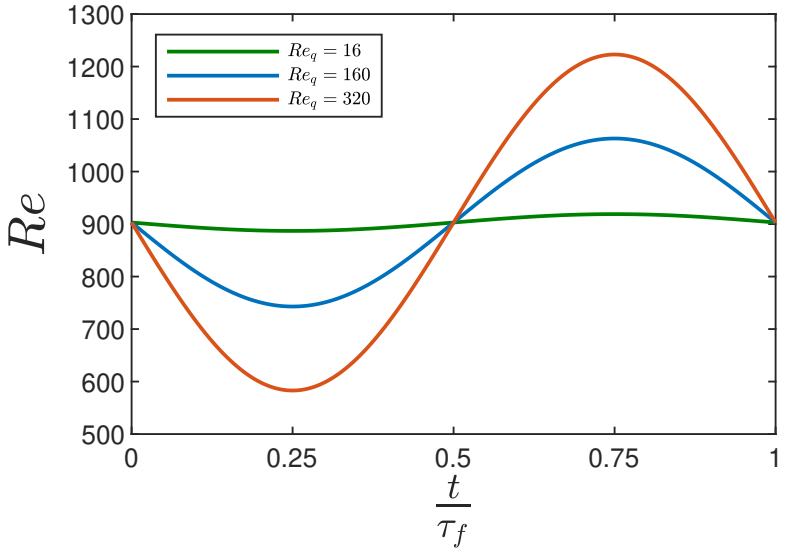

Figure 2.3: Instantaneous Reynolds number experienced by cylinder.

freestream velocity, U_∞, was held constant, such that the effective instantaneous velocity experienced by the cylinder is given by

$$U(t) = U_\infty - \frac{2q}{\omega_f}\sin(\omega_f t). \tag{2.1}$$

The parameter q, with units of acceleration, characterizes the amplitude of forcing, after Glaz et al. (2017). The corresponding variation of instantaneous Reynolds number is

$$Re(t) = \frac{U(t)D}{\nu} = Re_0 - Re_q \sin(\omega_f t). \tag{2.2}$$

$Re_0 = \frac{U_\infty D}{\nu}$ corresponds to the mean Reynolds number, while $Re_q = \frac{2Dq}{\nu\omega_f}$ characterizes the forcing amplitude. Re_0 and Re_q, combined with the forcing Strouhal number, $St_f = \frac{\omega_f D}{2\pi U}$, were varied to modify the forcing trajectory.

Re_0	Re_q	St_f/St_0	Re_q/Re_0
900	16	0.018	0.018
900	160	0.018	0.18
900	16	0.036	0.018
900	160	0.036	0.18
900	320	0.036	0.35
900	16	0.18	0.018
900	160	0.18	0.18
900	320	0.18	0.35

Table 2.1: Forcing parameters used in oscillating cylinder experiments.

Experiments were performed for multiple combinations of forcing frequency and amplitude all with mean Reynolds number of $Re_0 = 900$. At this Reynolds number,

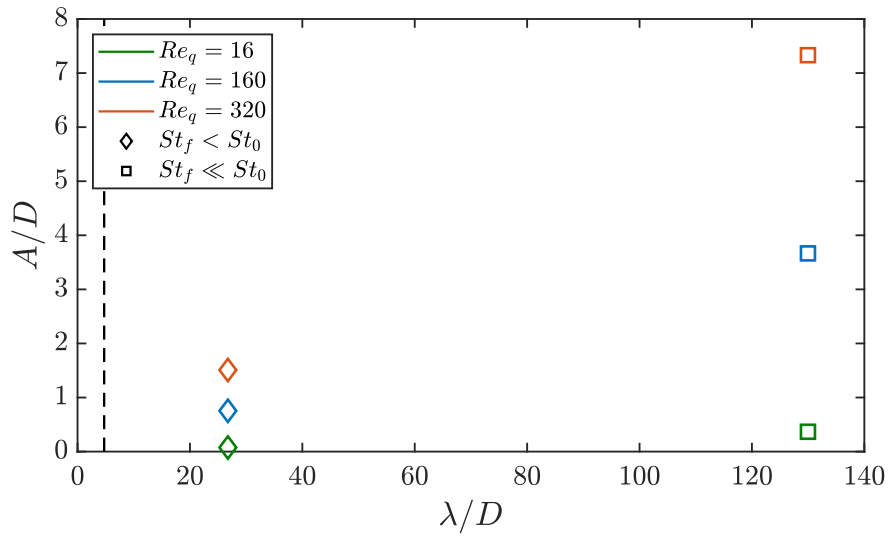

Figure 2.4: Ratios of amplitude, A/D, and wavelength, λ/D, for streamwise forcing trajectories. The vertical dashed line represents the amplitude ratio for the nominal lock-on frequency, $St_f \approx St_0$.

the stationary shedding Strouhal number, $St_0 = \frac{f_0 D}{U_\infty}$, is $St_0 = 0.21$ (Fey et al., 1998). Forcing frequencies both one and two orders of magnitude less than the stationary shedding frequency were considered. Throughout the remainder of this thesis, $St_f < St_0$ will refer to cases with a forcing frequency one order of magnitude less than the stationary shedding frequency while $St_f \ll St_0$ will designate cases with two orders of magnitude difference between forcing and stationary shedding frequencies. Table 2.1 presents a summary of the various combinations of forcing frequency and amplitude considered in experiments. The time-varying Reynolds number experienced by the cylinder is shown in Fig. 2.3. It is important to note that forcing parameters were chosen such that the instantaneous Reynolds numbers remained well above the critical value for vortex shedding (Fey et al., 1998). Namely, $Re(t) \gg Re_{cr} = 47$ at all times. Ratios of forcing frequency and amplitude, $\frac{St_f}{St_0}$ and $\frac{Re_q}{Re_0}$, respectively, were chosen to to facilitate comparison with previous studies (Glaz et al., 2017), albeit at higher Reynolds numbers. In addition, previous work by Williamson and Roshko (1988) has shown that for a cylinder undergoing transverse oscillations, the amplitude ratio, A/D, and wavelength ratio, $\lambda = \overline{U}\tau_f/D$, govern wake topology. This idea has been extended here to the streamwise-oscillating cylinder, and values corresponding to the forcing cycles considered in the current study are shown in Fig. 2.4.

In contrast to oscillating cylinder experiments, the surface-mounted hemisphere was

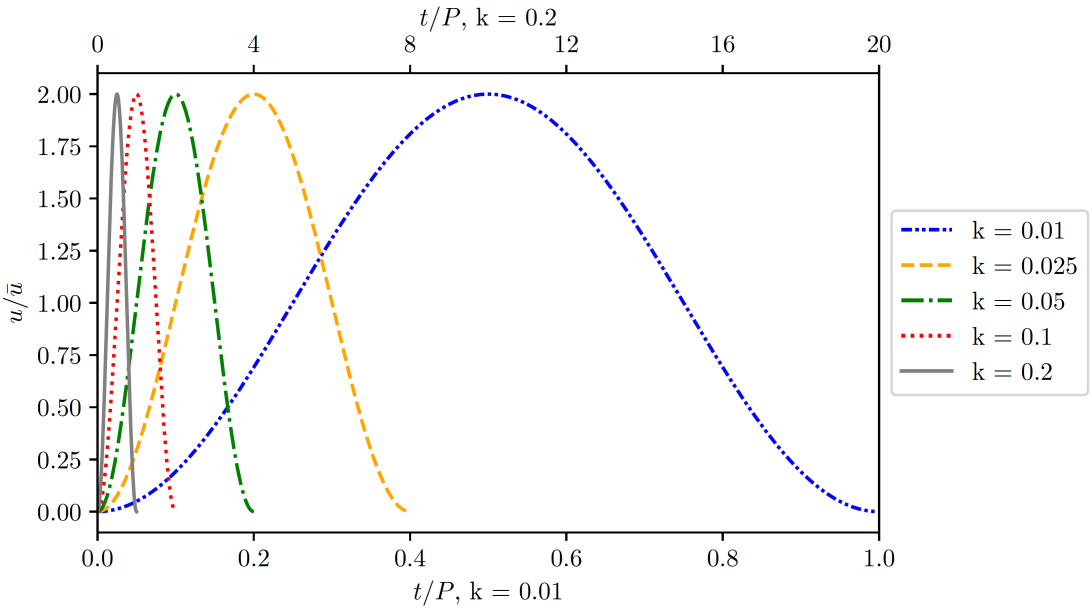

Figure 2.5: Pulsatile forcing profiles. From Carr (2019).

fixed while the freestream velocity varied following a sinusoidal forcing profile. All experiments were performed at the same mean Reynolds number $\overline{Re_R} = \frac{\overline{U}R}{\nu}$, specifically, $\overline{Re_R} = 1000$. The amplitude of the time-dependent Reynolds number was also kept constant and chosen to equal its mean value, namely, $Re_\Delta = 1000$. Forcing frequencies spanning two orders of magnitude were considered in experiments. Forcing parameters for the cases considered here are presented in Table 2.2, while pulsatile forcing trajectories are shown in Fig. 2.5. The quantity referred to here as

$\overline{Re_R}$	Re_Δ	St_f/St_0	$Re_\Delta/\overline{Re_R}$
1000	1000	0.05	1
1000	1000	0.5	1

Table 2.2: Forcing parameters used in surface-mounted hemisphere experiments.

the forcing Strouhal number, St_f, is often called the reduced frequency (Carr, 2019), k, but for the sake of consistency, it will be referred to as St_f in the remainder of this thesis. It should also be noted that forcing profiles achieved using the BPWT were not perfectly sinusoidal and deviated considerably. However, Carr (2019) and Carr et al. (2020) compared experimental results to Direct Numerical Simulation (DNS) of the same system, but with ideal forcing, and observed good similarity between the observed flow phenomena for both cases.

2.2 Diagnostics

Multiple diagnostics were used to measure the flow and obtain both qualitative and quantitative insight into the flow physics.

2.2.1 Particle Image Velocimetry

A clear acrylic cylinder with a diameter of 19 mm and wetted length of 46 cm was mounted onto the CTS such that its axis pointed down towards the bottom of the test section, as seen in Fig. 2.6b. In order to reduce end effects, the bottom of the cylinder was located approximately one millimeter from the bottom of the test section. For the range of Reynolds numbers considered here ($Re_0 \sim 10^3$) the wake sees development of three-dimensional structures, including, but not limited to, vortex dislocations and oblique shedding angles (Williamson, 1996). The analysis in this thesis is primarily concerned with large scale structures in the wake, in particular, shed vortices. It will be shown that these structures are clearly distinguishable in two-dimensional flow fields. Furthermore, consideration of the transverse component of velocity (v) alone gives significant insight into the dynamics of the wake. As such, two-dimensional time resolved particle image velocimetry (PIV) was deemed to be sufficient and used as the primary diagnostic to acquire velocity fields in oscillating cylinder experiments.

The laser and optics were configured such that the laser sheet was concurrent with the cross-section of the cylinder. A Photonics DM20-527(nm) dual-head YLF laser was pulsed to illuminate reflective tracer particles. Images of the illuminated particles were acquired using two Phantom Miro Lab 320 cameras with AF Nikkor 50mm f/1.8D lenses. As seen in Fig. 2.6a, the cameras were situated under the test section, normal to the laser sheet, but staggered in the streamwise direction. Partially overlapping fields of view allowed stitching of vector fields in post-processing. The resulting vector fields spanned $20D$ in the streamwise direction and $8D$ in the transverse direction, ensuring the cylinder remained inside the field of view at all times. Both single-pulse and double-pulse laser configurations were used in experiments. Single-pulse experiments produced a higher time resolution but shorter record length while double-pulse experiments lead to a longer record length but reduced time resolution. The sampling rate for single pulse experiments was 70 Hz, while double pulse experiments had an effective sampling rate of 12 Hz, both well above the expected shedding frequency, $f_0 \sim 0.5$ Hz. The LaVision DaVis PIV software suite was used for calibration, image acquisition, and post-processing. The PIV algorithm used to compute velocity fields consisted of 3 passes with the final

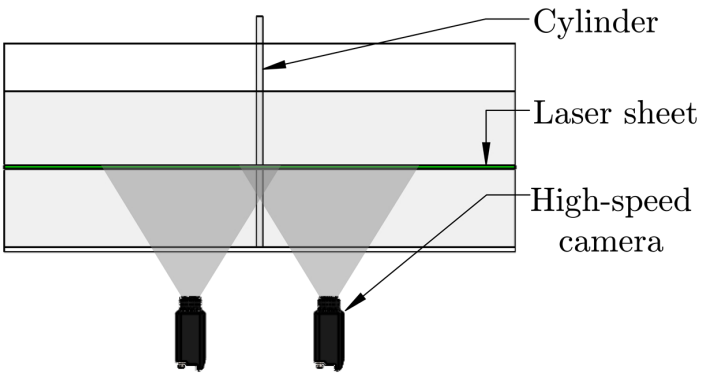

(a)

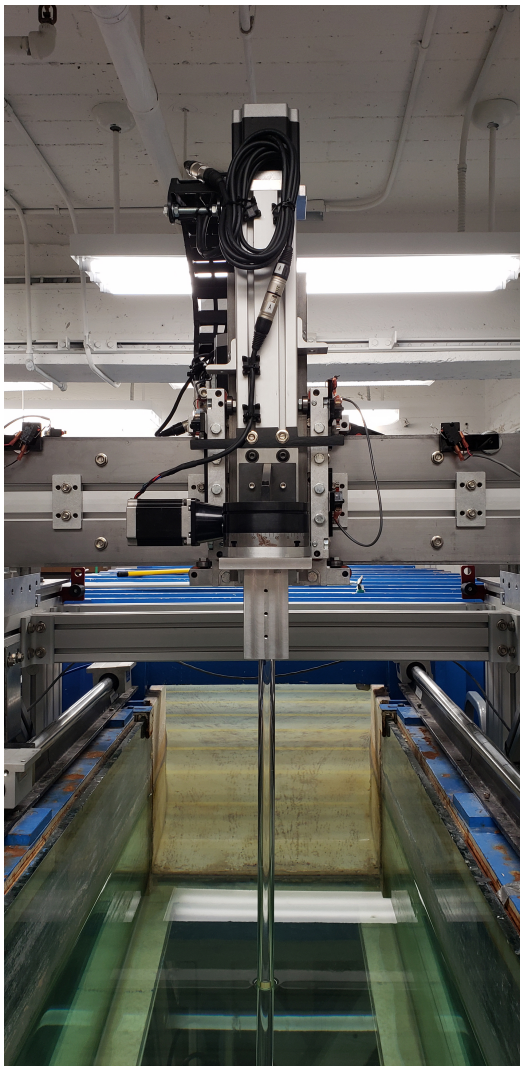

(b)

Figure 2.6: (a) Schematic of PIV setup used in used in oscillating cylinder experiments; (b) clear acrylic cylinder mounted in the test section of the NOAH water channel.

iteration using a 24-by-24 pixel window with 50% overlap. A 3-by-3 smoothing filter was applied after stitching of vector fields to reduce noise.

Besides the full-field information, interrogation points were used to sample the PIV flowfields and facilitate comparison of local and global dynamics. The interrogation points were not separate measurements or probes in the wake, but rather a point in the PIV flowfield from which the velocity was extracted. In the case of the oscillating cylinder, the interrogation point was translated in phase with the cylinder during the forcing cycle to maintain its distance from the cylinder. Similarly, although cylinder flowfields were acquired in the lab-fixed frame, relative to which the body was moving, all subsequent analysis was performed in the cylinder-fixed frame. This is the natural choice as all of the flow structures present in the wake were generated by the cylinder. The frame of reference was changed by re-sampling PIV flowfields using a window fixed to the cylinder. Note that window size was governed by the forcing amplitude, thus high amplitude cases used a smaller cylinder-fixed window. Even though translation of the field of view combined with finite PIV grid resolution led to a small pixelation error, the error was computed to be at most 1.5 mm and did not introduce noticeable artifacts into flowfields or time-traces of velocity.

Full details of the experimental setup and diagnostics used in surface-mounted hemisphere experiments are presented in Carr (2019), but a brief summary is provided here. Flowfields for the surface-mounted hemisphere were acquired using two-dimensional PIV. A Formlabs Form 2 3D printer, with a print resolution of 140 μm, was used to manufacture a surface-mounted hemisphere of radius $R = 20$ mm. The hemisphere was then situated in the spanwise center of the BPWT's test section. A Photonics DM25-527 Nd:YLF laser was pulsed to illuminate 1 μm tracer particles generated using a water and glycerine mixture. The laser sheet was located such that it was concurrent with the hemisphere's streamwise wall-normal plane of symmetry. An IDT MotionPro Y7 camera with a 28mm Nikon Nikkor lens was synchronized with the laser to record images of the illuminated tracer particles at 6 kHz. Vector calculation utilized a sliding sum-of-correlation algorithm implemented in the LaVision DaVis software package. In addition to the flowfield computation presented in Carr (2019), the analysis in the current study incorporated a pre-processing step to reduce high-frequency noise on the order of the sampling frequency. Specifically, PIV time-series were subjected to a temporal finite impulse response (FIR) filter using MATLAB. The cutoff frequency of the low-pass filter was chosen to be 50 Hz, higher than the frequency associated with the dynamics of interest.

2.2.2 Fluorescent Dye Flow Visualization

In addition to PIV, fluorescent dye was used to visualize unsteady flow structures in oscillating cylinder experiments. A dye injection port was located at the upstream stagnation point of the cylinder and (vertically) at the center of the test section. Fluorescent water tracing dye, produced by Ecoclean Solutions, was injected at the upstream stagnation point and illuminated using two HouLight 50 W ultraviolet floodlights. A thin slit was placed in front of the UV floodlights to reduce the beam width and increase contrast in images. The flowrate of the dye was adjusted to ensure no jet was produced which would perturb the cylinder's boundary layers, rather a thin filament of dye advected evenly on both sides of the cylinder and into the wake. A Nikon D600 DSLR camera with an Nikon AF Nikkor 50 mm f/1.8D lens was used to record images of the illuminated dye. In contrast to PIV, where images were acquired in the lab-fixed frame, the DSLR was mounted onto the CTS facing down along the axis of the cylinder, producing images that were acquired in the body-fixed frame.

2.3 Data Analysis and Decomposition

2.3.1 Phase Averaging

It will be shown that harmonic forcing of a cylinder leads to various flow phenomena which are linked to certain points in the forcing cycle. Therefore, phase averaging was employed to gain a deeper understanding of phase-locked dynamics. Only time series acquired using double-pulse PIV were used as they contained more forcing cycles. Phase-averaged flowfields for the streamwise-oscillating cylinder, presented in subsequent chapters, incorporated 42 forcing cycles with each forcing cycle consisting of 129 snapshots. Phase averaging was achieved by separating each time series into individual forcing cycles then averaging across all the cycles (corresponding to the same forcing parameters). Time series corresponding to the surface-mounted hemisphere were not phase averaged as the records did not contain a sufficient number of forcing cycles.

2.3.2 Welch's Method

Welch's method was used to compute the Power Spectral Density (PSD) for mean-subtracted data acquired at the interrogation point. Each time series was separated into sub-windows and the resulting discrete Fourier transforms were averaged to provide an estimate of the power spectral density (PSD) (Welch, 1967). Zero-padded Hamming windows were used, providing higher spectral resolution. Furthermore,

windows sizes corresponded to one-half and one-quarter of the forcing cycle for the cylinder and hemisphere, respectively, and contained no overlap. Note that finite record length, due to limitations in camera memory, resulted in the measurement of fewer cycles for cases with smaller forcing frequencies. This lead to the use of fewer windows in Welch's method which means that interrogation point spectra might not be fully converged for such cases. Although spectra for cases at lower forcing frequencies might not show perfect convergence, they provide sufficient insight into the relevant flow physics to facilitate comparison with global analyses.

2.3.3 Dynamic Mode Decomposition

In subsequent chapters, Dynamic Mode Decomposition (DMD) is used to extract spatio-temporally significant structures from flowfields. DMD appeals to the best-fit linear operator, **A**, representative of system dynamics (Schmid, 2010). Specifically, operator **A** propagates snapshots, **x**, forward in time according to

$$\mathbf{x}_{k+1} = \mathbf{A}\mathbf{x}_k. \tag{2.3}$$

Following Tu et al. (2014), snapshots can also be arranged into two matrices, $\mathbf{X} = [\mathbf{x}_1 \;\; \mathbf{x}_2 \;\; \ldots \;\; \mathbf{x}_{n-1}]$ and $\mathbf{Y} = [\mathbf{x}_2 \;\; \mathbf{x}_3 \;\; \ldots \;\; \mathbf{x}_n]$, allowing expression of Eq. (2.3) as

$$\mathbf{Y} = \mathbf{A}\mathbf{X}. \tag{2.4}$$

DMD refers to the eigen-decomposition of operator **A** in Eq. (2.4). Eigenvalues of **A**, denoted by λ_i and known as DMD eigenvalues, capture the growth rate and frequency of the corresponding DMD mode. Eigenvectors of **A** are referred to as DMD modes and contain the spatial structure associated with the corresponding DMD eigenvalue. The discrete-time formulation of DMD dictates that the unit circle serves as a boundary between stable and unstable eigenvalues. Continuous time eigenvalues can be found from the relation

$$\mu_i = \frac{\log(\lambda_i)}{\Delta t}, \tag{2.5}$$

where Δt represents the time between snapshots. Although **A** can be expressed as

$$\mathbf{A} = \mathbf{Y}\mathbf{X}^{+}, \tag{2.6}$$

where $\mathbf{X}^{+}$ is the pseudoinverse of **X**, the size of experimental datasets often renders the use of Eq. (2.6) computationally intractable. Fortunately, **A** itself need not be calculated in order to find its eigen-decomposition (Tu et al., 2014; Schmid,

2010). Although this can be achieved in many ways, the algorithm for "Exact" DMD presented by Tu et al. (2014) will be used here. Computing the Singular Value Decomposition (SVD) of $\mathbf{X}$,

$$\mathbf{X} = \mathbf{U}\mathbf{\Sigma}\mathbf{V}^*, \tag{2.7}$$

allows definition of

$$\tilde{\mathbf{S}} \equiv \mathbf{U}^*\mathbf{Y}\mathbf{V}\mathbf{\Sigma}^{-1}, \tag{2.8}$$

so that eigenvalues of $\tilde{\mathbf{S}}$ are also eigenvalues of $\mathbf{A}$ (DMD eigenvalues). Therefore, the eigen-decomposition $\tilde{\mathbf{S}}\mathbf{w} = \lambda\mathbf{w}$ is computed to yield the DMD eigenvalues, λ_i, and the DMD modes

$$\phi_i = \frac{1}{\lambda_i}\mathbf{Y}\mathbf{V}\mathbf{\Sigma}^{-1}\mathbf{w}_i. \tag{2.9}$$

Projecting all snapshots in the series onto the DMD modes yields a set of projection coefficients, the mean magnitude of which, α_i, represents each mode's spectral amplitude. The flow can be reconstructed using DMD modes and eigenvalues according to

$$\hat{\mathbf{x}}_k = \sum_{j=1}^{n} \lambda_j^k \alpha_j \phi_j. \tag{2.10}$$

The specific modes used in the reconstruction (Eq. (2.10)) can be truncated to generate a reduced order of model the system.

Under certain conditions, it can be shown that DMD serves an approximation of the Koopman Mode Decomposition (Drmac et al., 2018; Rowley et al., 2009). If conditions are satisfied, DMD modes can be viewed as Koopman modes scaled by the corresponding Koopman eigenfunctions. This connection with the Koopman operator, presented in Section 1.4.3, validates the use of DMD for systems where nonlinear dynamics may develop.

2.3.4 Γ_2 Vortex Identification

Contrary to local vortex identification (vortex ID) algorithms that rely on local gradients at each point in the flow, non-local methods also incorporate a finite region surrounding the point. As a result, non-local methods are better equipped to handle flows with noticeable noise or artifacts. The Γ_2 criterion (Graftieaux et al., 2001), a non-local vortex identification scheme, will be used in this thesis to identify vortex cores in the oscillating cylinder's wake. The Galilean invariance of the Γ_2 criterion makes it a prime candidate for use in non-inertial frames, including those

fixed to an oscillating body. For each point, P, and surrounding region, S, the Γ_2 criterion can be computed a according to

$$\Gamma_2(P) = \frac{1}{A}\int_{M\in S} \frac{[\mathbf{r}\times(\mathbf{u}_M - \tilde{\mathbf{u}}_p)]\cdot\hat{\mathbf{z}}}{||\mathbf{r}||\cdot||\mathbf{u}_M - \tilde{\mathbf{u}}_p||}\mathrm{d}S, \tag{2.11}$$

where $\mathbf{r}$ is the vector from P to M, $\hat{\mathbf{z}}$ is a unit vector orthogonal to S, A is the area of S, and $\tilde{\mathbf{u}}_p$ is the spatially averaged velocity in S. Regions in the flow where $|\Gamma_2| > 2/\pi$ correspond to vortex cores (Graftieaux et al., 2001).

In this thesis, S was taken to be a circle of radius $R = 1.6D$ centered at point P. The Γ_2 peak in each core was tracked between snapshots using the particle tracking code of Tinevez (2019). Trajectories shorter than 3 diameters were discarded as they often corresponded to spurious vorticity. A moving average filter was then applied to each trajectory, reducing fluctuations due to finite grid spacing. Note that the PIV sampling rate was much higher than the time scale associated with vortex convection, thus vortex identification was only applied to every third snapshot.

2.3.5 Sparse Sensor Placement

In full scale applications, access to the complete flowfield around a body is often not feasible. This has motivated significant work on sparse sensor placement at locations where measurements are representative of system dynamics. Not only does sparse sensor placement facilitate design and control, optimal sensor locations can also be used to identify dynamically significant regions of a flowfield. To this end, sparse sensor placement was used to identify optimal sensor positions in the surface-mounted hemisphere's wake.

Although various approaches to sensor placement exist, the methodology of Manohar et al. (2018) was used, as it frames the problem from the perspective of low-order modeling. Manohar et al. (2018) show that for a matrix with columns corresponding to data-driven basis vectors, the QR decomposition can be used to extract optimal sensor locations. More specifically, the pivoted QR decomposition can be applied to a truncated, data-driven basis resulting in a permutation matrix used to identify the optimal sensor locations. The resulting sensor locations provide a greedy solution to the optimal sensor placement problem. Proper Orthogonal Decomposition (POD) was used to generate a data-driven basis for the flowfields considered here. Manohar et al. (2018) show that the resulting sensor locations provide measurements enabling optimal computation of basis vector (POD mode) coefficients in a flow reconstruction. Full details regarding the formulation and theoretical foundation of their framework are presented in Manohar et al. (2018), as well as overlap

related techniques. In this thesis, MATLAB was used to implement the sparse sensor placement procedure outlined above.

2.4 Quasi-Steady Time Scaling

In order to reduce complexity of fluid-structure systems studied in this thesis, a novel time scaling framework is presented. This framework will be used to predict forcing regimes likely to exhibit quasi-steady behavior. Next, time is scaled such that the characteristic frequency exhibited by the system is normalized, alluding to quasi-steady dynamics. In this context, quasi-steady refers to the characteristic frequency of the system. Namely, if the characteristic frequency exhibits strong time-dependent behavior, the system is said to be unsteady. Systems showing an approximately constant characteristic frequency, however, will be denoted as quasi-steady.

2.4.1 Quasisteadiness Parameter

The quasisteadiness parameter, Ω, is developed to identify forcing regimes that coincide with quasi-steady behavior. Consider the effect of simple harmonic forcing with period τ_f on a system with characteristic frequency and period, $f(t)$ and $\tau(t) = \frac{1}{f(t)}$, respectively. An example of such a system is a cylinder generating a Kármán vortex street. Although both the rate of change of the characteristic frequency and period, $\dot{f}$ and $\dot{\tau}$, serve as a proxy to the speed at which system dynamics are changing, they do not both convey the same level of information. Namely,

$$\dot{\tau} = -\frac{\dot{f}}{f^2}. \tag{2.12}$$

Whereas $\dot{f}$ is simply the instantaneous rate of change in frequency, $\dot{\tau}$ also incorporates the instantaneous frequency, f. As will be shown in subsequent chapters, this nuance gives rise to important distinctions elucidating further understanding of system dynamics. Thus, $\dot{\tau}$ will only be considered in the following analysis. Normalizing $\dot{\tau}$ with the quantity

$$\frac{\Delta\tau}{\tau_f} \tag{2.13}$$

where $\Delta\tau = \tau_{max} - \tau_{min}$, the maximum change in characteristic period during the forcing cycle, scales $\dot{\tau}$ and leads to the parameter

$$\Omega(t) = \left|\frac{\Delta\tau}{\tau_f\dot{\tau}}\right| \tag{2.14}$$

referred to as the "quasisteadiness" in the remainder of this thesis. If the dependence of $\tau(t)$ on t is known, $\Omega(t)$ can be computed a priori.

The quasisteadiness parameter, Ω, can be interpreted as a normalized timescale associated with the change in characteristic period. In fact, Segel & Slemrod (1989) use a similar expression, albeit with a chemical concentration instead of τ, to define the slow timescale in a quasi-steady model of a chemical reaction. Consequently, $\Omega \gg 1$ indicates that the timescale associated with changes in the characteristic period is large, thus the temporal behavior of the system evolves relatively slowly and the system may be quasi-steady. It is important to note that large values of Ω do not necessarily guarantee quasi-steady dynamics, especially in cases where the separation of scales between the characteristic and forcing frequency is not large. Rather, high values of Ω allude to portions of the forcing cycle most likely to exhibit quasi-steady behavior and vice-versa.

The quasisteadiness parameter can also be obtained by performing a Taylor series expansion of $\tau(t)$ around an arbitrary time $t = t_0$ giving

$$\tau(t) = \tau(t_0) + \left.\frac{d\tau}{dt}\right|_{t=t_0} (t - t_0) + O(t - t_0)^2. \tag{2.15}$$

Letting $\dot{\tau} = \frac{d\tau}{dt}$, $\Delta\tau = \tau(t) - \tau(t_0)$, $\Delta t = t - t_0$, and rearranging yields

$$\Delta t = \frac{\Delta\tau}{\dot{\tau}|_{t=t_0}}, \tag{2.16}$$

where terms of $O(\Delta t^2)$ have been truncated. Normalizing Eq. (2.16) using the forcing period and taking the absolute value yields

$$\Omega(t) \equiv \left|\frac{\Delta t}{\tau_f}\right| = \left|\frac{\Delta\tau}{\tau_f \dot{\tau}\big|_{t=t_0}}\right|. \tag{2.17}$$

From the Taylor series perspective, $\Omega(t)$ serves as a linear approximation to the number of forcing periods the system would need to spend at the current position along its trajectory in state-space to experience a change in characteristic period equal to $\Delta\tau$. Letting $\Delta\tau = \tau_{max} - \tau_{min}$ produces the quasi-steadiness parameter formulated earlier.

2.4.2 Time Scaling

A simple time scaling can be used to enable quasi-steady analysis of the system with the objective of expressing the time-dependent characteristic frequency, $f(t)$,

in terms of a constant frequency, $\tilde{f}(\tilde{t}) = \tilde{f}$. The periodicity of the system requires that

$$\tilde{f}\mathrm{d}\tilde{t} = f(t)\mathrm{d}t. \tag{2.18}$$

Integration of Eq. (2.18) gives

$$\int_0^{\tilde{t}} \tilde{f}\mathrm{d}\tilde{t} = \int_0^t f(t')\mathrm{d}t' \tag{2.19}$$

$$\iff \qquad \tilde{f}\tilde{t} = \int_0^t f(t')\mathrm{d}t' \tag{2.20}$$

$$\iff \qquad \tilde{t} = \frac{1}{\tilde{f}}\int_0^t f(t')\mathrm{d}t'. \tag{2.21}$$

Equation (2.21) gives the desired expression for the scaled time, $\tilde{t}$, relative to which the characteristic frequency is constant. As an aside, it is observed that the form of Eq. (2.21) resembles the expression used to compute the angle of a frequency modulated signal (Haykin, 2001). Similar to Ω, if the dependence of f on the forcing is known then $\tilde{t}$ can be computed a priori.

2.4.3 Implementation

The quasisteadiness, Ω, can be used to predict quasi-steady regimes in the forcing cycle, but there is no guarantee different quasi-steady regimes all exhibit to the same characteristic frequency. If quasi-steady dynamics are expected, time can be scaled to normalize the frequency exhibited by the system. This can be implemented by sampling data (either in experiments or post-processing) at a rate that is constant relative to the scaled time, $\tilde{t}$. Varying the sampling frequency is akin to allowing the passage of time to contract or dilate so that the observed frequency remains constant, hence the term "time scaling." In this thesis, time scaling will be implemented in post-processing via temporal interpolation of time series according to Eq. (2.21).

Chapter 3

CHARACTERIZATION OF THE STREAMWISE-OSCILLATING CYLINDER'S WAKE

Portions of this chapter will appear in the forthcoming publication:

Shamai, M., Dawson, S. T. M., Mezic, I., and McKeon, B. J. (2021). "Unsteady dynamics in the streamwise-oscillating cylinder wake for forcing frequencies below lock-on". In: *Physical Review Fluids*. DOI: 10.1103/PhysRevFluids.00.004700.

In this chapter, the wake of the streamwise-oscillating cylinder is characterized and the underlying flow physics are discussed. The effect of streamwise forcing on wake dynamics will be presented using both PIV and fluorescent dye flow visualization. Flowfields will be analyzed to show that streamwise forcing manifests both amplitude and frequency modulation in the wake. The stationary case is presented first, however, as it is the reference configuration relative to which oscillating cases will be compared.

3.1 Stationary Cylinder

The wake of the stationary cylinder has been studied extensively and is well characterized (Williamson, 1996). At $Re_0 = 900$, the wake sees the development of the Kármán vortex street highlighted by the shedding of alternating vortices on each side of the cylinder. The stationary cylinder's wake will be referred to as the "steady" configuration. In this context, "steady" refers to the shedding frequency exhibited by the system.

PIV and dye flow visualization both capture the development of vortex shedding. The Kármán vortex street is particularly evident in snapshots from dye flow visualization (Fig. 3.1a). As seen in Figs. 3.1b to 3.1d, PIV flowfields elucidate parts of the flow not accessible by the fluorescent dye. Attention should be drawn to each pair of vertical structures present in the transverse velocity field (Fig. 3.1d), as they correspond to shed vortices. As such, it can be seen that the dominant flow structures present in this flow are clearly captured through consideration of the transverse velocity field, v, alone. This conclusion can also be reached by considering the velocity extracted at the wake interrogation point. It can be seen from Fig. 3.2 that the

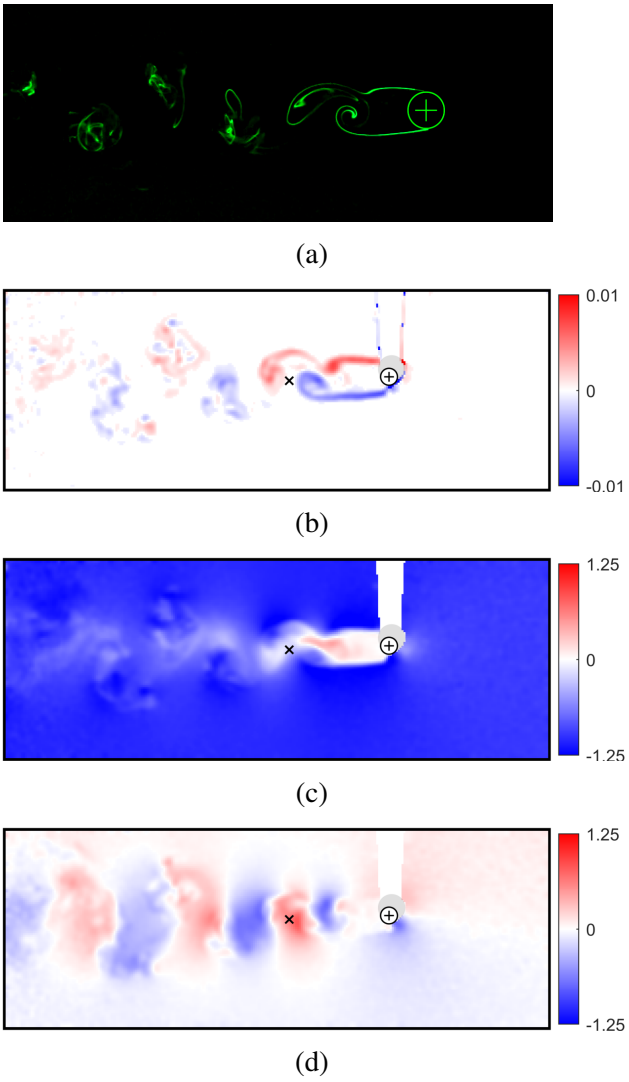

Figure 3.1: Snapshots of (a) fluorescent dye, (b) vorticity, ω_z, (c) transverse velocity, v/U_∞, and (d) streamwise velocity, u/U_∞, for the stationary cylinder. The cross-section of the cylinder at the measurement plane is represented by $\oplus$ and the shaded circle corresponds to an obstruction in the field of view due to the bottom of the cylinder. The location of the interrogation point is denoted by $\times$. Flow is from right to left. $Re_0 = 900$.

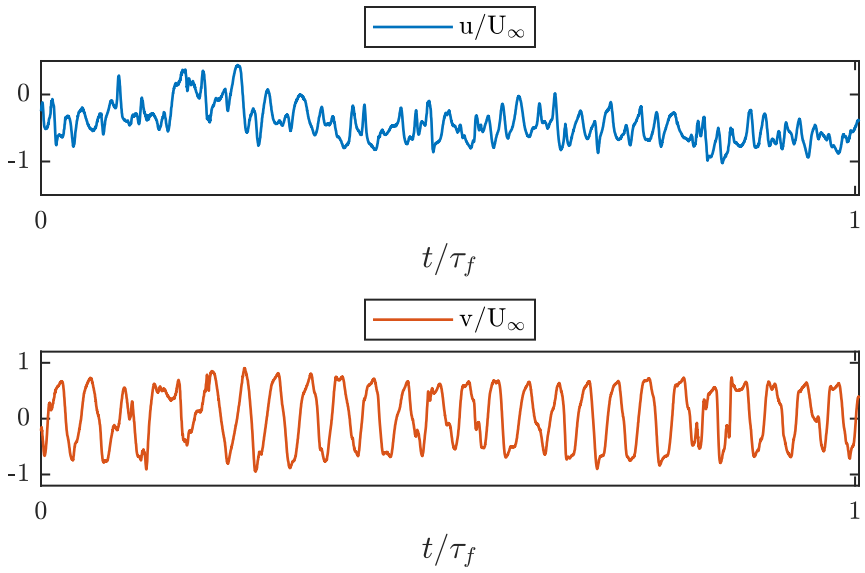

Figure 3.2: Time trace of velocity measured at interrogation point for the stationary cylinder at $Re_0 = 900$.

transverse component of velocity, v, measured at the interrogation point displays an approximately constant oscillation frequency as vortices of opposite sign convect past. (Note that the small deviation near $t/\tau_f \approx 0.25$ can likely be attributed to a fluctuation in the pump driving the water tunnel.) Furthermore, the stationary shedding frequency, corresponding to the peak in the interrogation point spectrum computed for the transverse velocity using Welch's method, is presented in Fig. 3.3. The experimental shedding frequency is almost identical to that predicted in the literature for this Reynolds number, $St \approx 0.21$ (Fey et al., 1998). Consequently, v serves as a good indicator of shedding and oscillatory behavior in the wake and will be the focus of subsequent analysis. Although vorticity fields also capture wake dynamics, the computation of vorticity from PIV flowfields often generates considerable noise which can percolate into further analysis.

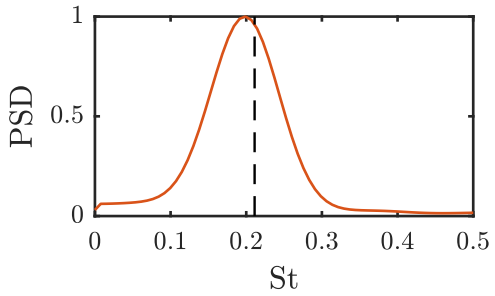

Figure 3.3: Interrogation point spectra for stationary cylinder at $Re_0 = 900$.

3.1.1 Dynamic Mode Decomposition and Power Spectrum

The DMD spectrum corresponding to the stationary cylinder, presented in Fig. 3.4a, also contains a peak coincident with that of the interrogation point, alluding to the extraction of the same shedding frequency. Furthermore, all the DMD eigenvalues for the stationary cylinder (Fig. 3.5) lie on or inside the unit circle, resulting in DMD modes that oscillate periodically or decay with time.

Both the representative DMD modes shown in Fig. 3.4b and the transverse flowfields (Fig. 3.1d) contain similar vertical structures. With the exception of the $St = 0$ mode which is an extraction of the mean flow around the cylinder, the representative modes are clustered around the stationary shedding frequency. It can be inferred that the modes containing these vertical structures are associated with vortex shedding and will henceforth be referred to as "shedding modes." Furthermore, the shedding mode in Fig. 3.4b corresponding to the peak in the DMD spectrum has the cleanest spatial shape, showing minimal noise and contamination from other structures present in the flow. The finite width of the spectral peak and the distribution of multiple shedding modes around it in Fig. 3.4a indicates that shedding in the stationary case might not be purely periodic. Rather, observations of vortex shedding reveal a small band of frequencies about the central value.

3.2 Oscillating Cylinder

The local change in Reynolds number induced by streamwise forcing led to numerous flow phenomena not observed in the stationary case. For a more robust characterization of the oscillating cylinder's wake, dye flow visualization will be combined with both instantaneous and phase averaged PIV. Results are presented for forcing parameters that exemplified the observed phenomena most clearly at each forcing frequency, but similar states were observed for other forcing trajectories as well. Results are presented for one amplitude ratio, $Re_q/Re_0 = 0.35$, and two forcing frequency ratios, $St_f/St_0 = 0.18$ and $St_f/St_0 = 0.036$.

3.2.1 Observed States in the Wake

Instantaneous snapshots of dye-flow visualization and PIV are shown for different phases of the forcing cycle in Fig. 3.6. From left to right, the columns in Fig. 3.6 correspond to $t/\tau_f = 0, 0.25, 0.50$, and 0.75, respectively. At $t/\tau_f = 0$, the wake resembles that of the stationary cylinder with shed vortices of opposite sign convecting downstream. Although the larger scale structure of the wake is similar to the stationary case, streamwise forcing also generates smaller scale structures and

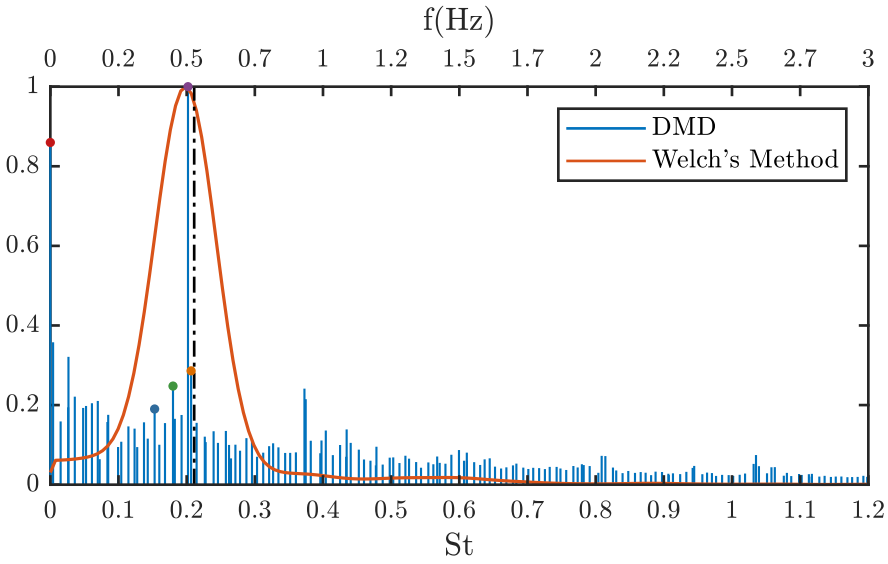

(a)

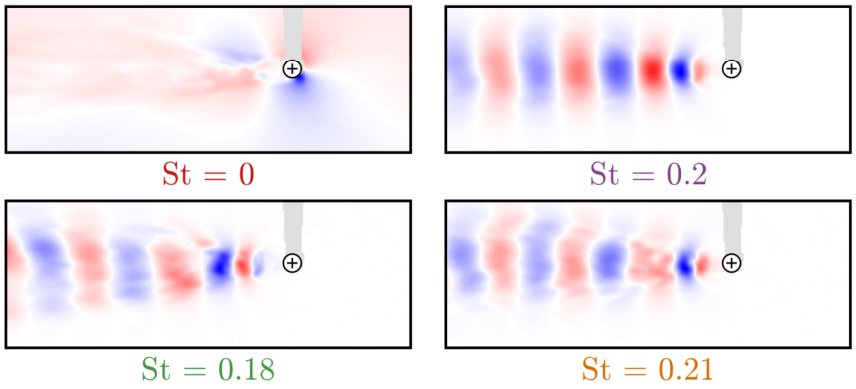

(b)

Figure 3.4: DMD spectrum (a) and modes (b) for the stationary cylinder at $Re_0 = 900$. With the exception of the mean mode ($St = 0$), the colored circles on the spectrum represent shedding modes. The colored mode labels correspond to the circles of the same color on the spectrum. The black dot-dashed line represents the stationary shedding frequency.

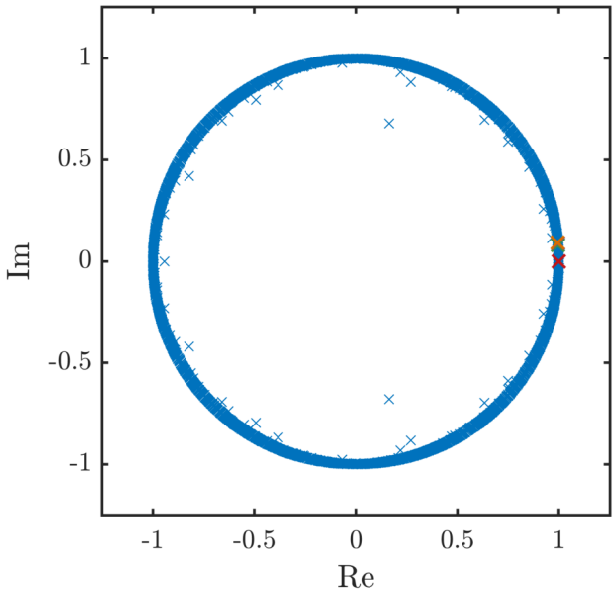

Figure 3.5: DMD eigenvalues for the stationary cylinder at $Re_0 = 900$. The colored symbols correspond to the modes shown in Fig. 3.4.

unsteadiness which can be seen in the velocity and vorticity fields. The cylinder reaches maximum downstream velocity when $t/\tau_f = 0.25$. It can be seen that the strength of shed vortices and the corresponding shear-layers have decreased at this point in the forcing cycle. Although the instantaneous freestream velocity seen by the cylinder at $t/\tau_f = 0$ and 0.50 is identical, the wake at the upstream turnaround point is not similar to its downstream counterpart. In the latter case, the wake no longer resembles that of the stationary cylinder. At $t/\tau_f = 0.50$, the wake is relatively quiescent and the near wake sees the development of two symmetric shear-layers which roll up into a pair of symmetric vortices. The behavior at the downstream turnaround point will be discussed in more detail in Section 3.3.1. At $t/\tau_f = 0.75$, the cylinder attains its maximum upstream velocity and also reaches its most active state. At this point in the forcing trajectory, vortex shedding has resumed and the increase in instantaneous freestream velocity seen by the cylinder leads to stronger shear layers and shed vortices.

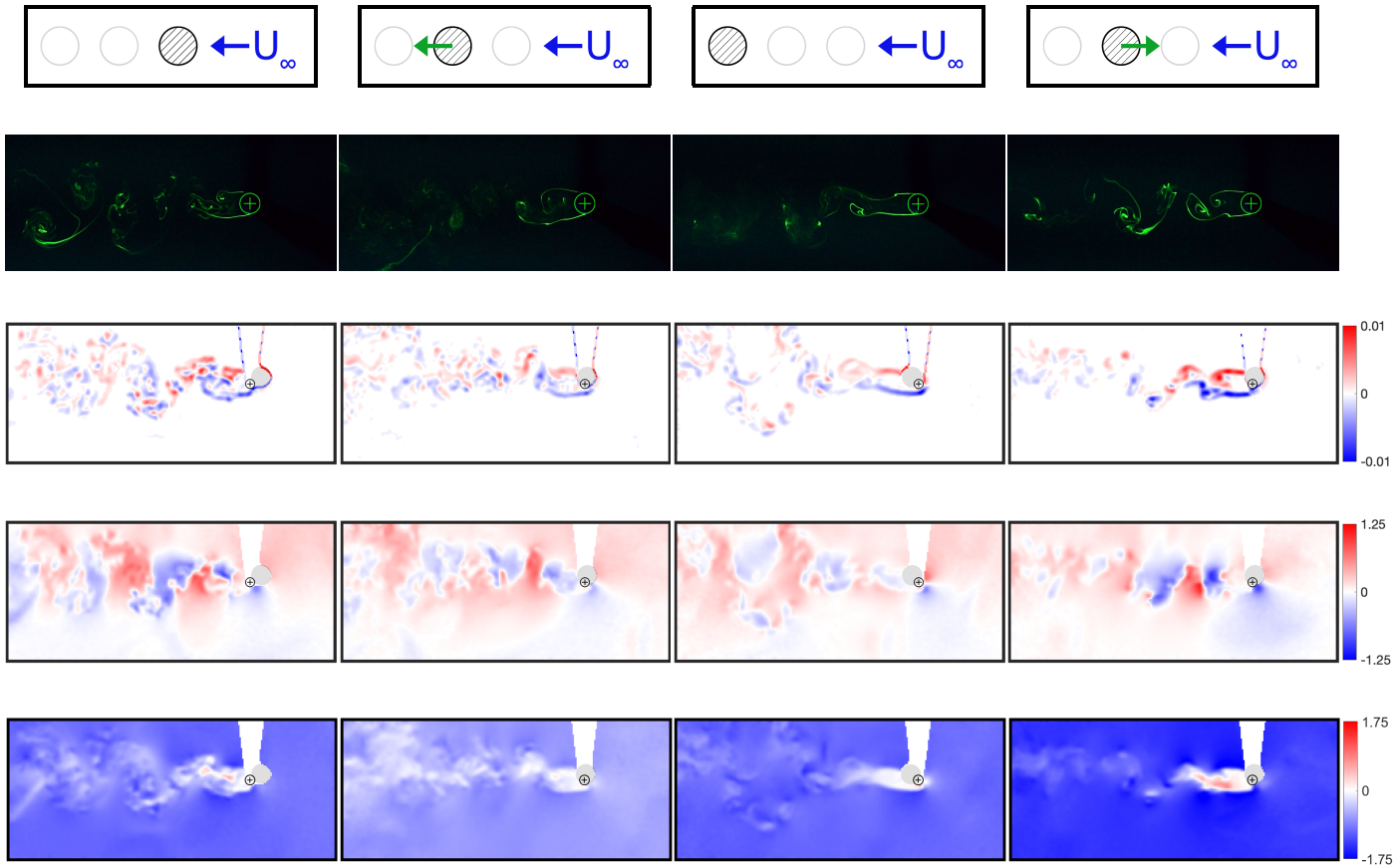

Figure 3.6: Flow around a streamwise oscillating cylinder, $Re_0 = 900$, $\frac{Re_q}{Re_0} = 0.35$, $\frac{St_f}{St_0} = 0.18$. The top row corresponds to the position of the cylinder in the forcing cycle. The second row corresponds to visualization of the flow using fluorescent dye. The third row corresponds to vorticity ω_z. The fourth and fifth rows correspond to the transverse and streamwise components of velocity, $\frac{v}{U_\infty}$ and $\frac{u}{U_\infty}$, respectively. From left to right, the columns correspond to $\frac{t}{\tau_f} = 0, 0.25, 0.50$, and 0.75, respectively. The $\oplus$ symbol represents the cross-section of the cylinder at the measurement plane while the shaded circle represents an obstruction in the field of view due to the bottom of the cylinder. Flow is from right to left.

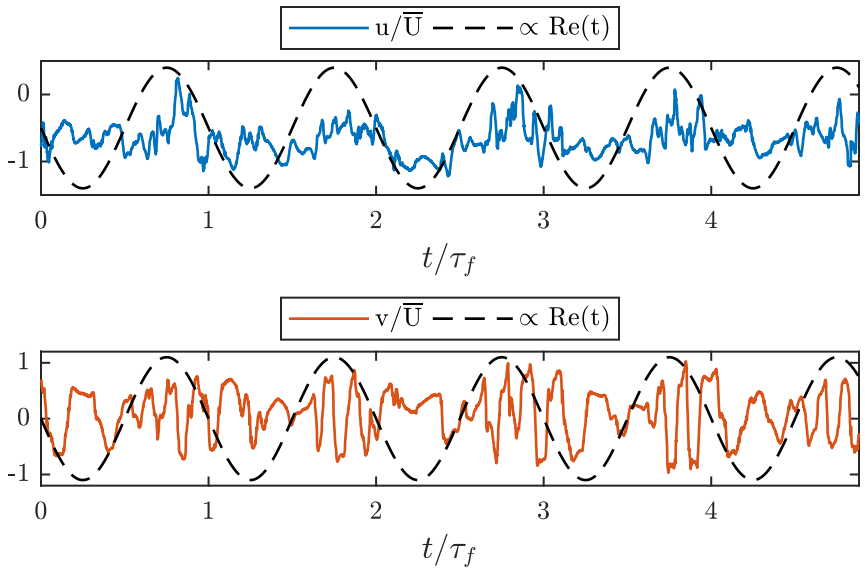

Figure 3.7: Time trace of velocity measured at the interrogation point. The dashed line is proportional to the instantaneous Reynolds number. $Re_0 = 900$, $Re_q/Re_0 = 0.35$, $St_f/St_0 = 0.18$.

One of the most noteworthy effects of streamwise forcing is the development of frequency and amplitude modulation in the wake. As shown in Figs. 3.7 and 3.8, the time trace of velocity probed at the interrogation point elucidates these important features of the flow. From a physical perspective, as the cylinder moves downstream and the shear layers feeding the vortices weaken, more time is required to form and pinch off each vortex. This results in the frequency-modulated signals observed in Figs. 3.7 and 3.8. The large separation between forcing and shedding frequency when $St_f \ll St_0$ leads to a slower change in the instantaneous Reynolds number, thereby resulting in the completion of more shedding cycles at each frequency. This leads to more pronounced frequency modulation for cases at lower forcing frequencies. Frequency modulation will be analyzed more robustly in Chapter 4, while amplitude modulation will be discussed further in Section 3.3.1.

Consideration of the power spectrum provides deeper insight into the frequency modulation. In contrast to the stationary case, local interrogation point spectra for the the oscillating cylinder contain two peaks (Fig. 3.9). The peaks are a direct result of the frequency-modulated shedding frequency. Interestingly, the stationary shedding frequency, indicated by the vertical dashed line, corresponds to a local minimum in the oscillating cylinders' spectra. This indicates that the range of shedding frequencies exhibited by the oscillating cylinder, as observed at

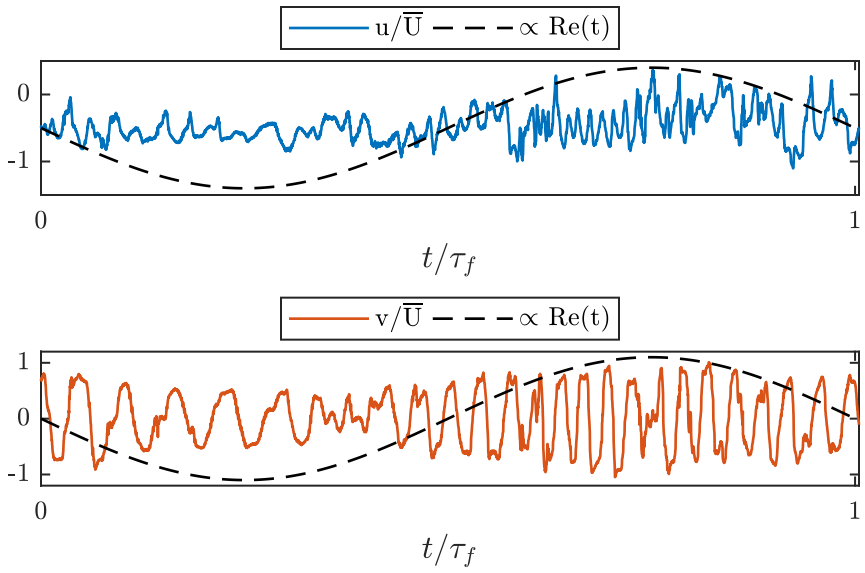

Figure 3.8: Time trace of velocity measured at the interrogation point. The dashed line is proportional to the instantaneous Reynolds number. $Re_0 = 900$, $Re_q/Re_0 = 0.35$, $St_f/St_0 = 0.036$.

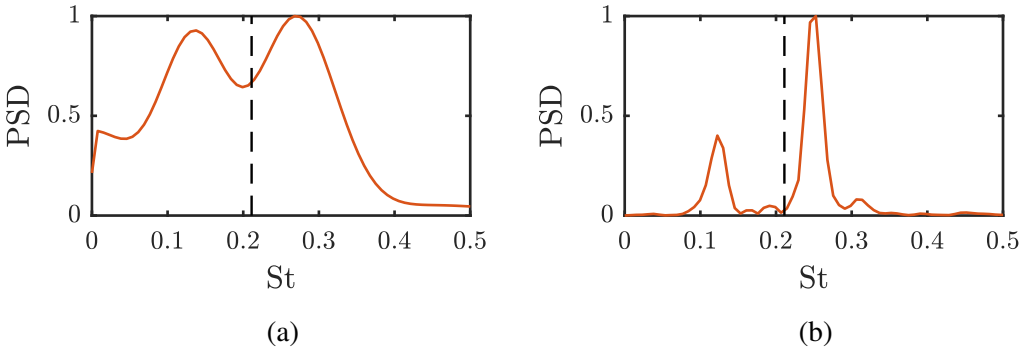

Figure 3.9: Interrogation point spectra corresponding to (a) $Re_q/Re_0 = 0.35$, $St_f/St_0 = 0.18$ and (b) $Re_q/Re_0 = 0.35$, $St_f/St_0 = 0.036$; $Re_0 = 900$.

the interrogation point, is not dominated by the stationary shedding frequency at the mean Reynolds number.

3.2.2 Dynamic Mode Decomposition of the Oscillating Cylinder's Wake

Frequency modulation also changes the structure of the (global) DMD spectra. As with the stationary case, all DMD eigenvalues lie on or inside the unit circle indicating, respectively, neutrally stable or stable modes (not shown). Aside from the zero frequency mode and the mode at the forcing frequency, each of the colored points on the spectra shown in Figs. 3.10a and 3.11a indicate a shedding mode. From the global perspective, frequency-modulated shedding leads to a clustering of

shedding modes away from the stationary shedding frequency. This is evident for the case corresponding to $St_f \ll St_0$ shown in Fig. 3.11a. Two representative shedding modes are shown in Figs. 3.10b and 3.11b corresponding to the strongest shedding mode in each peak. In addition, one mode corresponding to the mean and another at the forcing frequency are presented. Although the multitude of shedding modes each correspond to a slightly different frequency, the associated spatial structures are all similar. A similar phenomena was presented by Arbabi and Mezic (2017) who observed the persistence of structurally similar Koopman modes in lid driven cavity flow over a wide range of Reynolds numbers. The mean and shedding modes for the oscillating case also resemble their stationary counterparts.

It should be noted that the development of a relatively strong but narrow outlying peak near $St \approx 0.4$ in the DMD spectra shown in Fig. 3.10a does not play a significant role in the system's dynamics. The outlying peak corresponds to a transient set of mode pairs with stable eigenvalues indicating decaying mode contribution with increasing time. The mode pairs also contain similar spatial structures (displaying weak coherence and significant noise) but are almost perfectly out of phase resulting in a very small net contribution from the mode pairs to the overall system dynamics. The peak near $St \approx 0.5$ is ignored for the same reason.

Although it is tempting to assume the outlying peaks arise from a nonlinear interaction of the dominant shedding modes (shown in Fig. 3.10b), the frequency of the dominant shedding modes do not sum to give the frequency of the outlying peaks in question. Thus, the outlying peak is likely not a result of nonlinear interactions between shedding modes. This is not to say, however, that nonlinear interactions do not play a role in the flow. Future work could consider the role of nonlinear interactions associated with secondary flow structures to extract the physical mechanism associated with the transient modes in the outlying peak. In the context of this thesis, however, it will be shown that the linear approach incorporated herein, combined with quasi-steady time scaling, suffices to model the observed shedding dynamics.

Results of Dynamic Mode Decomposition corresponding to cases with different forcing trajectories (not shown) are briefly summarized here. When Re_q is fixed but forcing frequency is decreased by an order of magnitude, additional shedding modes are extracted from the time-series. These additional shedding modes arise from the gradual modulation of the shedding frequency during the forcing period. On the other hand, increasing forcing amplitude, Re_q, but holding all other pa-

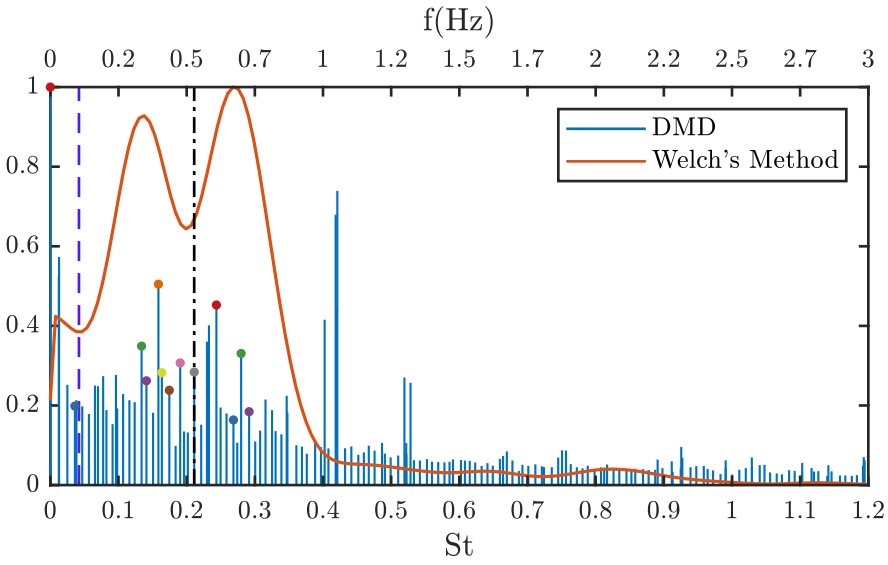

(a)

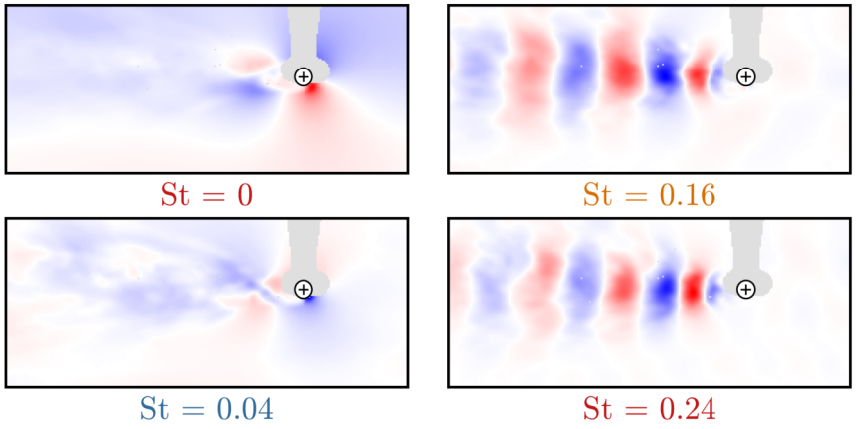

(b)

Figure 3.10: DMD spectrum (a) and modes (b) for oscillating cylinder, $Re_0 = 900$, $Re_q/Re_0 = 0.35$, $St_f/St_0 = 0.18$. The colored mode labels correspond to the circles of the same color on the spectrum. The black dot-dashed line represents the stationary shedding frequency while the purple dashed line denotes the forcing frequency. The additional colored symbols on the spectrum indicate shedding modes.

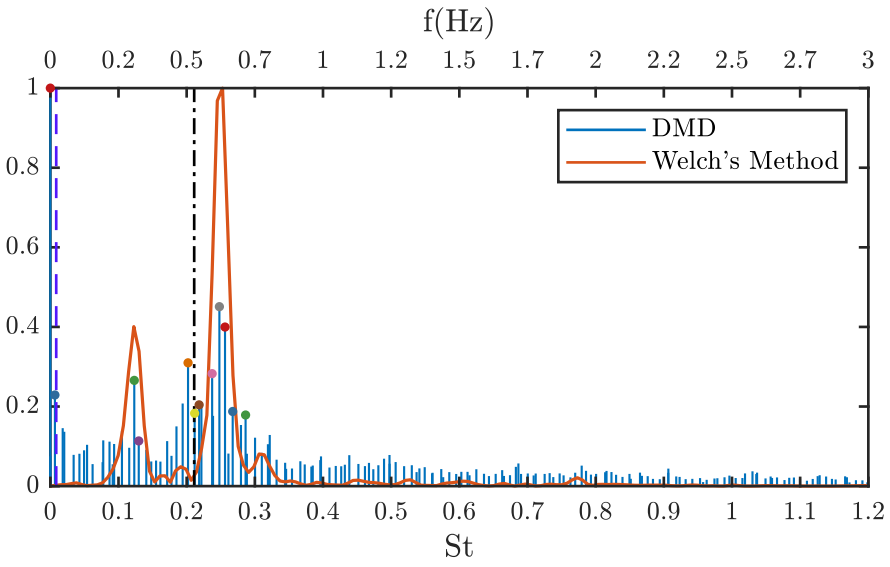

(a)

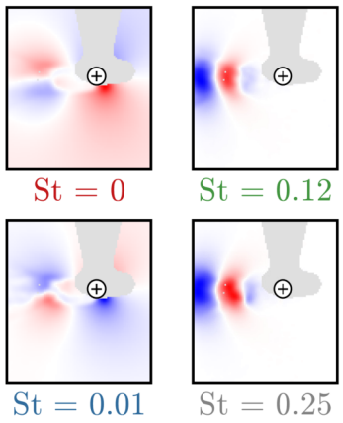

(b)

Figure 3.11: DMD spectrum (a) and modes (b) for oscillating cylinder, $Re_0 = 900$, $Re_q/Re_0 = 0.35$, $St_f/St_0 = 0.036$.

rameters constant led to an increase in separation between spectral peaks, both in the interrogation point and DMD spectra. Raising Re_q also increased the width of spectral peaks, a phenomenon also seen by Glaz et al. (2017), albeit at lower Reynolds numbers.

3.3 Vortex Dynamics

It was shown that streamwise forcing manifests a range of flow phenomena not observed in the stationary case. Given that the dominant structures in this flow regime are vortices, the effect of the forcing cycle on their dynamics plays an important role in system dynamics.

3.3.1 Starting Vortex Generation

As discussed in Section 3.2.1 and shown in Fig. 3.6, the wake of the streamwise-oscillating cylinder takes on symmetry in the vicinity of the downstream turnaround point at $t = \frac{1}{2}\tau_f + k\tau_f$. Consideration of both dye flow visualization and phase-averaged flowfields facilitates understanding of this phenomenon from both a qualitative and quantitative perspective. As the cylinder moves downstream and the instantaneous freestream velocity seen by the cylinder decreases, the shear-layers weaken and move away from each other. On the other hand, as the cylinder moves upstream, the instantaneous freestream velocity seen by the cylinder increases, and the shear-layers strengthen and move inward. This contraction and narrowing of the wake is particularly evident in the phase-averaged vorticity fields of Fig. 3.12. As an aside, it is observed (and expected) that phase-averaging reduces the observability of vortex shedding in the wake.

As the relative velocity seen by the cylinder begins to increase, the symmetric shear layers roll up into two symmetric vortices, one on either side of the cylinder. This state is seen in Fig. 3.13a as two symmetric filaments of dye located across the cylinders centerline. As the cylinder starts moving upstream, the two symmetric vortices increase in strength. Eventually, the two-vortex system becomes unstable resulting in the growth of perturbations and asymmetry, leading to the resumption of vortex shedding (Figs. 3.13b to 3.13f). Streamlines of the phase-averaged flow, shown in Fig. 3.14, also reveal the aforementioned behavior at the downstream turnaround point. As the cylinder approaches its furthest position downstream, initially smooth streamlines close in a symmetric manner about the wake centerline. The development of these closed streamlines alludes to the generation of the two symmetric vortices downstream of the cylinder.

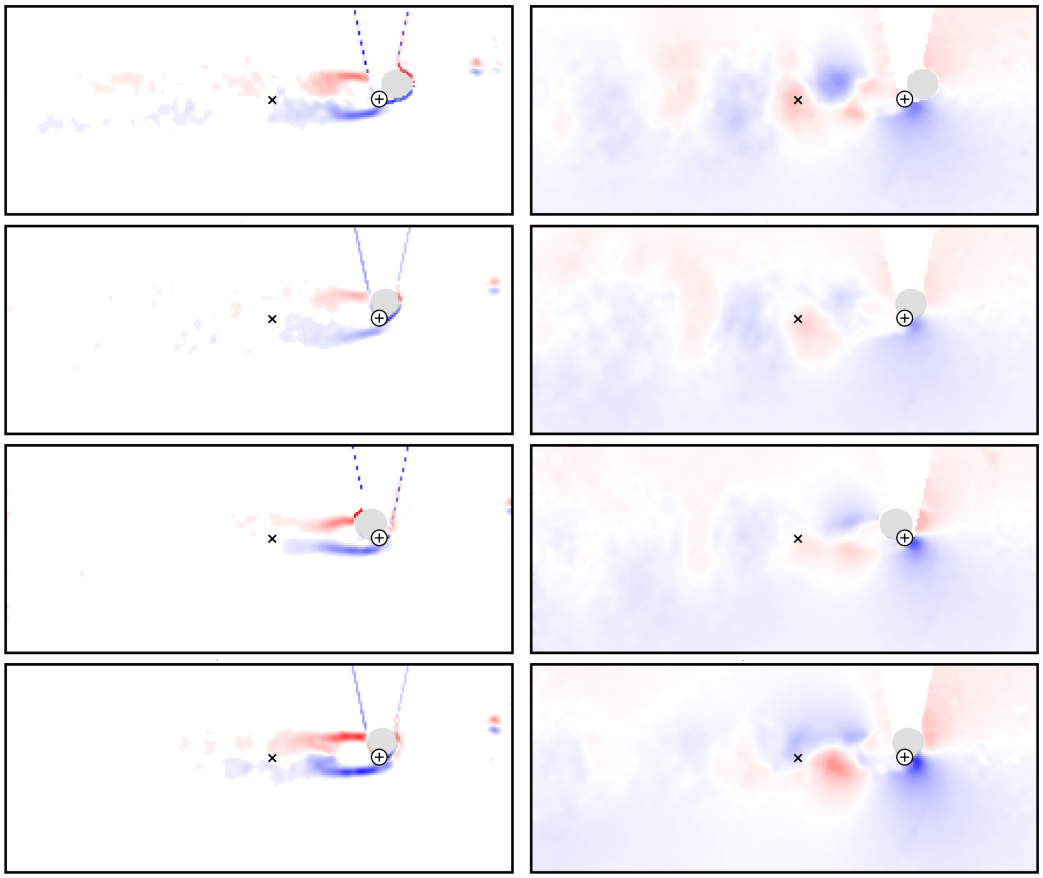

Figure 3.12: Phase averaged vorticity (left) and transverse velocity (right), $Re_0 = 900$, $Re_q/Re_0 = 0.35$, $St_f/St_0 = 0.18$. From top to bottom, snapshots correspond to $t/\tau_f = 0$, $t/\tau_f = 0.25$, $t/\tau_f = 0.50$, and $t/\tau_f = 0.75$, respectively.

The symmetric flow structures at the downstream turnaround point also resemble the development of so-called "starting vortices" in the wake of an impulsively started cylinder (Bouard and Coutanceau, 1980). As a cylinder is impulsively started from rest, two symmetric starting vortices are generated in the near wake before vortex shedding begins. Thus, the symmetric vortices in the streamwise-oscillating cylinder's wake will be referred to as starting vortices in the remainder of this thesis. It should be noted that even though the closed streamlines in Fig. 3.14 resemble the mean recirculation bubble in the wake of a stationary cylinder, they persist for only a short duration in the vicinity of the turnaround point. The symmetric roll up of dye filaments is also anchored to the same phase in the forcing cycle. Therefore, it is deduced that the streamline pattern is not an extraction of the cylinder's recirculation bubble via phase averaging but rather a footprint of the starting vortices.

The development of amplitude modulation is intimately linked to the generation of

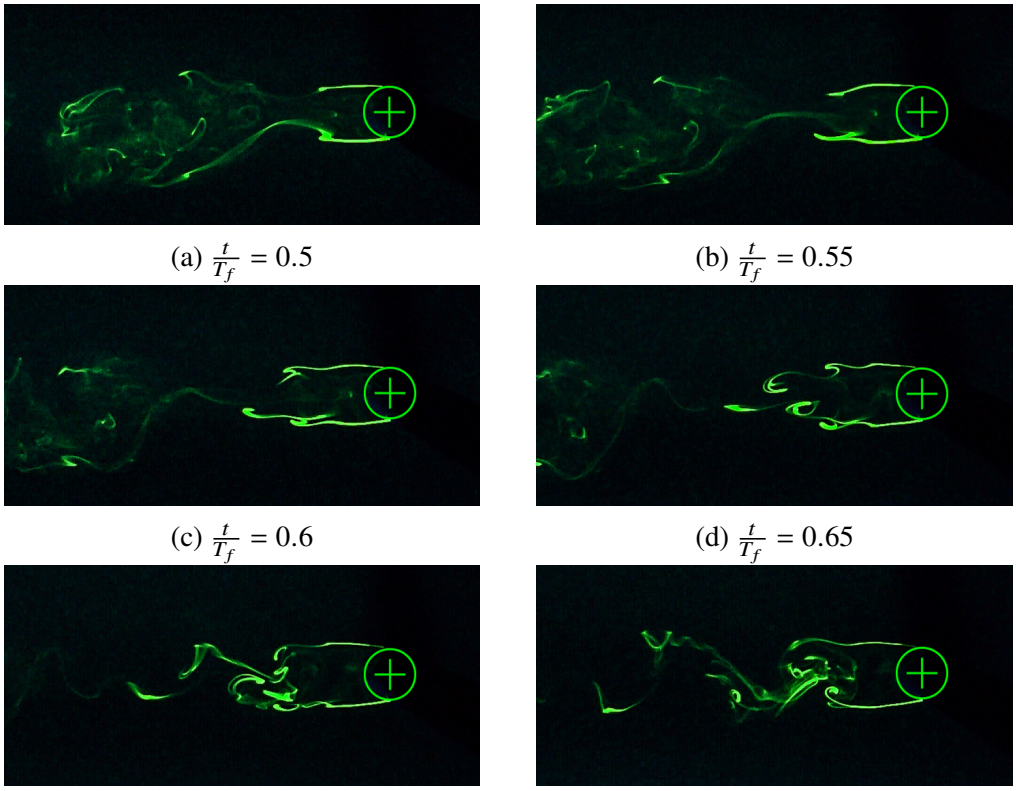

(a) $\frac{t}{T_f} = 0.5$ (b) $\frac{t}{T_f} = 0.55$

(c) $\frac{t}{T_f} = 0.6$ (d) $\frac{t}{T_f} = 0.65$

(e) $\frac{t}{T_f} = 0.7$ (f) $\frac{t}{T_f} = 0.75$

Figure 3.13: Flow visualization showing the generation and evolution of starting vortices.

these starting vortices. As a result of the symmetric flow pattern, asymmetric shedding is suppressed and oscillatory amplitude decreases. As the cylinder moves upstream and shedding resumes, however, an oscillatory signal is once again observed. Thus the interplay in wake symmetry leads to amplitude modulation. It should be noted that amplitude modulation was more pronounced in cases corresponding to higher forcing frequencies because increased acceleration at the turnaround point resulted in the generation of stronger starting vortices.

The vortex formation time, as presented by Jeon and Gharib (2004) for bluff body wakes, further elucidates the transition from symmetric starting vortices to alternate vortex shedding after the turnaround point. When the formation time exceeds a critical value, the circulation in wake vortices saturates and the introduction of additional circulation leads to secondary flow structures and asymmetry. Following Jeon and Gharib (2004), the vortex formation time for a bluff body wake can be defined as

$$t^* \equiv \frac{\overline{U}t}{D} = \frac{L}{D}, \tag{3.1}$$

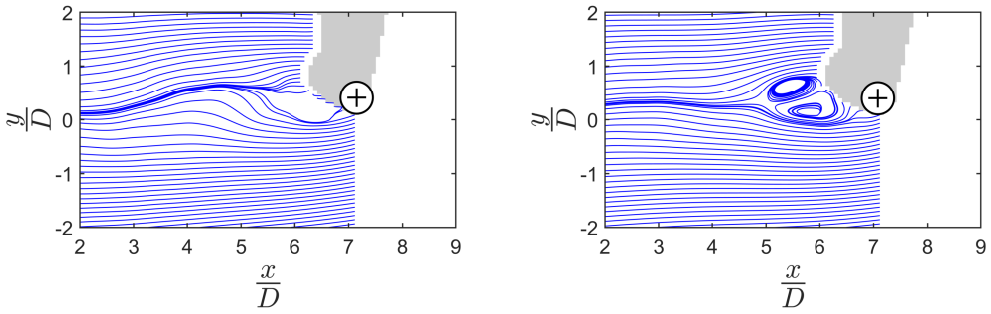

Figure 3.14: Streamlines of phase-averaged velocity field before formation of starting vortex at $t/\tau_f = 0.4$ (left) and during formation of starting vortex $t/\tau_f = 0.5$ (right). $Re_0 = 900$, $Re_q/Re_0 = 0.35$, $St_f/St_0 = 0.18$.

where $\overline{U}$ denotes the mean velocity from time $t = t_0$ to t and L represents the path distance traveled by the cylinder. For an impulsively started cylinder, Jeon and Gharib (2004) show that starting vortices first develop asymmetry when $t^* \approx 4$. For a cylinder oscillating in the streamwise and transverse directions, on the other hand, they show that the total path distance traveled during a forcing cycle dictates wake dynamics. Specifically, Jeon and Gharib (2004) show that if the total path distance per forcing cycle exceeds that traveled by a cylinder moving at the freestream velocity, vortices in the wake saturate and secondary vortices can arise. The latter definition for the formation time, based on total path distance per cycle, can easily be extended to the streamwise forcing considered in this thesis. In order to extend the former definition, however, t_0 is taken as the phase in the forcing cycle where the relative velocity seen by the cylinder reaches zero and begins increasing, the portion of the forcing cycle analogous to an impulsively started cylinder. Given that the forcing frequencies considered in this thesis are relatively small, it will be shown that certain forcing regimes resemble an impulsive start while others are similar to the lock-on case.

The vortex formation time, computed according to the two definitions above, is shown for $St_f < St_0$ in Fig. 3.15. It is evident that the total path distance, L/D, per forcing cycle exceeds the critical value, denoted by the horizontal dashed line. This alludes to saturation of primary wake vortices and the resulting generation of secondary vortical structures. Note that secondary flow structures observed in this forcing regime will be discussed further in subsequent sections. The formation time computed according to the definition for an impulsively started cylinder, on the other hand, indicates symmetry breaking just before the downstream turnaround point. This is in contrast to the observation of symmetric starting vortices which develop

at the downstream turnaround point for $St_f < St_0$. Consequently, for cases at higher forcing frequencies, vortex formation and the resulting dynamics at the downstream turnaround point are more closely related to the lock-on regime.

The formation time points to different behavior at smaller forcing frequencies, namely, $St_f \ll St_0$. From Fig. 3.16 it can be seen that the total path distance exceeds the critical value quite significantly. Although this indicates significant generation of secondary flow structures, the flowfields show otherwise. In contrast, fewer secondary flow structures are observed in this regime and they are considerably weaker than those observed at higher forcing frequencies. It is also observed that forcing regimes corresponding to $St_f \ll St_0$ develop a symmetric wake considerably earlier (i.e. before the downstream turnaround point). The formation time corresponding to an impulsive start sheds light on this phenomenon. In particular, Fig. 3.16 shows that the formation time for an impulsive start surpasses the critical value near $t/\tau_f \approx 0.25$, indicating the development of wake symmetry and subsequent onset of asymmetry before the downstream turnaround point, in good agreement with experiments. Jeon and Gharib (2004) also note a slow transition from symmetric starting vortices to asymmetric shedding for very low accelerations. A similar trend is observed for streamwise forcing cycles corresponding to $St_f \ll St_0$ and is likely responsible for the less pronounced amplitude modulation observed in Fig. 3.8. All in all, it can be seen that wake dynamics for lower forcing frequencies are in better agreement with the formation time defined for an impulsive start. Therefore, dynamics in this regime are more closely related to that of an impulsively started cylinder, as opposed to an oscillating cylinder within the lock-on regime.

Dynamic Mode Decomposition of the phase-averaged velocity fields is presented in Fig. 3.17 and provides a link between starting vortex generation and DMD of the instantaneous PIV time series. As expected, phase averaging leads to a reduction in activity in the frequency range for vortex shedding, a trend which should continue with increasing record length. The emergence of an anti-symmetric flow structure at the forcing frequency, henceforth referred to as the "forcing mode," can be seen in the bottom left panel of Fig. 3.17b. The anti-symmetric structure in the forcing mode is located at the same location as the starting vortices and contains adjacent structures of opposite sign, indicative of a vortex. Thus, the forcing mode is an extraction of a flow structure associated with the starting vortices. It has previously been shown that the phase-averaged velocity field is directly related to the Koopman

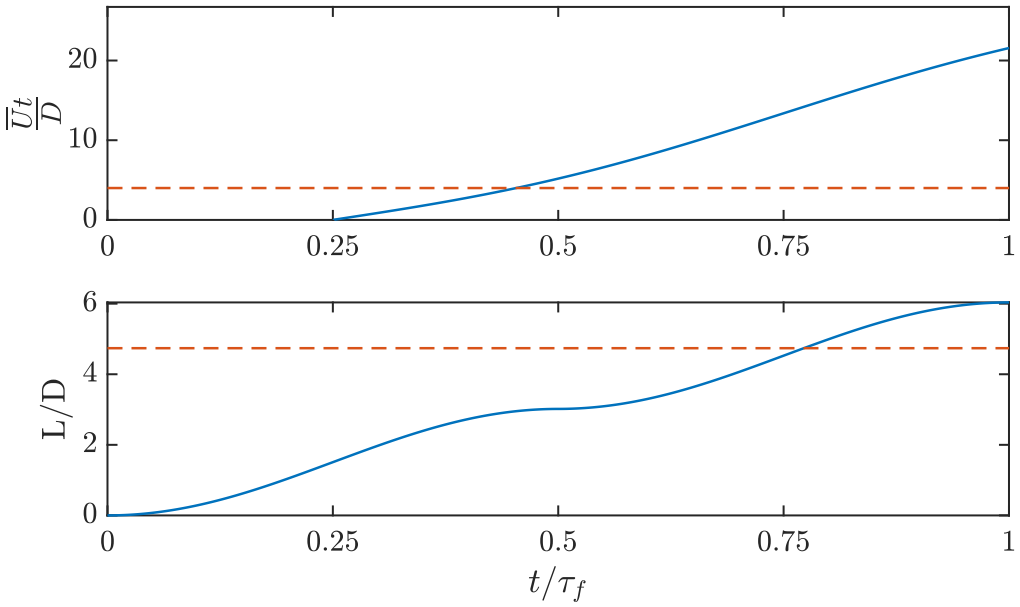

Figure 3.15: Vortex formation time for the streamwise-oscillating cylinder. Dashed horizontal lines correspond to critical value based on the respective definition. $Re_0 = 900$, $Re_q/Re_0 = 0.35$, $St_f/St_0 = 0.18$.

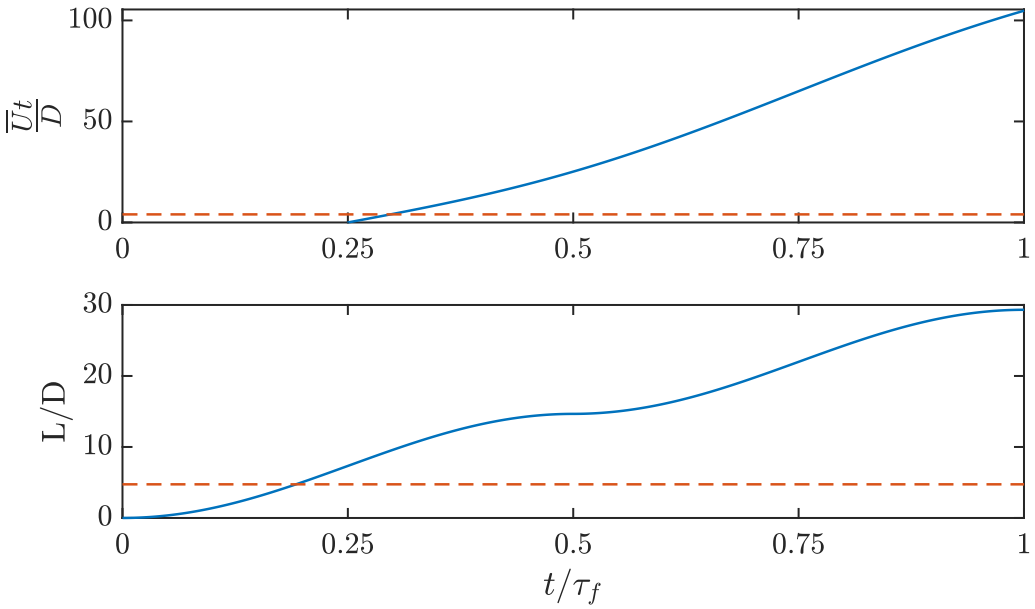

Figure 3.16: Vortex formation time for the streamwise-oscillating cylinder. $Re_0 = 900$, $Re_q/Re_0 = 0.35$, $St_f/St_0 = 0.036$.

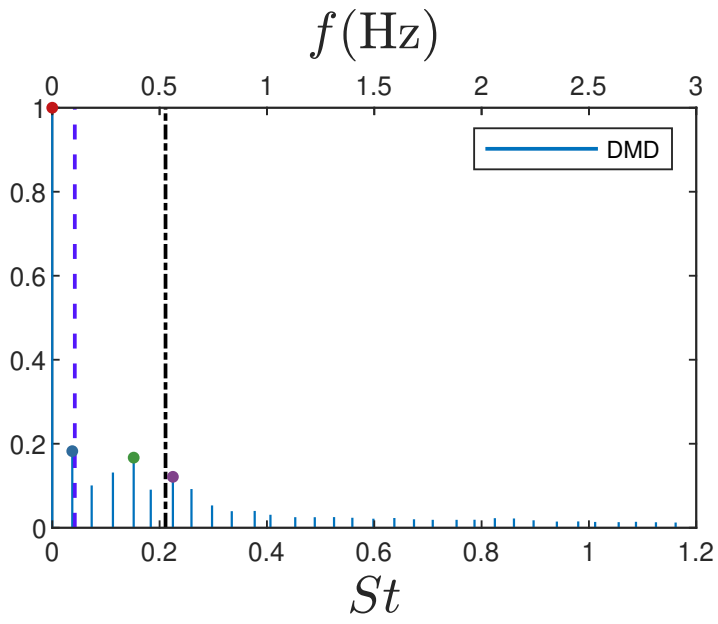

(a)

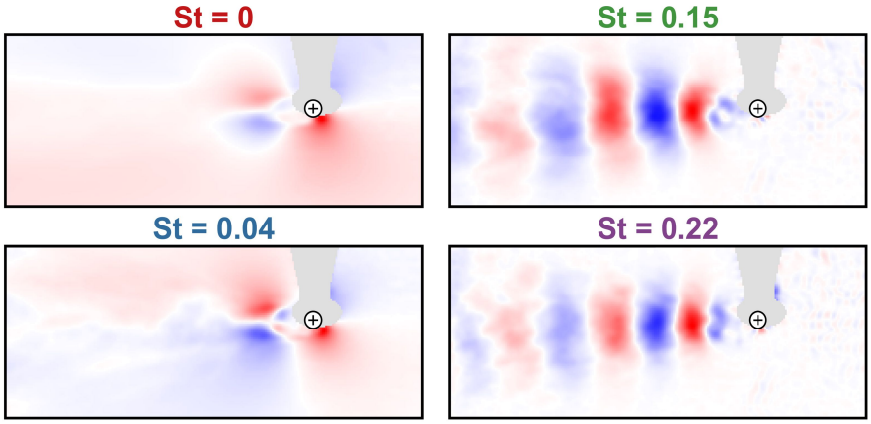

(b)

Figure 3.17: DMD spectrum (a) and modes (b) for phase-averaged time series, $Re_0 = 900$, $Re_q/Re_0 = 0.35$, $St_f/St_0 = 0.18$. Note that phase averaging leads to a lower frequency resolution in the DMD spectrum.

mode at the averaging frequency (Mezic, 2005). Hence, the forcing mode extracted in the phase-averaged case may be related to the dynamics of the non-phase-averaged system via this connection with the Koopman operator. Indeed, footprints of the anti-symmetric forcing mode can be seen in cases that are not phase-averaged (Fig. 3.10b, Fig. 3.11b).

Although the range of forcing frequencies considered here do not overlap with those

required for the canonical lock-on phenomena, the generation of starting vortices at the downstream turnaround point is synchronized with the forcing. In contrast to the classical lock-on case where the vortex shedding frequency is proportional to the forcing frequency, the generation of starting vortices can be thought of as a "pseudo" or "partial" lock-on state. Specifically, the frequency of starting vortex generation is proportional to the forcing frequency even though the vortex shedding frequency is not.

3.3.2 Vortex Identification

The trajectory of each vortex also takes on different behavior in the presence of streamwise forcing. Vortex core trajectories are computed using the Γ_2 metric following the approach described in Section 2.3.4. For comparison with the reference configuration, vortex dynamics in the stationary case are considered first. From Fig. 3.18, it can be seen that the underlying vorticity field may suffice to identify vortices in the near wake, but further downstream fluctuations hinder such an approach. Application of the Γ_2 criterion, however, clearly identifies vortices regardless of their streamwise distance from the cylinder. Vortex core trajectories are shown in Fig. 3.19 along with the corresponding convection speed along the trajectory. It can be seen that the trajectories exhibit approximate symmetry across the cylinder's centerline. Nearly all vortices follow the same qualitative trajectory, although individual trajectories occasionally show deviations. The relatively weak inflection point at $x/D \approx 1$ corresponds to the location where individual vortices are pinched off from the shear layer and begin to convect downstream. After pinch-off, each vortex convects downstream at a very slight angle away from the centerline, resulting in a gradual increase in wake width. It can be seen that after traveling approximately 10 diameters downstream, the convection speed approaches the freestream value, which is maintained as the vortices continue downstream. The small drop in convection speed at the end of each trajectory in Fig. 3.19 is a result of vortex tracking applied to the core as it leaves the field of view.

The aforementioned differences manifested in the cylinder wake due to streamwise forcing lead to vortex trajectories that differ from the stationary case. In addition to the suppression of asymmetric shedding at the midpoint of the forcing cycle, a number of other effects are observed. Application of the Γ_2 criterion to the oscillating cylinder's wake is shown at various phases in Fig. 3.20. As the cylinder moves downstream and vortex shedding frequency decreases, resulting vortices are weakened. Consequently, fewer vortices are detected using the Γ_2 criterion

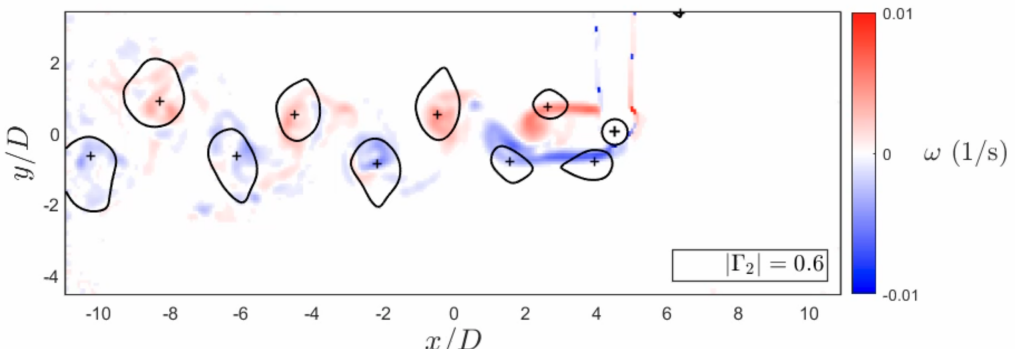

Figure 3.18: Instantaneous snapshot of vortex identification via the Γ_2 criterion for a stationary cylinder at $Re_0 = 900$.

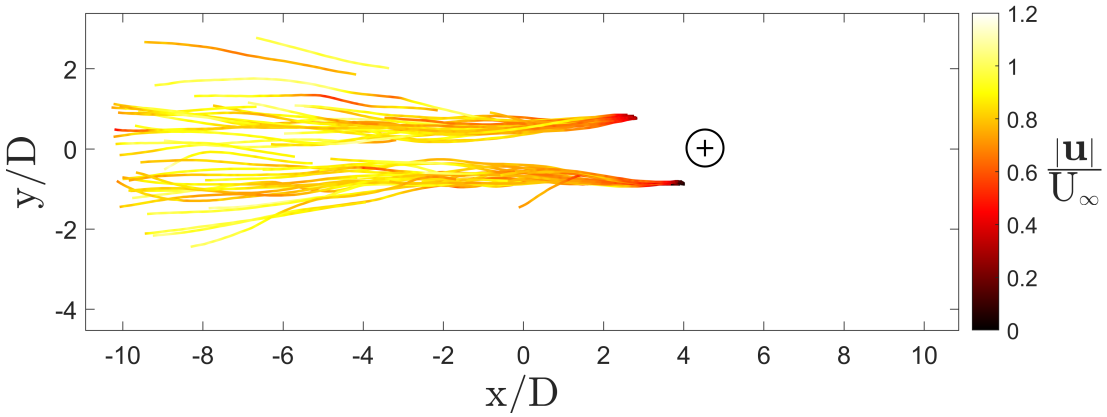

Figure 3.19: Vortex trajectories in the stationary cylinder's wake at $Re_0 = 900$. Trajectories on the top of the cylinder start further downstream due to PIV shadow.

(Fig. 3.20a). At the downstream turnaround point, vortices are not immediately identified in the near wake (Fig. 3.20b) as that point corresponds to wake symmetry immediately before generation of starting vortices. Note that the structure at that instant located just below the cylinder is the separated shear layer. The latter half of the forcing cycle coincides with strong shedding resulting in the identification of multiple well-defined vortices (Fig. 3.20c). In addition to the identification of shed vortices, the Γ_2 criterion also detects pockets of spurious vorticity near the top and bottom of the field of view. These structures, which are not physical, can likely be attributed to the cylinder motion combined with the large field of view resulting in spurious laser reflections in some images.

The behavior observed during the two halves of the forcing cycle motivate analysis of vortex trajectories in the oscillating case differently. Whereas trajectories for the full forcing cycle are not easily deciphered (Fig. 3.21a), separate consideration

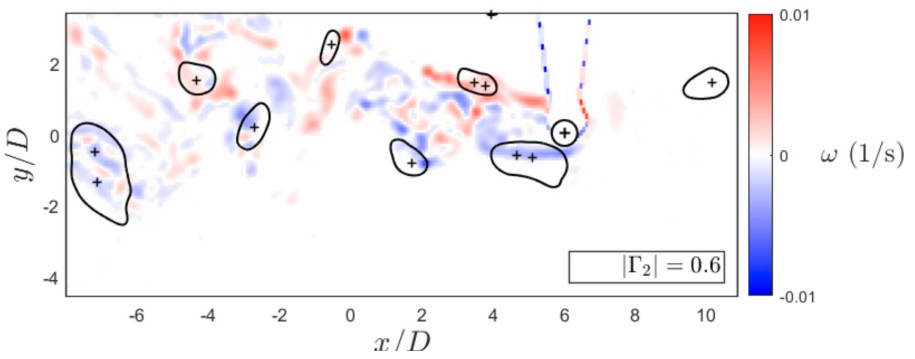

(a) $t/\tau_f = 0.25$

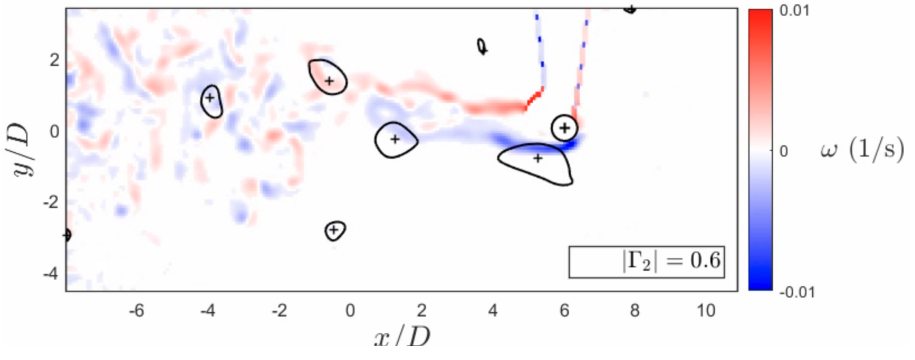

(b) $t/\tau_f = 0.5$

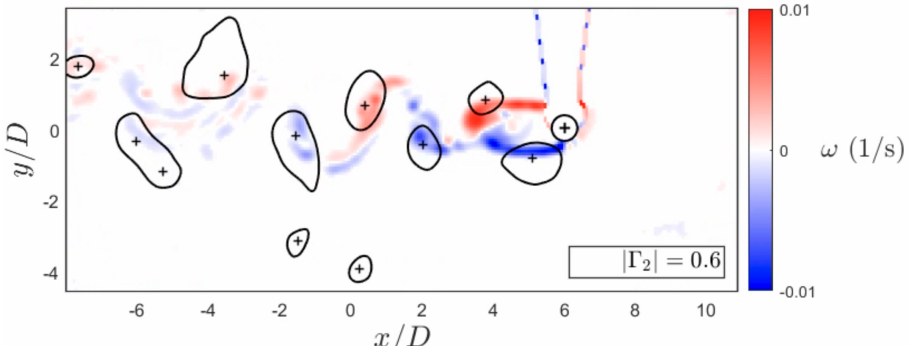

(c) $t/\tau_f = 0.75$

Figure 3.20: Instantaneous snapshot of vortex identification via the Γ_2 criterion for an oscillating cylinder. $Re_0 = 900$, $Re_q/Re_0 = 0.35$, $St_f/St_0 = 0.18$.

of each half of the cycle gives insight into the dynamics. Specifically, Fig. 3.21b shows that as the cylinder moves downstream, the the relative velocity experienced by the cylinder decreases, resulting in reduced vortex convection velocities. As a result, vortices exhibit a longer residence time in the near wake, yielding shorter trajectories. It should be noted that although the convection velocity decreases during the first half of the cycle, it is still higher than the downstream velocity of the cylinder. The reduced shedding frequency during this portion of the cycle also results in the identification of fewer trajectories. Unlike the stationary case where trajectories primarily follow a repetitive smooth path, the same does not hold true for the downstroke of the oscillating cylinder. The reduced convection speed during this portion of the cycle means that transverse velocity fluctuations, due to the background flowfield and interactions with other vortices, play a larger role in determining the trajectory. Consequently, vortex trajectories corresponding to the first half of the forcing cycle show significant fluctuations in the transverse direction. The opposite holds true for the latter half of the forcing cycle. The increase in instantaneous Reynolds number leads to a higher shedding frequency, resulting in identification of additional trajectories as seen in Fig. 3.21c. Furthermore, the relative increase in freestream velocity reduces the effect of fluctuations leading to smooth trajectories similar to the stationary case. Vortices also convect at a higher speed during this half of the cycle, leading to longer trajectories.

As alluded to in the discussion of the vortex formation time, streamwise forcing also led to the generation of secondary vortices in the wake, an example of which is shown in Fig. 3.22. Secondary vortices were observed in the latter half of some forcing cycles with seemingly random occurrence. During the upstroke of the forcing cycle, it was observed that the shear layers exhibited a Kelvin-Helmholtz (K-H) style instability and roll up. When this occurred, the K-H vortices followed two possible trajectories. They either merged with other vortices of the same sign in the near wake and were subsequently shed downstream, or instead, they were shed as individual secondary vortices. Secondary vortex generation is possibly also related to increased wake sensitivity during the cylinder's upstream motion. Specifically, as the relative velocity experienced by the cylinder increases, the boundary layer thins, resulting in a higher sensitivity to external perturbations. Even small perturbations, such as cylinder vibrations, could destabilize the boundary layer and generate secondary vortical structures. Although the Captive Trajectory System (CTS) was configured such that the forcing followed a smooth trajectory, small cylinder vibrations could still arise due oscillating hydrodynamic load acting on the cantilevered, high aspect

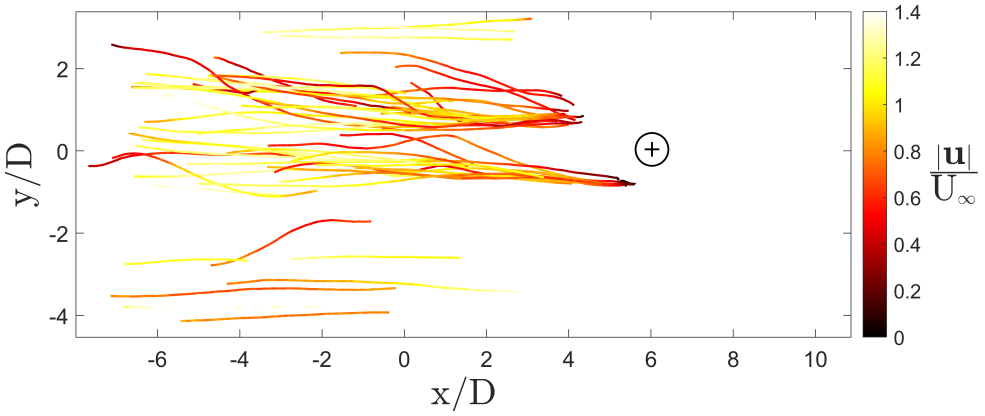

(a) $0 \leq t/\tau_f \leq 1$

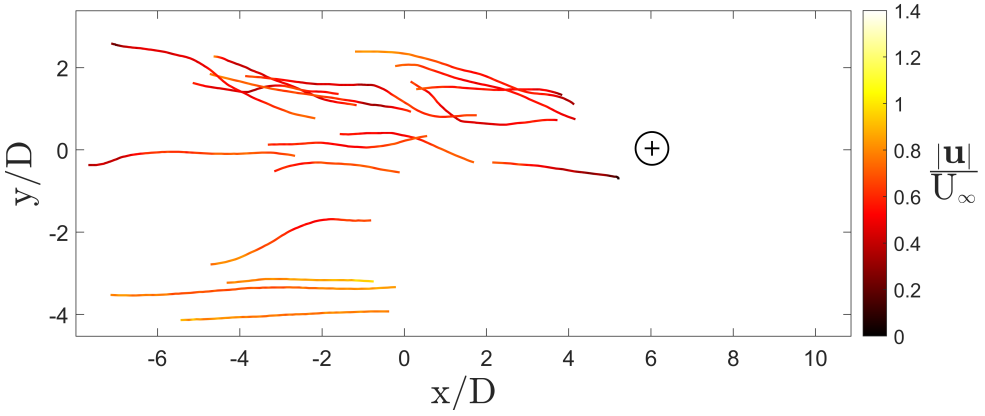

(b) $0 \leq t/\tau_f < 0.5$

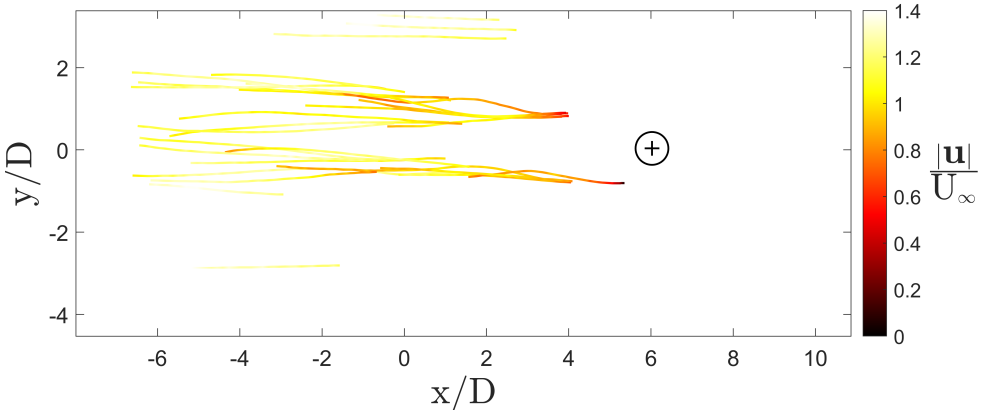

(c) $0.5 \leq t/\tau_f \leq 1$

Figure 3.21: Vortex trajectories in the streamwise-oscillating cylinder's wake corresponding to specified portion of forcing cycle. $Re_0 = 900$, $Re_q/Re_0 = 0.35$, $St_f/St_0 = 0.18$.

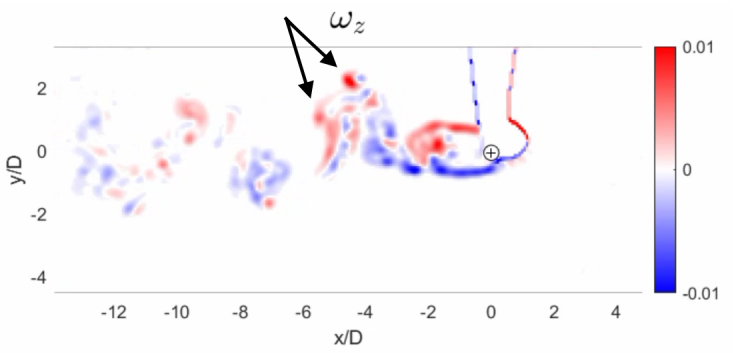

Figure 3.22: Secondary vortex generation in the oscillating cylinder wake. Arrows indicate secondary vortices.

ratio cylinder. Future work can consider the role of boundary layer destabilization in secondary vortex generation to develop a more robust characterization of the underlying mechanisms that gives rise to them.

Chapter 4

COMPLEXITY REDUCTION OF THE STREAMWISE OSCILLATING CYLINDER WAKE

Portions of this chapter will appear in the forthcoming publication:

Shamai, M., Dawson, S. T. M., Mezic, I., and McKeon, B. J. (2021). "Unsteady dynamics in the streamwise-oscillating cylinder wake for forcing frequencies below lock-on". In: *Physical Review Fluids*. DOI: 10.1103/PhysRevFluids.00.004700.

In Chapter 3 it was shown that streamwise forcing led to a range of unsteady flow phenomena in the oscillating cylinder's wake. It was observed, however, that during certain portions of the forcing cycle, the wake mimicked that of the stationary case. In this chapter it will be shown that the stationary and oscillating cases can indeed be related for the parameter range studied here. Specifically, analysis of the oscillating case through the lens of its stationary counterpart enables a deeper understanding of the system and also paves the way for reduced-order modeling. Thus, the time scaling framework presented in Chapter 2 will be used to transform the system such that it exhibits quasi-steady behavior. Further details regarding the formulation and implementation of the time-scaling framework can be found in Section 2.4.

4.1 Quasisteadiness

The quasisteadiness parameter, Ω, is considered first as it indicates portions of the forcing cycle corresponding to quasi-steady dynamics. Therefore, Ω can be used to determine the utility of quasi-steady time scaling for a particular forcing trajectory. The stationary shedding Strouhal number, St, is approximately constant with a value of $St \approx St_0 = 0.21$ across all of the instantaneous Reynolds numbers experienced during the forcing cycle (Fey et al., 1998). This quasi-steady assumption implies that the system dynamics are such that the fundamental mechanism of vortex shedding remains the same, subject only to an adjustment in frequency due to the change in the effective instantaneous Reynolds number. From the definition of Strouhal number, any change in freestream velocity, U, must be balanced by a variation of the shedding frequency, f, to maintain constant St. Therefore, assuming $St \approx St_0 =$ constant, the

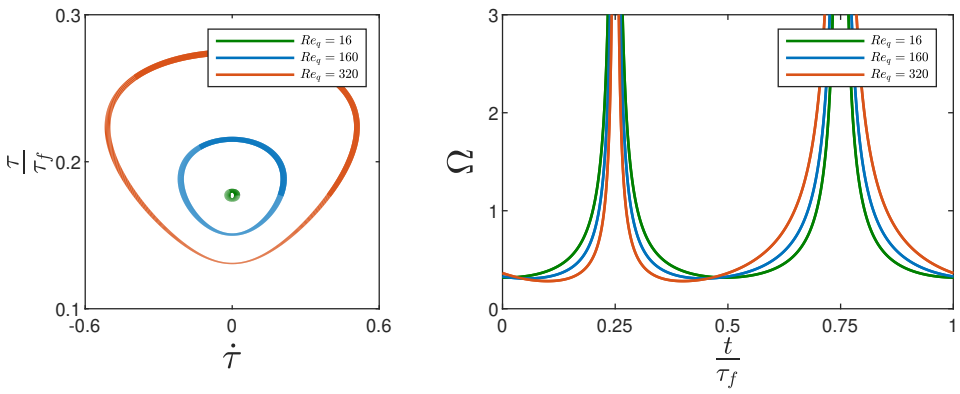

(a) (b)

Figure 4.1: (a) Phase portrait showing change in τ and $\dot{\tau}$ during forcing cycle. Line width is proportional to speed in phase-space. (b) Quasi-steadiness parameter plotted for streamwise forcing trajectory.

instantaneous shedding frequency can be expressed as

$$f(t) = \frac{St_0 U(t)}{D}, \tag{4.1}$$

or for the harmonic variation of cylinder velocity given in Eq. (2.1),

$$f(t) = \frac{St_0 \nu}{D^2}\Big(Re_0 - Re_q \sin(\omega_f t)\Big). \tag{4.2}$$

Since the dependence of frequency on time is known through Eq. (4.2), Ω can be computed a priori using Eq. (2.14) to give

$$\Omega = \left|\frac{\sec(\omega_f t)\big(Re_0 - Re_q \sin(\omega_f t)\big)^2}{\pi\big(Re_0^2 - Re_q^2\big)}\right|. \tag{4.3}$$

It was shown that the quasisteadiness incorporates both the characteristic period τ, as well as its rate of change, $\dot{\tau}$. Thus, consideration of the corresponding phase portrait (Fig. 4.1a) sheds light on behavior observed during various portions of the forcing cycle. Note that the line width in Fig. 4.1a represents the local speed in state-space. As Re_q increases, an asymmetry develops in the phase portrait which corresponds to the different wake states discussed in Section 3.2.1. The vertical extrema of the state-space trajectory allow sufficiently long residence time in states with approximately constant shedding frequencies and relatively simple vortex shedding. On the other hand, the steep regions of the trajectory on either side of $\dot{\tau} = 0$ indicate a rapid change in shedding frequency and thus do not allow consistent shedding to develop.

The time variation of Ω, shown in Fig. 4.1b, further elucidates the interplay between different states. As presented in Section 2.4.1, $\Omega \gg 1$ alludes to quasi-steady behavior. Therefore, the two peaks in Ω observed at $\frac{t}{\tau_f} = \frac{1}{4}$ and $\frac{t}{\tau_f} = \frac{3}{4}$ predict quasi-steady shedding where the assumption that $St \approx St_0$ holds. This was verified in Section 3.2.1 where it was shown that $\frac{t}{\tau_f} = \frac{1}{4}$ and $\frac{t}{\tau_f} = \frac{3}{4}$ indeed correspond to the two regions of the forcing cycle with the strongest vortex shedding. Similarly, the local minima in Ω, shown in Fig. 4.1b, indicate unsteady dynamics, also in agreement with experiments.

Beyond the presence of two peaks in Ω, Fig. 4.1b also displays an increase in asymmetry with Re_q. Whereas $\dot{f}$ governs the location of the peaks and is controlled by the cylinder acceleration, $\dot{\tau}$ also includes the instantaneous shedding frequency, which depends on the sense of the cylinder motion relative to the freestream, resulting in the observed asymmetry. This is an important distinction because the wider peak in Ω corresponds to the most active portion of the forcing trajectory where shedding is stronger. In this context, “stronger" refers to the duration of the quasi-steady portion, strength of shed vortices, number of completed shedding cycles, and relative magnitude of each spectral peak. Thus, not only does Ω give insight into quasi-steady regions of the forcing cycle, it also relates the relative strength of such regimes.

It is important to observe that the dimensional shedding frequency associated with the different quasi-steady regions may be different. This depends on the range of Reynolds numbers traversed during each portion of the forcing cycle. Using Eq. (4.2), the shedding frequency corresponding to each of the two peaks in Ω can be predicted. In Fig. 4.2, the observed spectral peaks for the interrogation point are compared with the predicted dominant Strouhal numbers corresponding to each peak in Ω. The peaks in the interrogation point spectra are in good agreement with the prediction, indicating that the two spectral peaks can be identified with periods of large Ω where the observed dominant frequencies arise due to quasi-steady shedding.

4.2 Quasi-Steady Time Scaling

The quasisteadiness indicates that streamwise forcing precipitates quasi-steady behavior during certain segments of the forcing cycle. Namely, the underlying mechanism producing flow structures during those regions is similar to the stationary case, although the characteristic frequency can vary. This motivates the use of the quasi-steady time scaling presented in Section 2.4.2 to normalize the time-varying

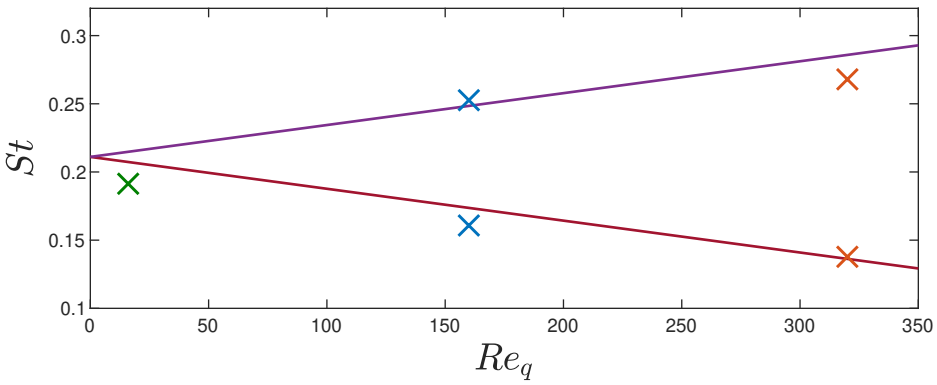

Figure 4.2: Comparison of predicted and observed dominant frequencies, $Re_0 = 900$, $St_f/St_0 = 0.18$. The solid lines represent the predicted dominant frequencies while the $\times$ symbols represent the actual dominant frequencies observed in experiments.

characteristic frequency. Similar to Ω, the dependence of f on forcing is known through Eq. (4.2), so $\tilde{t}$ can be computed a priori using Eq. (2.21) to give

$$\tilde{t} = t + \frac{Re_q}{Re_0 \omega_f}\left[\cos(\omega_f t) - 1\right]. \tag{4.4}$$

The scaled time, $\tilde{t}$, is shown in Fig. 4.3 for various forcing amplitudes. It can be seen that larger forcing amplitudes result in bigger deviations between the lab time, t, and scaled time, $\tilde{t}$. Similarly, the sampling rate used in experiments is shown relative to both t and $\tilde{t}$ in Fig. 4.4. Because the mapping between t and $\tilde{t}$, specifically Eq. (4.4), is known, the time-series are temporally interpolated, or "scaled," to replicate a constant sampling rate relative to $\tilde{t}$. Interpolated time-series will be referred to as "scaled" datasets in the remainder of this thesis.

4.3 Quasi-Steady Shedding Regimes

Whereas analysis of the unscaled system is difficult to interpret, time-scaling clarifies results and allows for a more meaningful interpretation. Figure 4.5 compares time traces of velocity at the interrogation point both before and after time scaling. Recalling the discussion in Section 3.2.1, vortex shedding in the oscillating cylinder's wake exhibited strong frequency modulation which was more observable in cases at lower forcing frequencies ($St_f \ll St_0$). After time scaling, however, the time traces show a striking difference: frequency modulation is no longer present but rather an approximately constant shedding frequency is observed. This is particularly evident in Fig. 4.6. Thus, the scaled system exhibits a quasi-steady shedding frequency, similar to the stationary case. The local power spectra confirm this observation. As

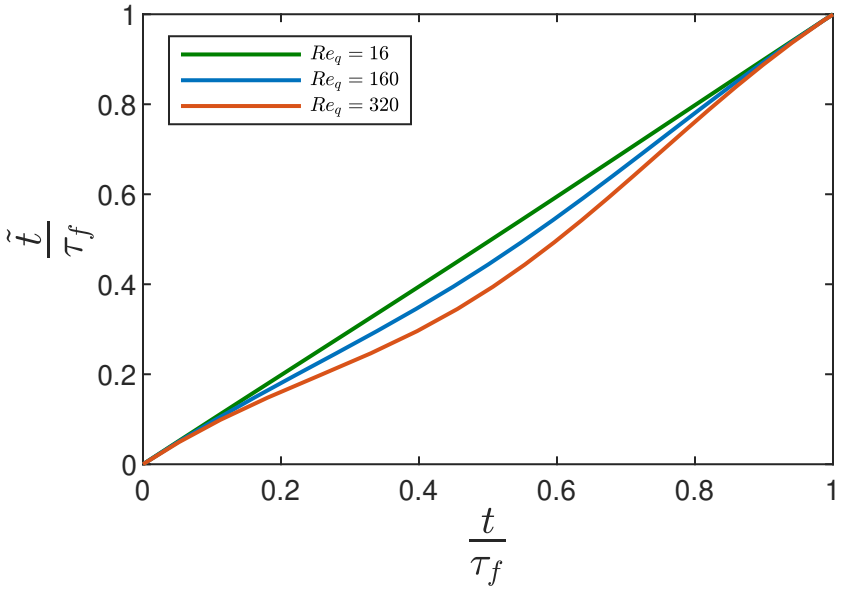

Figure 4.3: Variation in scaled time, $\tilde{t}$, with lab time, t.

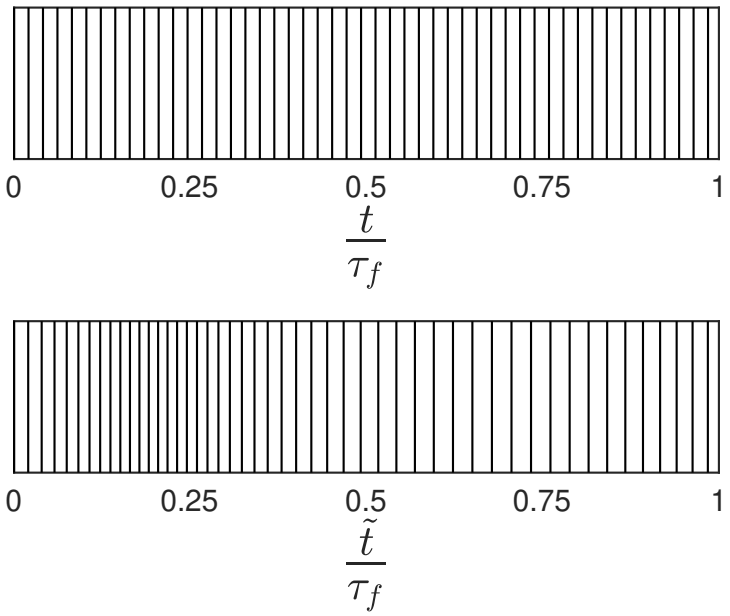

Figure 4.4: Experimental sampling rate in lab time (top) and corresponding scaled time (bottom). Vertical lines correspond to snapshot acquisition in the experiment. For the sake of clarity, the number of samples shown has been significantly decreased relative to the actual experiment.

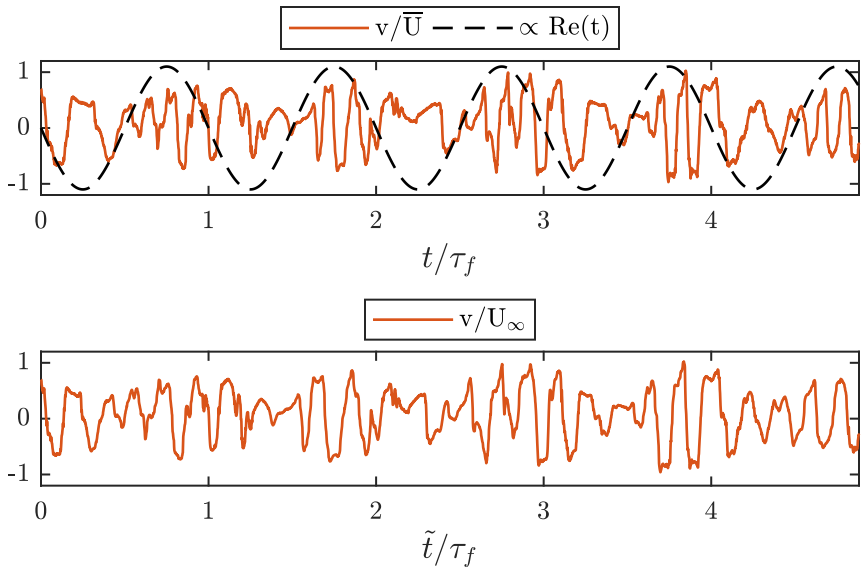

Figure 4.5: Time-trace of transverse velocity at interrogation point. $Re_0 = 900$, $Re_q/Re_0 = 0.35$, $St_f/St_0 = 0.18$.

seen in Fig. 4.7, quasi-steady time scaling leads to a reduction in spectral activity for the range of frequencies active in the unscaled system. Instead, time scaling leads to a collapse of spectral peaks near the stationary shedding frequency. This is in stark contrast to the spectra for unscaled cases (Fig. 3.9) which had local minima at the stationary shedding frequency.

A similar collapse is observed when time scaling is applied to the other forcing trajectories not explicitly discussed here. This collapse is shown in Fig. 4.8 for two additional forcing amplitudes. The lowest forcing amplitude, $Re_q = 16$, is considerably smaller than Re_0 and, as a result, the effective change in shedding frequency is only minor. Thus, the two dominant frequencies predicted in Fig. 4.2 for Re_q are nearly identical and only a single corresponding spectral peak was observed in experiments. It should also be noted that the spectra in Fig. 4.8 corresponding to $St_f \ll St_0$ contain relatively narrower peaks. This can likely be attributed to more pronounced frequency modulation resulting from a slower change in system dynamics, as describe above. Furthermore, the measurement of only a single forcing cycle in the experimental time series for these cases could also lead to a narrower peak.

From a global perspective, DMD of the scaled system also attests to reduced system complexity. Specifically, DMD of the scaled time series, seen in Figs. 4.9 and 4.10, shows that the two clusters of shedding modes present in the unscaled case have

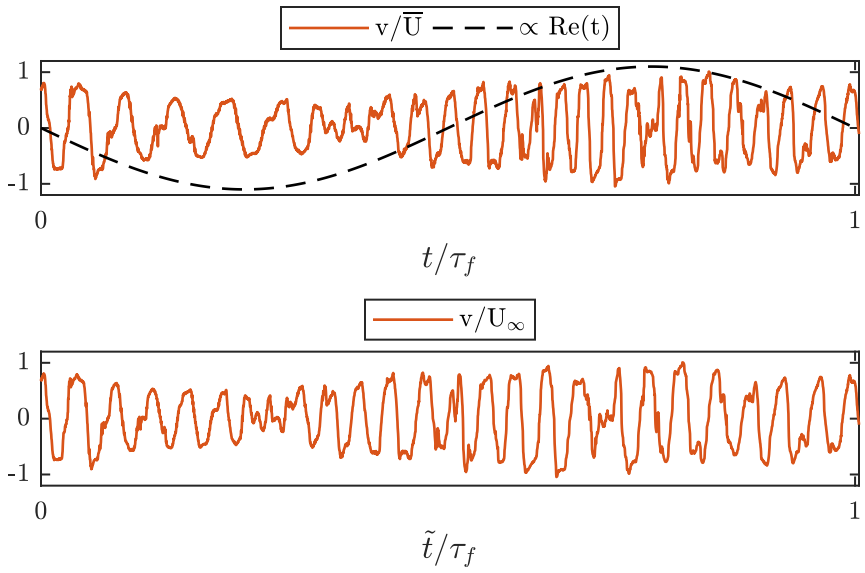

Figure 4.6: Time-trace of transverse velocity at interrogation point. $Re_0 = 900$, $Re_q/Re_0 = 0.35$, $St_f/St_0 = 0.036$.

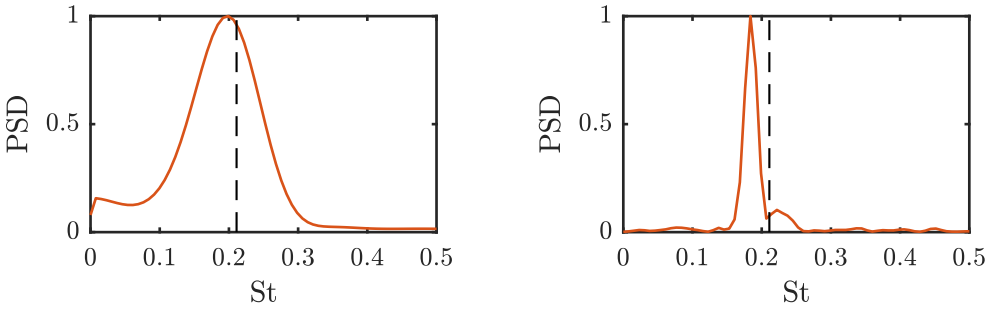

Figure 4.7: Interrogation point spectra for scaled system. (a) $Re_q/Re_0 = 0.35$, $St_f/St_0 = 0.18$, (b) $Re_q/Re_0 = 0.35$, $St_f/St_0 = 0.036$. $Re_0 = 900$.

been replaced by a cluster of shedding modes around the stationary shedding frequency. Relative to the unscaled system, scaling also leads to extraction of fewer shedding modes, each of which contains less noise and contamination from other structures in the flow. Furthermore, the shedding modes generate a clear spectral peak reminiscent of the stationary case.

To summarize, quasi-steady time scaling transforms the system such that spectral activity due to vortex shedding is limited to a small band of frequencies near the stationary value. The shedding frequency no longer displays strong frequency modulation (i.e. two spectral peaks) and instead exhibits quasi-steady behavior reminiscent of the stationary cylinder. The extraction of fewer DMD shedding

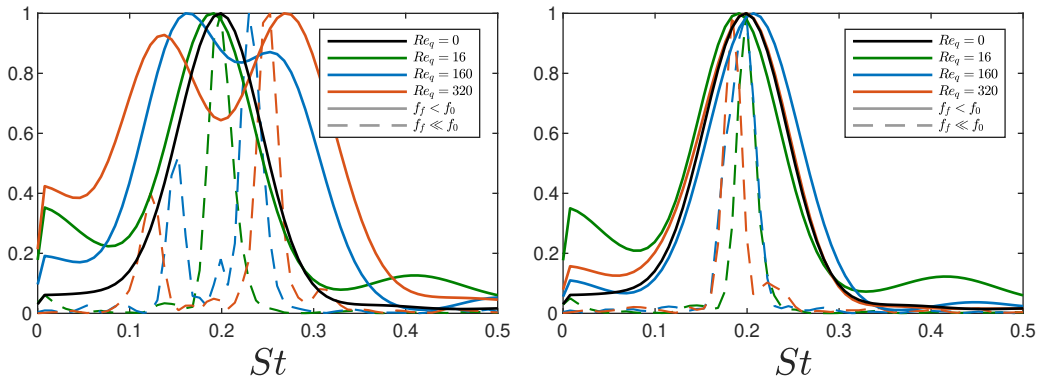

Figure 4.8: Comparison of interrogation point power spectra before (left) and after (right) application of quasi-steady time scaling.

modes also attests to this fact.

4.4 Reduced-Order Flow Reconstruction

The lack of a clear spectral peak and broad distribution of shedding modes in DMD of the unscaled system hinders reconstruction. In particular, the choice of modes required for a reduced-order model is not clear. The complexity reduction achieved via quasi-steady time scaling, however, remedies this issue. Specifically, the concise spectral representation of system dynamics achieved via time scaling allows for robust characterization and grouping of dynamically significant modes.

Revisiting Eq. (2.10), it can be seen that any subset of DMD modes can be used to produce a reduced-order model of the flow. For the reconstruction to hold meaning, however, the choice of modes must correspond to dynamically significant flow structures. In the previous section it was shown that time scaling enabled the identification of three DMD modes, corresponding to the mean, forcing, and shedding, respectively. Therefore, a simple reduced-order model can be generated using these three DMD modes. Specifically, the mean, forcing, and peak shedding mode of the scaled system can be combined with Eq. (2.10) to produce a simple yet meaningful model of the flow. The projection coefficient, α_j, used to scale each mode in Eq. (2.10) is taken as the projection coefficient of the first snapshot onto the DMD modes. After reconstruction, the model is transformed back to lab time, t, as the mapping between $\tilde{t}$ and t is known through Eq. (2.21).

Snapshots of the reduced-order flow reconstruction are shown in Figs. 4.11 and 4.13. The alternating vertical structures indicate that the flow reconstruction exhibits vortex shedding reminiscent of the full system. Furthermore, the time trace of

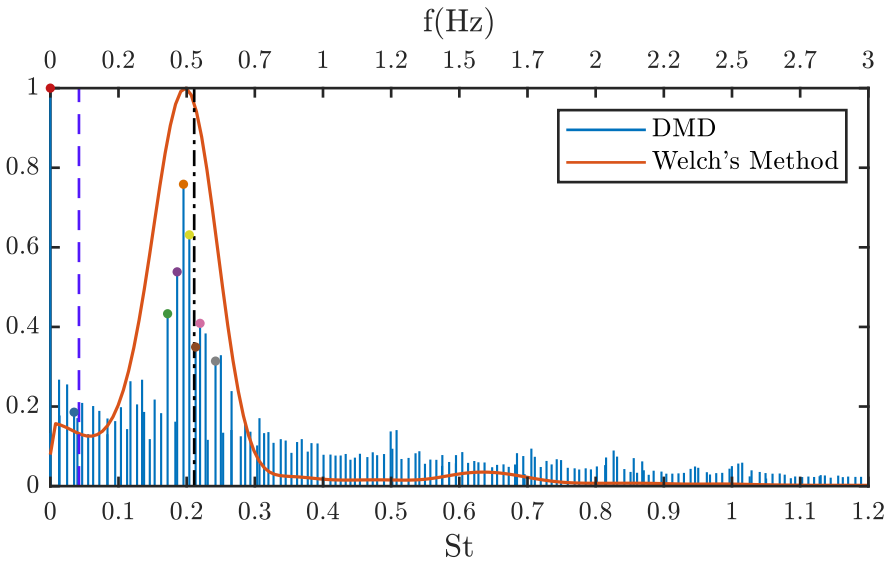

(a)

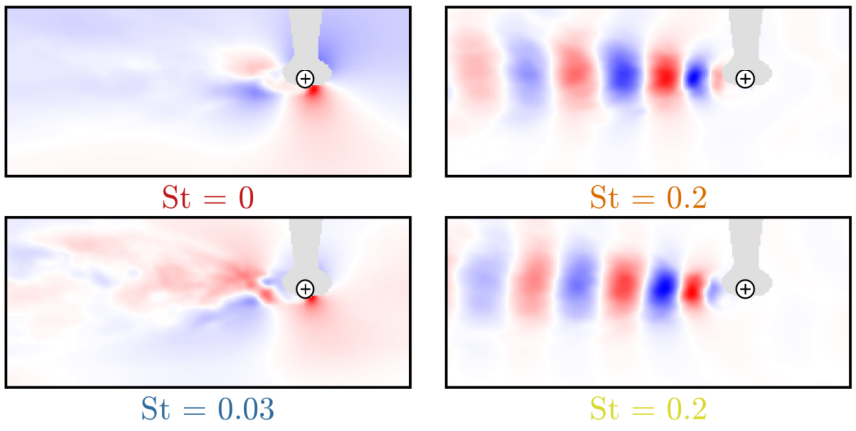

(b)

Figure 4.9: DMD spectrum (a) and modes (b) for oscillating cylinder with quasi-steady time scaling, $Re_0 = 900$, $Re_q/Re_0 = 0.35$, $St_f/St_0 = 0.18$.

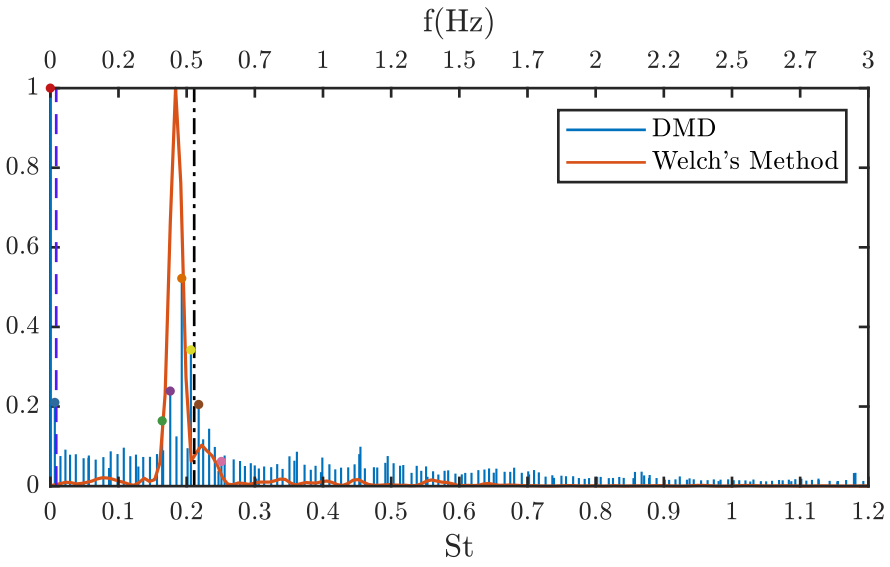

(a)

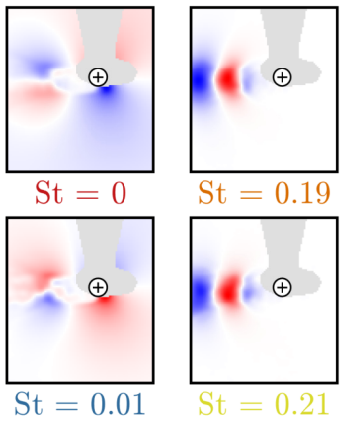

(b)

Figure 4.10: DMD spectrum (a) and modes (b) for oscillating cylinder with quasi-steady time scaling, $Re_0 = 900$, $Re_q/Re_0 = 0.35$, $St_f/St_0 = 0.036$.

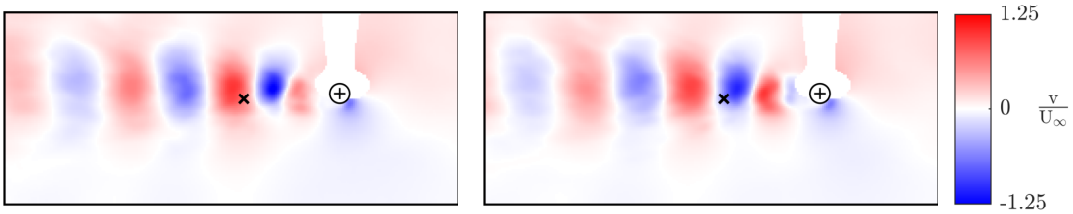

(a) $t/\tau_f = 0.25$ (b) $t/\tau_f = 0.75$

Figure 4.11: Instantaneous snapshot reduced-order flow reconstruction in lab time, t. The location of the interrogation point is denoted by ×. $Re_0 = 900$, $Re_q/Re_0 = 0.35$, $St_f/St_0 = 0.18$.

reconstructed velocity at the interrogation point, shown in Figs. 4.12 and 4.14, highlight the development of frequency modulation.

It should be noted that although the reduced-order model displays frequency modulation similar to the full system, the same does not hold true for amplitude modulation. This is not surprising given that time scaling is primarily concerned with the shedding frequency. Additional factors contributing to discrepancies will be discussed in Section 4.5. That is not to say that the reconstruction does not hold value, however. Such a model can be used in future applications to predict and control unsteady fluid-structure phenomena associated with the frequency-modulated shedding. More importantly, however, the model shows that the quasi-steady assumption relating the stationary and oscillating systems enables the generation of a physically meaningful model.

It is reiterated that quasi-steady time scaling links the dynamics of the scaled and stationary systems. After time scaling, the dynamics of the forced system resembles that of the stationary system, as confirmed using DMD. This observation implies that the oscillating case can be modeled in scaled time using the stationary system's Dynamic Mode Decomposition. After reconstruction using the *stationary* cylinder's decomposition, the system can be transformed to lab time using Eq. (4.4) to provide a reduced-order model of the *oscillating* system. It should be noted that the stationary system has no corresponding forcing mode, therefore this approach would primarily model vortex shedding. Such an approach is not limited to the oscillating cylinder. If conditions permitting the use of time scaling are satisfied, it is likely that this approach could be used to model the dynamics of other forced fluid structures systems solely using information of their stationary counterparts.

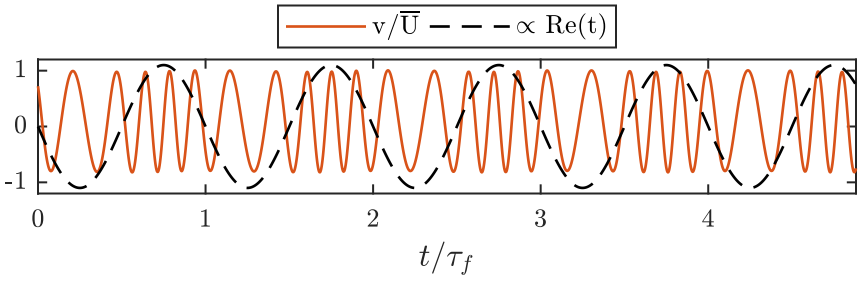

Figure 4.12: Time trace of reconstructed velocity measured at interrogation point. $Re_0 = 900$, $Re_q/Re_0 = 0.35$, $St_f/St_0 = 0.18$.

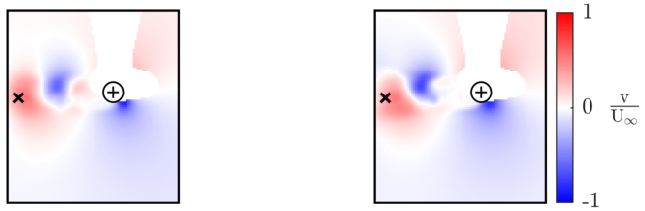

(a) $t/\tau_f = 0.25$ (b) $t/\tau_f = 0.75$

Figure 4.13: Instantaneous snapshot reduced-order flow reconstruction in lab time, t. The location of the interrogation point is denoted by ×. $Re_0 = 900$, $Re_q/Re_0 = 0.35$, $St_f/St_0 = 0.036$.

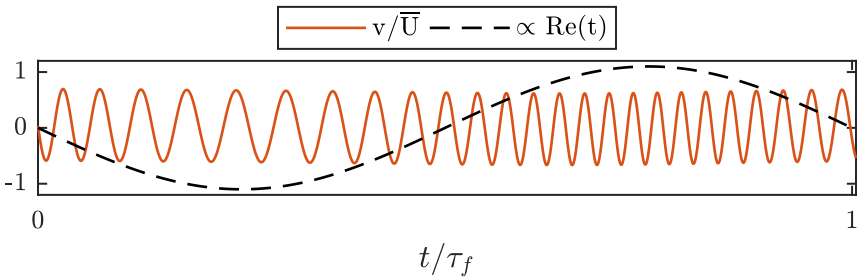

Figure 4.14: Time trace of reconstructed velocity measured at interrogation point. $Re_0 = 900$, $Re_q/Re_0 = 0.35$, $St_f/St_0 = 0.036$.

4.5 Limitations of Time Scaling

While it was shown that the complexity of this flow can be reduced by quasi-steady time scaling, several limitations must be addressed. In particular, the success time scaling hinges the relation derived for the time-varying characteristic (shedding) frequency of the system. In order to develop such an equation, a quasi-steady assumption is used to derive a simple relation for the shedding frequency (Eq. (4.2)). Although this formulation satisfactorily predicts the system's dominant shedding frequencies and time scaling considerably reduces system complexity, several factors may be underlying any discrepancies. First, the spectra were calculated using Welch's method, which depends heavily on window quantity and size. Varying these parameters can lead to different estimates of the PSD. Thus, these parameters may cause the interrogation point spectra to deviate from the prediction. This is particularly relevant when $St_f \ll St_0$, resulting in PIV time series that only contain a single forcing cycle.

It is also assumed that St_0 remains constant for the range of Reynolds numbers encountered, yet, in reality, it can vary by up to 3% during the forcing cycle, a deviation which may percolate through the analysis. It should also be noted that time scaling is applied uniformly to each snapshot in the time series. That is, the scaling procedure does not account for the fact that it takes a finite amount of time for vortical structures to convect downstream. Even still, quasi-steady time scaling gives reasonable collapse of the spectral peaks.

Additionally, the scaling procedure does not account for vortex interactions, shear-layer dynamics, and the resulting starting vortices. Similarly, the modulation of shear-layer strength is such that starting vortices may develop at times close to peaks in Ω, where shedding at the dominant frequencies is expected. As a result, the inclusion of additional DMD modes in the flow reconstruction could be needed to capture these phenomena and the resulting amplitude modulation.

A comment should also be made regarding the range of streamwise forcing trajectories where time scaling may be useful. Given that the analysis focused on vortex shedding in regimes analogous to the stationary system, the absence of such behavior would limit the utility of scaling time. As a result, an important threshold would be the transition to the lock-on state near $St_f/St_0 \sim 1$. Similarly, forcing at amplitudes that do not permit the development of vortex shedding would also limit the use of time scaling. An extreme example of this would be a forcing trajectory where the relative velocity seen by the cylinder changes direction and the wake

moves to the opposite side of the cylinder. Future work can consider time scaling applied to separate segments of such forcing cycles to reduce complexity.

Chapter 5

COMPLEXITY REDUCTION OF THE FLOW AROUND A HEMISPHERE IN PULSATILE FLOW

The flow around surface-mounted hemispheres has received considerable attention due to the development of multiple important flow phenomena. Of particular significance are the hairpin vortices that are shed periodically and hold importance due to their similarity with hairpin vortices observed in turbulent boundary layers (Acarlar and Smith, 1987). Although the majority of previous studies consider a steady freestream, recent interest has developed in the case of a pulsatile freestream due to similarities between the flowfield and human vocal fold pathologies (Carr, 2019; Carr et al., 2020). Furthermore, Carr (2019) and Carr et al. (2020) have shown that highly pulsatile forcing leads to the development of additional structures beyond those observed in the unforced case. In this chapter, the flowfield[1] around a surface-mounted hemisphere subject to a highly pulsatile freestream will be analyzed. For additional details regarding the experimental facility used to acquire flowfields, measurement diagnostics, and forcing cycles, readers can refer to Sections 2.1.3, 2.1.4 and 2.2.1, respectively. Quasi-steady time scaling will be used to reduce system complexity and show that for particular forcing regimes, flow structures can be related back to the analogous unforced system (i.e., subject to a steady freestream). As a precursor to the analysis of the pulsatile case, relevant flow structures and dynamics for the corresponding unforced system are summarized first.

5.1 Flow Structures in the Absence of Pulsatility

A primary flow structure of importance in this system is the standing horseshoe (or necklace) vortex that develops upstream of the hemisphere (Acarlar and Smith, 1987). A schematic of the standing vortex is shown in Fig. 5.1a. It should be noted that horseshoe vortices are ubiquitous in junction flows beyond the case of a surface-mounted hemisphere (Simpson, 2001). Furthermore, such systems are not limited to the development of a single vortex and often see the generation of multiple standing vortices resulting in a system of horseshoe vortices (Simpson, 2001). The

[1]Surface-mounted hemisphere experiments were carried out by Ian A. Carr and Michael W. Plesniak. We are extremely grateful to them for sharing the data as well as invaluable discussions, insight, and collaboration.

horseshoe vortex plays an important role redistributing fluid away from the body towards the wake via the induced velocity field. This can result in the generation of secondary flow structures and additional instabilities in the wake.

The primary flow structure considered in this chapter will be the canonical hairpin vortices. These structures, characterized by their curved, two-legged geometry (shown in Fig. 5.1), are periodically shed from the cylinder for Reynolds numbers ranging from $Re_R \approx 120$ through $Re_R \approx 12000$ (Acarlar and Smith, 1987; Tamai et al., 1987). Although hairpin vortices result from the shedding of arched vortex tubes located at the separation line of the hemisphere, the velocity gradient (and corresponding shear) away from the wall results in the downstream slant and stretching of hairpins as they convect away from the hemisphere (Tamai et al., 1987). Often, the leading edge of each leg can interact with the hairpin located directly upstream. As a result, the leading portion of each leg is slightly lifted up and away from the wall. The characteristic shedding frequency of the hemisphere corresponds to the generation and shedding of hairpin vortices. Beyond $Re_R \approx 2000$, Tamai et al. (1987) note that multiple hairpins can coalesce into a single structure, resulting in a hairpin shedding frequency that varies from the frequency at which individual hairpins are generated at the hemisphere. This is important to note because the pulsatile forcing cycle considered here, corresponding to $0 \leq Re_R \leq 2000$, approaches this threshold. Previous studies also show that in this range of Reynolds numbers, the shedding Strouhal number increases with Reynolds number (see Fig. 5.2).

Beyond the development of the horseshoe and hairpin vortices, this system can also see the generation of secondary flow structures. Examples include the production of secondary hairpin vortices in the wake on either side of the hemisphere due to the interaction of the high momentum outer flow with the low speed flow lifted up from the wall by the horseshoe vortex (Acarlar and Smith, 1987). Similarly, secondary vortices can also develop between the legs of each hairpin vortex (Acarlar and Smith, 1987). Although such secondary flow structures can be generated, they will not be considered here in depth.

5.2 Analysis of the Hemisphere Wake with Pulsatile Forcing

Detailed characterization of the complex and highly three-dimensional flowfield around a hemisphere subject to highly pulsatile forcing can be found in Carr and Plesniak (2016), Carr (2019), and Carr et al. (2020). A brief summary of the relevant flow structures will be provided, however, to facilitate subsequent analysis. In

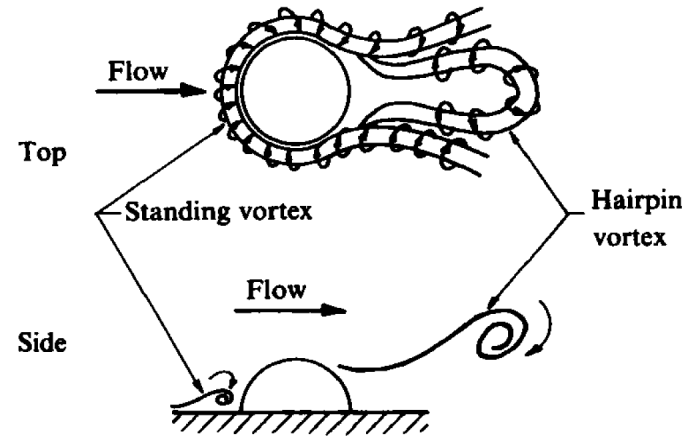

(a)

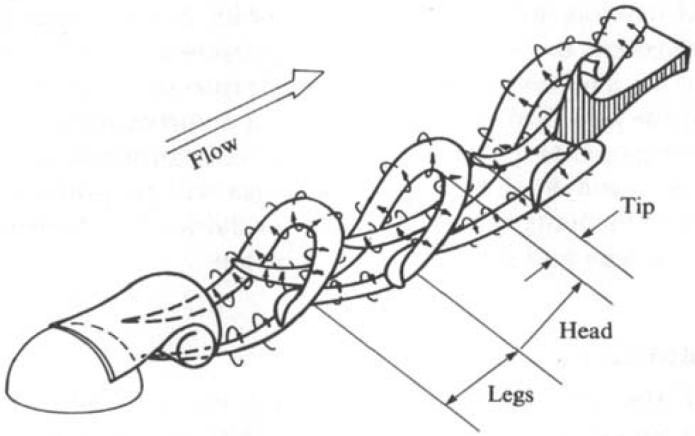

(b)

Figure 5.1: Flow structures in the wake of a surface-mounted hemisphere. From Acarlar and Smith (1987).

particular, system dynamics can range from periodic hairpin shedding, to unsteady, phase-locked shedding of a single arch vortex during each forcing cycle. The experimental flowfields discussed here all correspond to nominal values $\overline{Re_R} = 1000$, $Re_\Delta/\overline{Re_R} = 1$, as reported by Carr (2019), and were acquired using the BPWT facility outlined in Section 2.1.3. Results will be presented for two pulsatile forcing frequencies, namely, $St_f = 0.01$ and $St_f = 0.1$, corresponding to $St_f/St_0 = 0.05$ and $St_f/St_0 = 0.5$, respectively.

5.2.1 Hairpin Shedding Regime

The pulsatile forcing profile corresponding to experiments at $St_f/St_0 = 0.05$ is shown in Fig. 5.3. It should be noted that although the experimental forcing profile is not perfectly sinusoidal, the observed wake dynamics still resemble those syn-

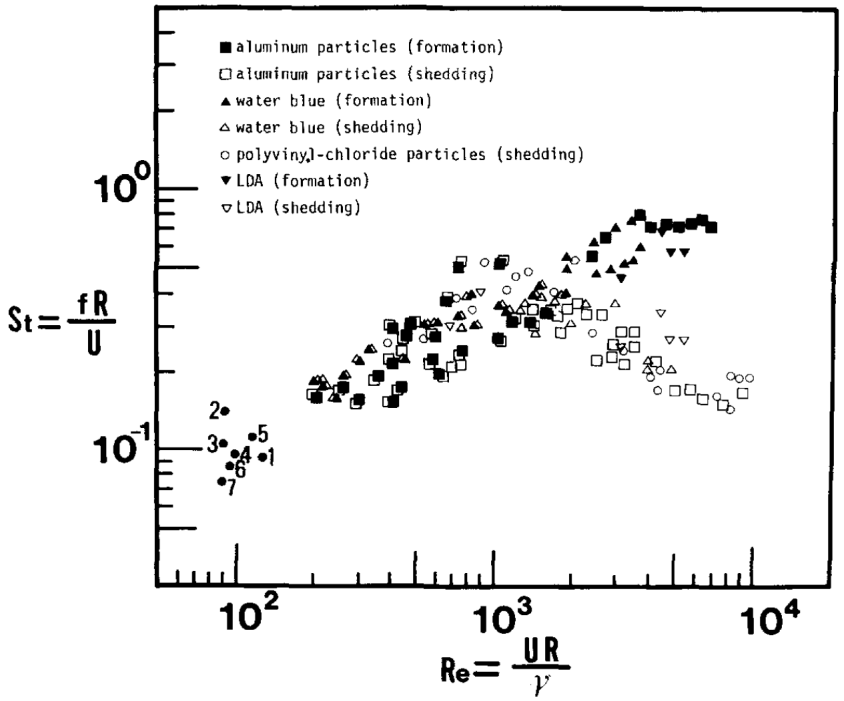

Figure 5.2: Hairpin generation and shedding frequency for a surface-mounted hemisphere subject to a steady freestream. From Tamai et al. (1987).

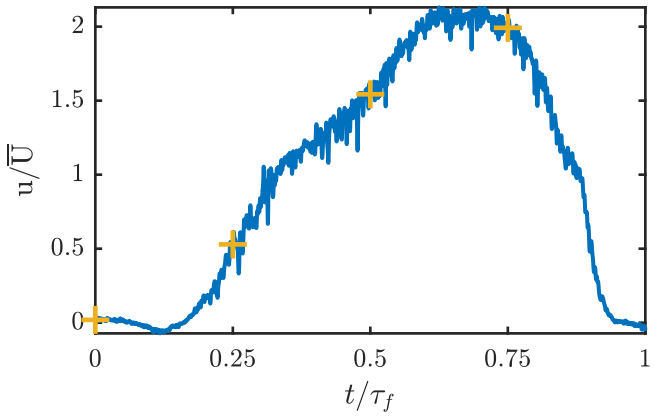

Figure 5.3: Pulsatile forcing cycle for $St_f/St_0 = 0.05$ measured at interrogation pointed located approximately $2R$ upstream of cylinder and $3R$ away from the wall (furthest upstream point in PIV domain). The + symbols correspond to the snapshots shown in Fig. 5.4.

onymous with ideal sinusoidal forcing (Carr et al., 2020). Snapshots of the system at various phases in the forcing cycle are presented in Fig. 5.4. As the freestream velocity increases from its minimum value at $t/\tau_f = 0$, the flow separates from the hemisphere, generating a recirculation bubble and consequent rear arch vortex at the separation line, seen in the second column of Fig. 5.4. As the freestream velocity continues to increase, it reaches a value sufficient to drag the head of the rear arch vortex downstream, resulting in periodic shedding of hairpin vortices, seen in the third and fourth columns of Fig. 5.4, similar to the steady freestream case. As the flow decelerates, the freestream velocity eventually decreases below the value required to drag the rear arch vortices downstream, and thus hairpin shedding terminates. As the freestream velocity approaches its minimum value, the velocity induced by the rear arch vortex eventually exceeds the instantaneous freestream velocity, resulting in upstream motion of the rear arch vortex. In addition to the wake dynamics outlined above, the pulsatile forcing cycle also leads to the generation of a horseshoe vortex upstream of the hemisphere. The resulting horseshoe vortex can be seen as the small pocket of vorticity located just upstream of the hemisphere in the latter two columns of Fig. 5.4. It was observed that the distance between the horseshoe vortex and hemisphere decreases as the instantaneous freestream velocity increases and vice-versa.

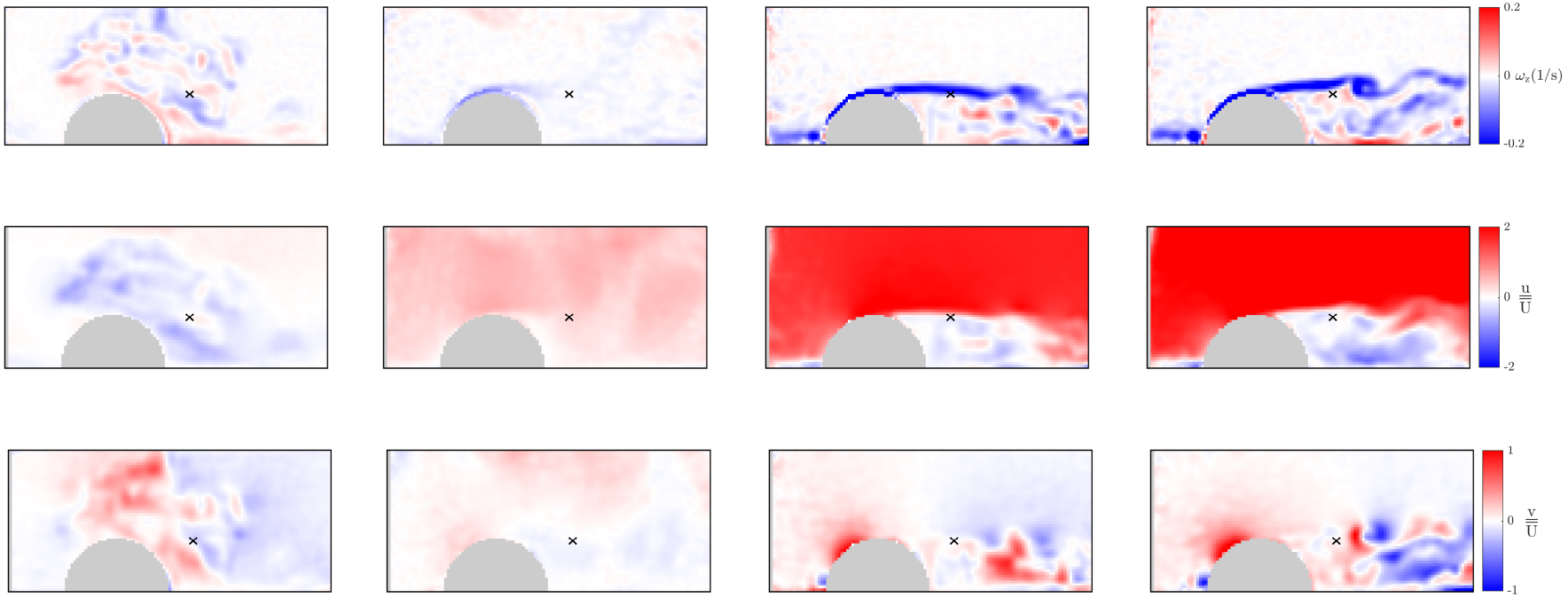

Figure 5.4: Flow around a hemisphere in pulsatile flow, $\overline{Re_R} = 1000$, $Re_q/\overline{Re_R} = 1$, $St_f/St_0 = 0.05$. The top row corresponds to vorticity ω_z. The second and third rows correspond to the streamwise and wall-normal components of velocity, $u/\overline{U}$ and $v/\overline{U}$, respectively. From left to right, the columns correspond to $t/\tau_f = 0, 0.25, 0.50$, and 0.75, respectively. The $\times$ symbol represents the location of the interrogation point. Flow is from left to right.

The time trace of velocity at an interrogation point located $1.5R$ downstream of hemisphere and $1R$ above the wall is shown in Fig. 5.5. For ease of comparison, the instantaneous freestream velocity corresponding to the time trace is also shown in Fig. 5.5. The time trace at the interrogation point, situated in the wake's shear layer, alludes to the aforementioned wake dynamics. Specifically, the high-frequency oscillations that develop in the time trace as the freestream velocity increases indicate the shedding of hairpin vortices. It can also be seen that the frequency of wall-normal velocity oscillations during this portion of the forcing cycle do not remain constant but rather vary, alluding to frequency-modulated shedding. On the other hand, the relatively flat portion of the time trace near the minimum freestream velocity corresponds to the absence of shedding in the wake due to upstream motion of the rear arch vortex. Beyond flow structures in the close vicinity of the hemisphere, the presence of the wall merits discussion of the boundary layer. Carr et al. (2020) used flowfields from an analogous Direct Numerical Simulation (DNS) to characterize the boundary layer on the plane of symmetry three diameters upstream of the hemisphere. For both forcing frequencies considered here, they showed that the boundary layer height was on the order of the hemisphere's radius. Furthermore, Carr et al. (2020) observed the development of near-wall reversal at the minimum freestream velocity. Their results showed that near-wall reversal was small when $St_f \ll St_0$ but increased noticeably when St_f and St_0 were of the same order. As the freestream velocity increased, they observed a reduction in near-wall reversal. Finally, when the freestream velocity reached its maximum value, Carr et al. (2020) found that the boundary layer profiles for both forcing frequencies resembled the Blausius profile.

5.2.2 Phase-Locked Regime

Forcing frequency ratios of order $St_f/St_0 \sim 10^{-1}$ lead to phase-locked wake dynamics, in contrast to the hairpin shedding regime outlined above. Figure 5.6 shows snapshots of the system at multiple phases in the forcing cycle for $St_f/St_0 = 0.5$. As with the previous case, the pulsatile forcing profile, shown in Fig. 5.7, deviates from an ideal sinusoid, but the observed flow phenomena hold for the analogous system with ideal sinusoidal forcing. Snapshots shown in Fig. 5.6 highlight the phase-locked rear arch vortex that develops for this forcing regime. Whereas the large separation of scales between the forcing and shedding frequency in the previous case permitted enough time to shed multiple hairpin vortices, the phase-locked case instead sees the generation of a single rear arch vortex during each forcing cycle.

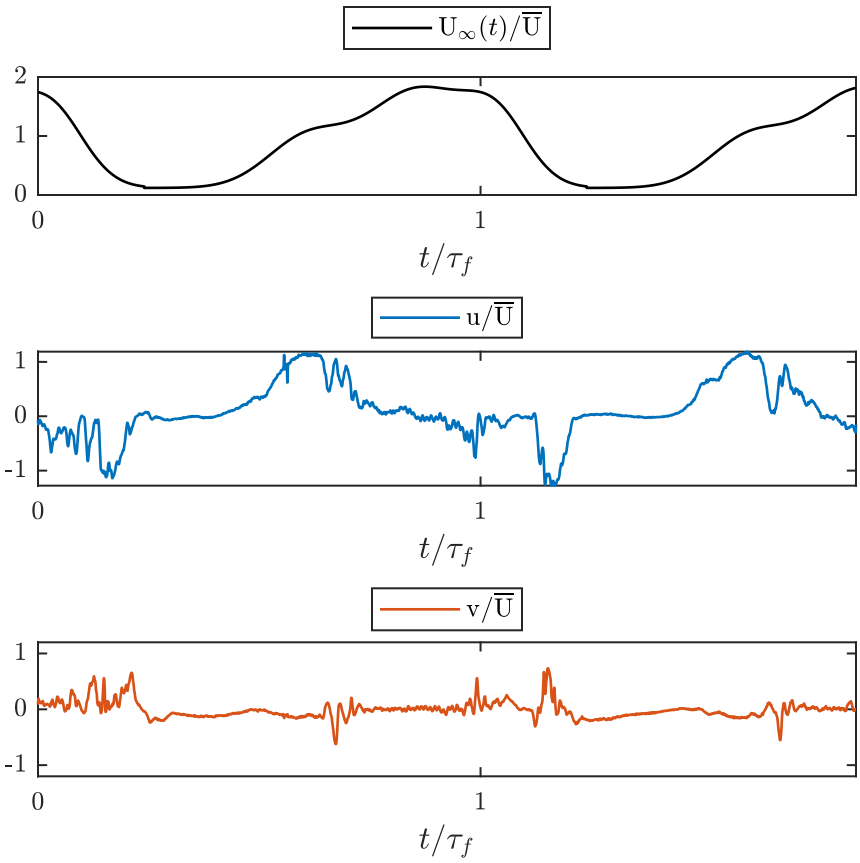

Figure 5.5: Trace of instantaneous freestream and velocity measured at interrogation point, $St_f/St_0 = 0.05$.

Specifically, as the instantaneous freestream velocity increases, a rear arch vortex grows behind the hemisphere. As the freestream velocity decreases, the velocity induced by the rear arch vortex eventually supersedes the instantaneous freestream, resulting in the forward motion of the rear arch vortex. The time traces of velocity in the wake, shown in Fig. 5.8, also attest to the phase-locked nature of the wake in this forcing regime. In particular, the time trace of velocity in the wake shows strong fluctuations at the forcing frequency. Furthermore, the time trace is devoid of the high-frequency fluctuations seen in the aforementioned regime, further verifying the absence of periodic hairpin shedding.

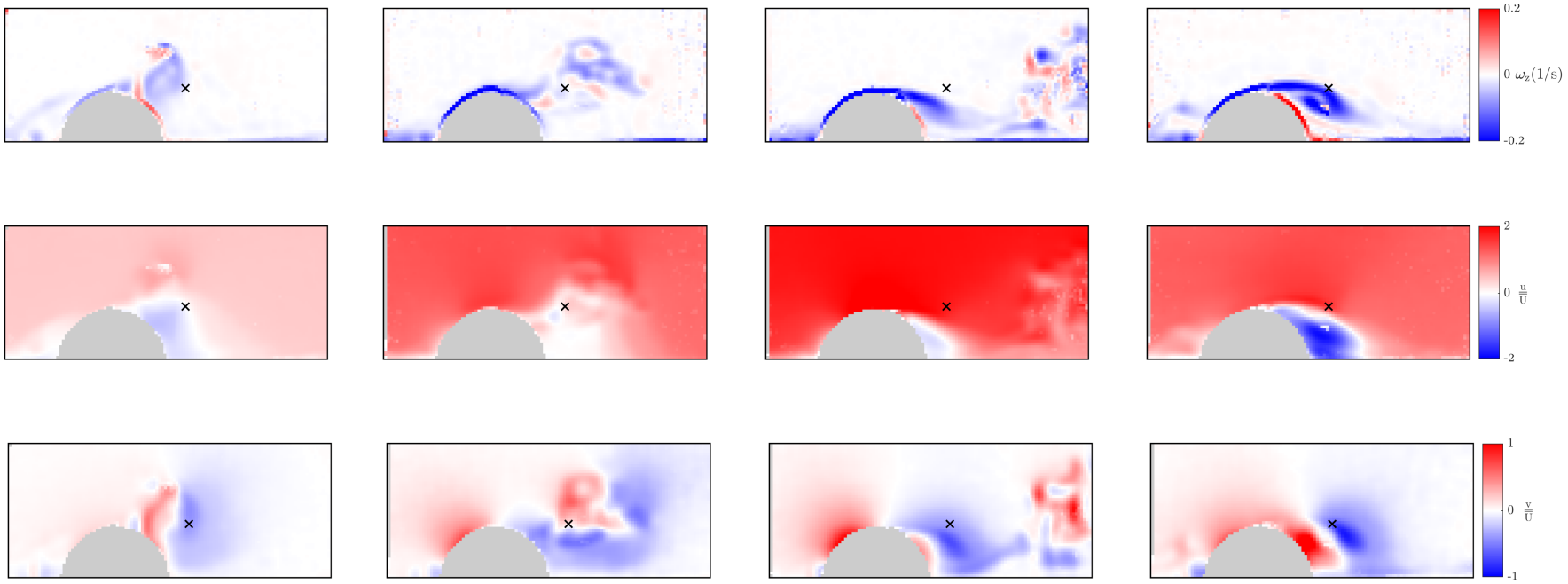

Figure 5.6: Flow around a hemisphere in pulsatile flow, $\overline{Re_R} = 1000$, $Re_q/\overline{Re_R} = 1$, $St_f/St_0 = 0.5$. The top row corresponds to vorticity ω_z. The second and third rows correspond to the streamwise and wall-normal components of velocity, $u/\overline{U}$ and $v/\overline{U}$, respectively. From left to right, the columns correspond to $t/\tau_f = 0, 0.25, 0.50$, and 0.75, respectively. The $\times$ symbol represents the location of the interrogation point. Flow is from left to right.

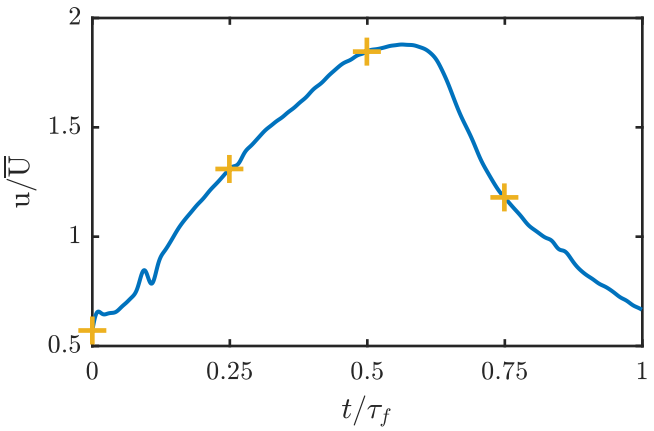

Figure 5.7: Pulsatile forcing cycle for $St_f/St_0 = 0.5$. The + symbols correspond to the snapshots shown in Fig. 5.6.

5.2.3 Dynamic Mode Decomposition

In order to analyze the aforementioned spatio-temporal dynamics in the flowfield, Dynamic Mode Decomposition of wall-normal velocity fields was considered. DMD of the wall-normal velocity fields corresponding to $St_f/St_0 = 0.05$ is shown in Fig. 5.9. The DMD spectrum, shown in Fig. 5.9a, displays a strong peak only at the mean and forcing frequencies. Similar to frequency-modulated vortex shedding in the wake of an oscillating cylinder, DMD extracts an array of spatially similar shedding modes, as seen in seen in Fig. 5.9. Comparison with the instantaneous snapshots of wall-normal velocity shown in Fig. 5.4 indicates that the shedding modes extracted using DMD indeed correspond to hairpin vortices shed by the hemisphere. The distribution of shedding modes over a wide range of frequencies alludes to frequency-modulated shedding, also observed in the frequency-modulated time trace of velocity (Fig. 5.5). Beyond the extraction of modes representing hairpin vortices, the forcing mode also captures the horseshoe vortex located upstream of the cylinder. It is reiterated that the distance between the hemisphere and horseshoe vortex oscillates inversely with the freestream velocity. Thus, the structure upstream of the hemisphere in the forcing mode captures the streamwise oscillation of the horseshoe vortex.

DMD of the flowfields corresponding to $St_f/St_0 = 0.5$, shown in Fig. 5.10, results in a strong peak at the forcing frequency. The corresponding DMD mode, shown in Fig. 5.10b, contains a vertical structure in the same location as the rear arch vortex shown in Fig. 5.6. An additional mode, corresponding to the second-highest spectral peak after the forcing mode, is also shown in Fig. 5.10b. This mode,

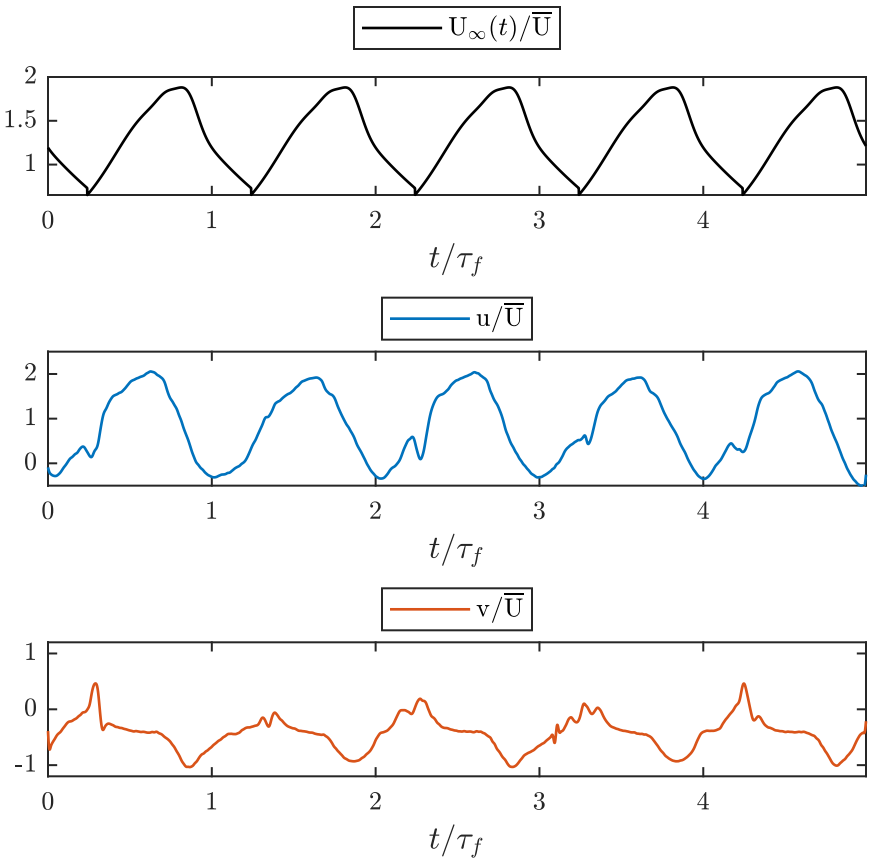

Figure 5.8: Trace of instantaneous freestream and velocity measured at interrogation point, $St_f/St_0 = 0.5$.

corresponding to twice the forcing frequency, is likely a harmonic of the forcing mode. Therefore, the dominant modes in the decomposition (beyond the mean mode) are all extractions of flow structures phase-locked to the forcing. Thus, the initial characterization of this flow regime as being phase-locked to the forcing is also confirmed via DMD.

5.3 Complexity Reduction via Time Scaling

In this section, the quasi-steady time scaling framework presented in Section 2.4 will be used to reduce complexity of the hemisphere wake corresponding to $St_f/St_0 = 0.05$. Although a range of flow structures develop in the flow, time scaling will be used to reduce complexity associated with hairpin shedding during the forcing cycle. It will be shown that the hemisphere exhibits shedding dynamics analogous to the stationary case motivating time scaling to transform the forced system to exhibit quasi-steady shedding similar to the non-pulsatile case.

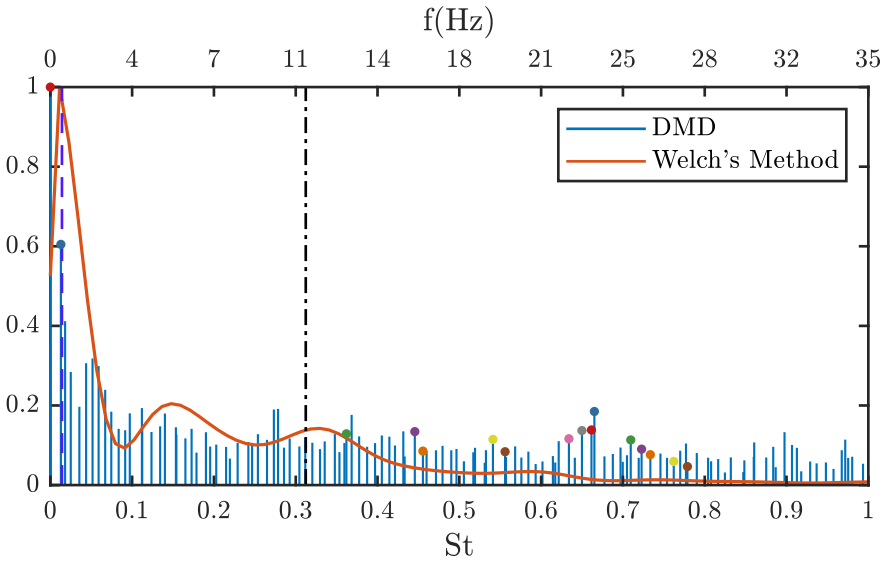

(a)

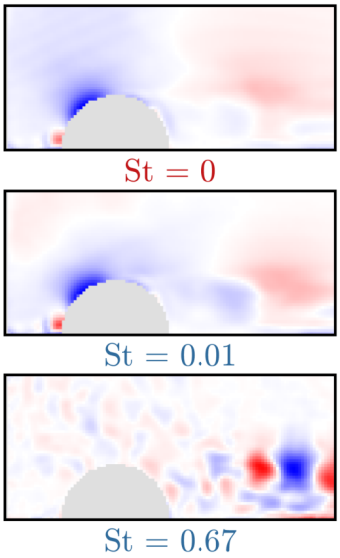

(b)

Figure 5.9: DMD spectrum (a) and modes (b) for the hemisphere in pulsatile flow for $St_f/St_0 = 0.05$. With the exception of the mean mode and forcing modes ($St = 0$ and $St = 0.01$), the colored circles on the spectrum represent shedding modes. The colored labels in (b) correspond to the circles of the same color on the spectrum. The black dot-dashed line represents the stationary shedding frequency while the purple dashed line denotes the forcing frequency.

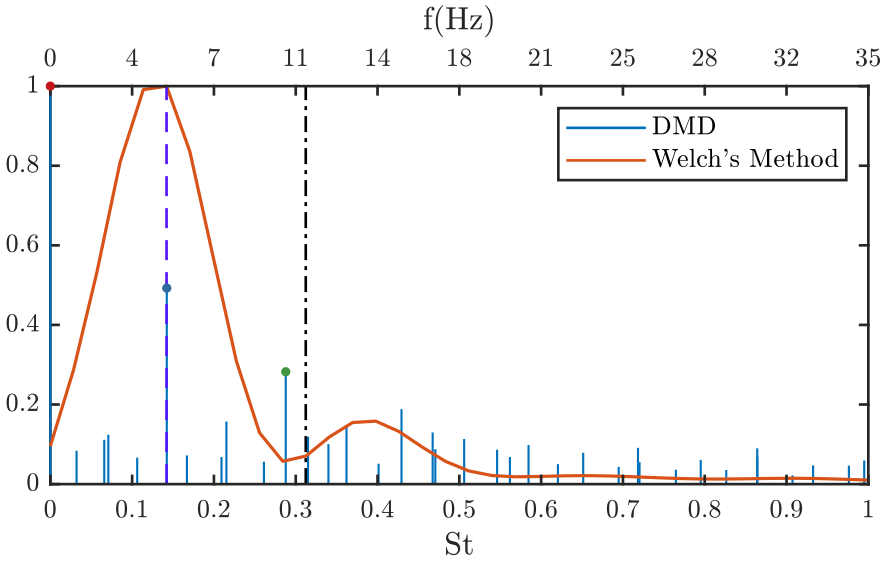

(a)

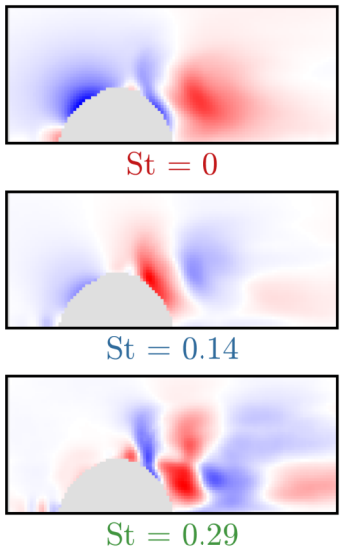

(b)

Figure 5.10: DMD spectrum (a) and modes (b) for the hemisphere in pulsatile flow for $St_f/St_0 = 0.5$.

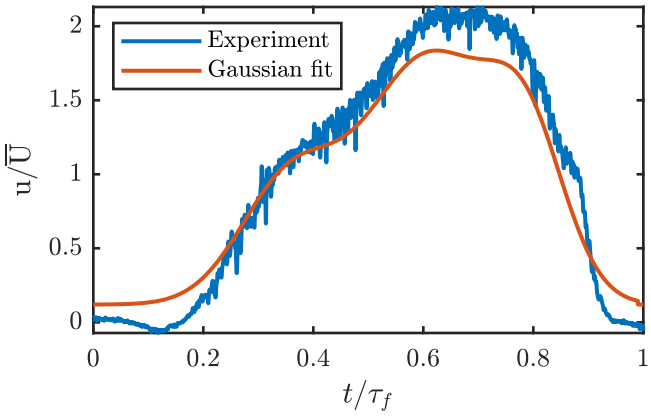

Figure 5.11: Fitted pulsatile forcing profile, $St_f/St_0 = 0.05$.

In order to accurately scale time, a relation for the instantaneous Reynolds number was required. Thus, as a precursor to the time-scaling analysis, a moving average filter was applied to the forcing profile shown in Fig. 5.3 to remove high-frequency measurement noise, then a fourth-order Gaussian of the form

$$u(t) = \sum_{i=1}^{4} a_i e^{-\left(\frac{t-b_i}{c_i}\right)^2} \tag{5.1}$$

was fit to the pulsatile forcing profile. A Gaussian fit was used as it accurately captured the flat tails in the forcing profile near $t/\tau_f \approx 0$ and 1. The fitted profile, corresponding to $R^2 = 0.993$, is shown in Fig. 5.11. It is noted that the highly pulsatile forcing profile led to a significant contraction and dilation of $\tilde{t}$. Because time was scaled by re-sampling the data a posteriori, as outlined in Section 2.4.3, high pulsatility could lead to poor re-sampling from an insufficient number of snapshots near the extrema of the forcing cycle. Consequently, the amplitude of the fitted profile was slightly decreased to improve scaling performance, hence the small defect between the experimental and fitted forcing profiles shown in Fig. 5.11.

In order to use the time-scaling framework presented in Section 2.4, a relation for the shedding frequency as a function of Reynolds number is required. A simple equation for the variation of St with Re_R was developed by considering the data from Tamai et al. (1987) shown in Fig. 5.2. Fitting a power-law to the data from Tamai et al. (1987) for the corresponding range of Reynolds numbers results in the the desired relation, $St(Re) = 0.0142Re^{0.4554}$, also shown in Fig. 5.12.

The resulting power-law and forcing profile are used to compute the quasisteadiness, $\Omega(t)$, and scaled time, $\tilde{t}$, corresponding to the pulsatile forcing cycle (Fig. 5.11). It

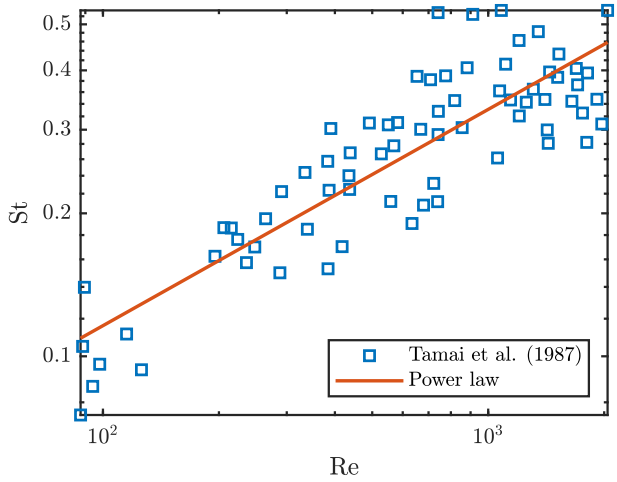

Figure 5.12: Power-law fit to data from Tamai et al. (1987).

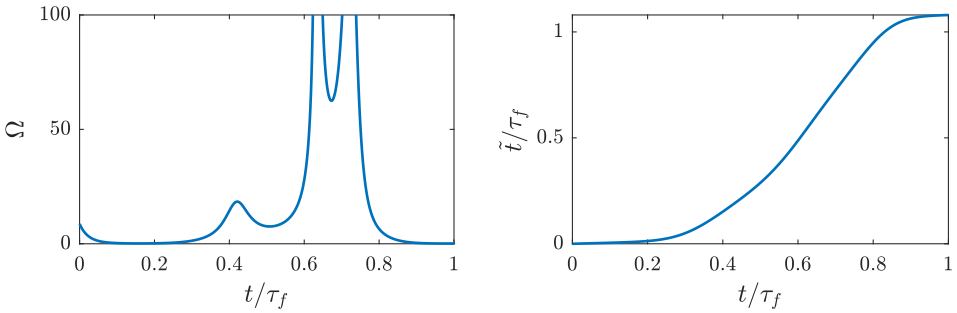

Figure 5.13: Quasisteadiness, Ω, and scaled time, $\tilde{t}$, computed for pulsatile forcing cycle shown in Fig. 5.11, $St_f/St_0 = 0.05$.

can be seen that the quasisteadiness, shown in Fig. 5.13, increases near $t/\tau_f \approx 0.4$ and displays a strong peak at $t/\tau \approx 0.75$ where $\Omega \gg 1$. As outlined in Section 2.4, portions of the forcing cycle where $\Omega \gg 1$ are indicative of quasi-steady behavior similar to the unforced case. Thus, this portion of the pulsatile forcing cycle corresponds to the regime most likely to exhibit hairpin shedding and wake dynamics similar to the steady flow case. Both the snapshots shown in Fig. 5.4 and the time trace of velocity presented in Fig. 5.5 verify this notion. Furthermore, the minimum in Ω at $t/\tau_f \approx 0.2$, alluding to unsteady dynamics, corresponds to the portion of the forcing cycle where hairpin shedding is replaced by the upstream motion of the rear arch vortex.

Given that the pulsatile forcing cycle permits regions of quasi-steady shedding similar to the non-pulsatile case, time scaling can be used to transform the system and reduce complexity. Thus, time is scaled according to the methodology outlined

in Section 2.4. The variation of scaled time, $\tilde{t}$, along the pulsatile forcing profile is shown in Fig. 5.13. In contrast to the unscaled system which exhibits frequency-modulated shedding and highly unsteady arch vortex dynamics, the scaled system is dominated by the shedding of hairpin vortices. This is highlighted by the time trace of velocity in the wake of the scaled system, shown in Fig. 5.14. Specifically, the time trace shows a contraction in the unsteady segment of the forcing cycle resulting in an effective reduction in the effect of the rear arch vortex.

Further analysis of the scaled system elucidates the effect of time scaling on frequency-modulated shedding. Both the local and global (DMD) spectra of the scaled system, presented in Fig. 5.15a, contain a peak at the unforced shedding frequency. Furthermore, the peak in the DMD spectrum consists of hairpin shedding modes. This is in contrast to the unscaled case which contained shedding modes dispersed over a wide range of frequencies. The collapse of shedding modes onto a single spectral peak signals that hairpin shedding in the scaled system occurs at an approximately constant frequency. Because the spectral peak sits at the unforced shedding frequency, DMD of the scaled system holds more significance than its unscaled counterpart. Specifically, it shows that the dynamics of the hemisphere subject to pulsatile freestream forcing can indeed be related back to the unforced case, particularly in portions of the cycle where hairpin shedding is present. The collapse of shedding modes onto a single spectral peak also indicates that fewer modes are required to represent system dynamics, a byproduct of reduced system complexity. This also motivates categorization of dynamically significant modes and enables a path forward for the development of a reduced-order model in Section 5.5.

5.4 Sensor Placement

Analysis of the full flowfield around complex fluid-structure systems is often intractable in full-scale applications. As such, identification of dynamically significant regions of the flow that serve as good indicators of system behavior for analysis and reconstruction are invaluable. This section builds on this concept to identify optimal sensor locations in the wake of the surface-mounted hemisphere, both before and after time scaling.

The complexity induced by pulsatile forcing is evident in the broad range of spatio-temporal structures that develop in the wake. Dynamically significant flow structures are not localized in space but rather, different structures are seen in various regions of the flowfield. Examples include hairpin vortices, the rear arch vortex, and the

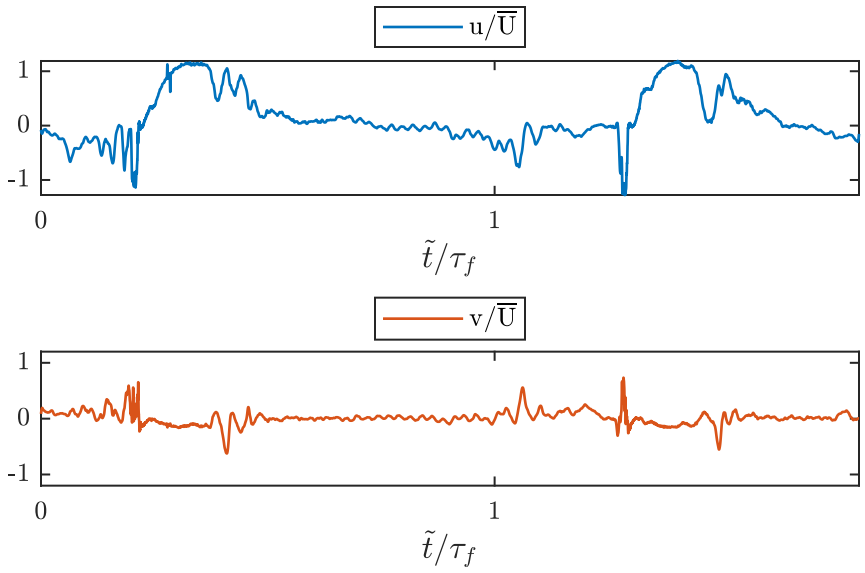

Figure 5.14: Time trace of velocity measured at interrogation point of scaled flowfield, $St_f/St_0 = 0.05$.

horseshoe vortex which all corresponded to different regions of the flowfield. In order to study the effect of time scaling on system complexity and identify regions of the flowfield representative of wake dynamics, data-driven sparse sensor placement is employed. In particular, the optimal set of sensor locations are computed for the flow, both before and after time scaling, using the methodology of Manohar et al. (2018), as outlined in Section 2.3.5. For a given number of sensors, the framework of Manohar et al. (2018) produces the optimal set of sensor locations for reconstruction. Hence, the resulting sensor positions serve as a good proxy to dynamically significant regions of the flowfield.

Sensor locations are presented for 20 sensors for pulsatile forcing at $St_f/St_0 = 0.05$. The leading 20 POD modes are used for sensor placement and account for 85% total energy contained in the system. Although the number of sensors can be increased, it was observed that the resulting position of additional sensors were approximately the same as the initial 20, albeit with slight variations. The resulting sensor locations for the unscaled case are shown in Fig. 5.16a. A rough approximation of the dynamic significance of each sensor location can be gained from the order in which sensors are placed. The numbers accompanying each sensor in Fig. 5.16a correspond to the order in which they were placed. In the unscaled system, approximately three quarters of the sensors reside in the wake. The clustering of sensors in the wake signals both its dynamic significance in the flowfield as well as its spatial complexity,

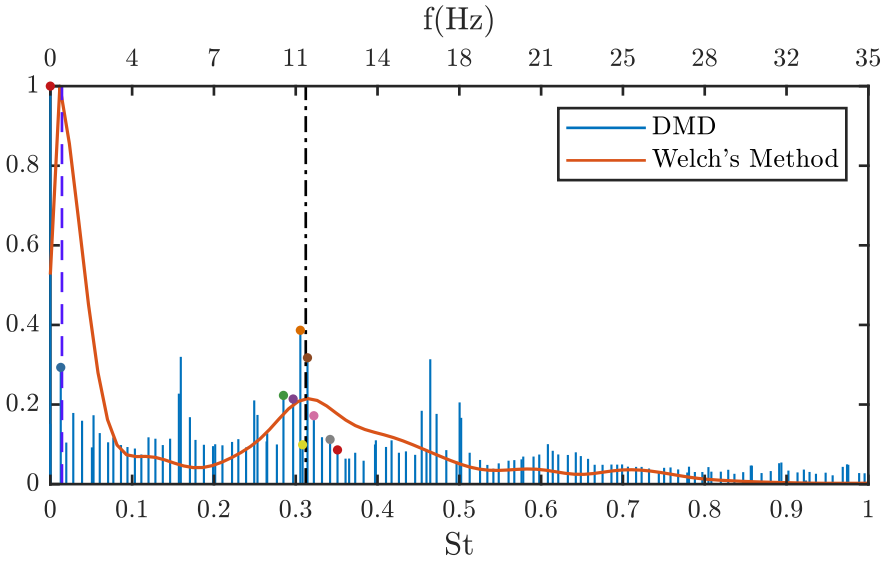

(a)

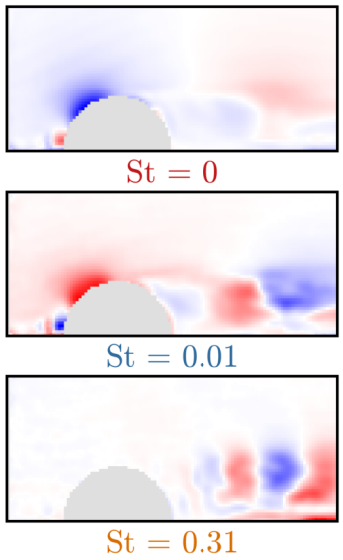

(b)

Figure 5.15: DMD spectrum (a) and modes (b) for the hemisphere in pulsatile flow under quasi-steady time scaling. $St_f/St_0 = 0.05$.

which mandates the use of additional sensors. Within the wake, there is a clustering of sensors near the top of the recirculation bubble, starting at sensor numbers 10 and 16. This can likely be attributed to the generation of hairpin vortices in that region.

Although the majority of sensors reside in the wake, multiple sensors are located elsewhere in the flow. Sensor 1 sits on the cylinder, above the leading stagnation point. The flow at this point is representative of the phase in the forcing cycle, which serves as a good measure of the transition between hairpin shedding and upstream motion of the rear arch vortex. Sensors 17 and 19, on the other hand, sit in the trajectory of the rear arch vortex as it moves upstream, and therefore capture its behavior as the freestream velocity reaches zero. The significant clustering of sensors in the wake tempts a reduction in the number of sensors, but the presence of numerous sensors in the other locations, such as sensors 17 and 19, promotes inclusion of all the sensors.

As opposed to the unscaled case, Fig. 5.16b shows that nearly all sensors are clustered in the wake. Consequently, no sensors are situated in the path of the rear arch vortex. The significance of sensors 15 and 16, located above the upstream stagnation point has also been reduced. This can be attributed to minimization of unsteady behavior phase-locked with the forcing. It is reiterated that time scaling was employed to achieve quasi-steady shedding and reduce unsteadiness. It should also be noted that time scaling increases the total energy contained in the 20 leading POD modes used in sensor placement to 89%. Furthermore, the clustering of nearly all the sensors in the wake after time scaling means the total number of sensors can likely be reduced, alluding to reduced system complexity.

Additional discussion is merited regarding the extrapolation of sensor locations to different forcing trajectories. The methodology used to compute sensor locations, namely that of Manohar et al. (2018), relies on a data-driven tailored basis, resulting in a greedy solution to the optimal sensor placement problem. Because the tailored basis is computed for a series of velocity fields corresponding to a specific forcing trajectory, meaningful extrapolation of sensor positions to different trajectories is not straightforward. In general, there is no guarantee that sensor locations would overlap for different forcing, but the time scaling framework provides some guidance in this regard. If different cases can all be scaled to resemble the same quasi-steady system, the resulting sensor locations after time scaling should be in good agreement. In this case, sensor locations computed after time scaling may also be relevant for quasi-steady regimes in other forcing trajectories (i.e. where $\Omega \gg 1$). The extrapolation

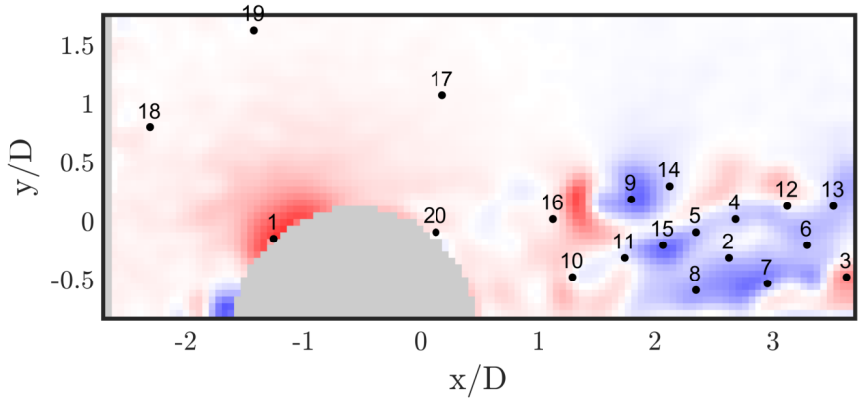

(a) Unscaled

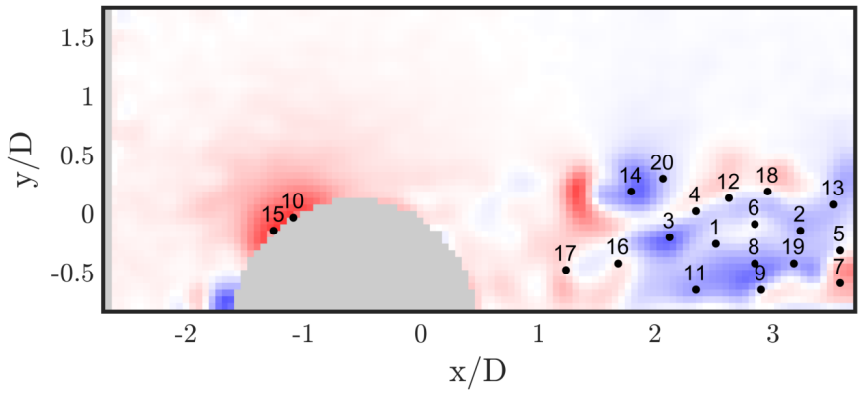

(b) Scaled

Figure 5.16: Sparse sensor placement in pulsatile flowfield, $St_f/St_0 = 0.05$.

of sensor locations to other forcing trajectories remains an open question and can be considered more in future work.

5.5 Flow Reconstruction

It was shown in Section 5.2 that freestream pulsatility corresponding to $St_f/St_0 = 0.05$ significantly alters wake dynamics, with particular attention placed on hairpin shedding. In addition, DMD of the wake, presented in Section 5.2.3, extracted shedding modes dispersed across a wide range of frequencies and produced a spectrum lacking a distinct spectral peak beyond the mean, alluding to hairpin shedding at more than one frequency. Consequently, a meaningful reconstruction that accurately captured shedding dynamics using only a small subset of modes was not straightforward. Time scaling was applied, however, to reduce system complexity and normalize the frequency associated with hairpin shedding, as attested to by the development of a spectral peak at the unforced shedding frequency. The scaled system facilitates a simple reconstruction of the flow that accurately captures the

observed shedding phenomena. Specifically, Eq. (2.10) can be used in conjunction with three DMD modes from the scaled system, namely, the mean, forcing, and peak shedding mode to generate a reduced-order model of the flow. After reconstruction relative to scaled time, $\tilde{t}$, the system is transformed back to lab time, t. A snapshot of the resulting reconstruction is shown in Fig. 5.17a at $t/\tau_f = 0.75$. At this phase in the cycle, the reconstruction exhibits frequency-modulated shedding, similar to experiments. Frequency-modulated shedding is particularly evident in the corresponding time trace of velocity, shown in Fig. 5.18a. Furthermore, Fig. 5.18a exhibits reduced oscillatory behavior when $t/\tau_f \approx 0.5$, also in good agreement with experiments. Although the shedding dynamics are satisfactorily represented in the reconstruction, the amplitude fluctuations observed in experiments are not captured by the reconstruction. Given that time scaling focused on hairpin shedding, a single shedding mode sufficed in the reconstruction. Even though DMD extracts a mode at the forcing frequency, the unsteady behavior exhibited by the arch vortex is not captured as well as the shedding. This likely results from the presence of additional vortical structures that ride on top of the rear arch vortex. Consequently, to model dynamics not associated with shedding, additional modes may be required. Similarly, footprints of shedding are present in the reconstruction at phases corresponding to motion of the arch vortex upstream. It should be reiterated that the analysis presented in this chapter primarily aimed to address hairpin shedding, which is still accurately captured by the reconstruction. Future work, however, can explore inclusion of additional modes in the reconstruction to account for this issue.

Reconstruction of the phase-locked system ($St_f/St_0 = 0.5$) is relatively straightforward. The presence of a strong spectral peak associated with the forcing frequency mitigates the need to scale time and motivates a choice of modes. A snapshot of the flow reconstructed using only the mean and forcing mode is shown in Fig. 5.17b. The reconstruction captures the phase-locked generation of the rear arch vortex. The trace of velocity in the wake, shown in Fig. 5.18b, also contains oscillations at the forcing frequency corresponding to the phase-locked behavior. The time trace does not contain the high-frequency fluctuations observed as small scale wake structures convect past the interrogation point. In order to replicate a larger range of spatial scales, future reconstructions can incorporate additional modes beyond the mean and forcing mode.

5.6 Chapter Summary and Outlook

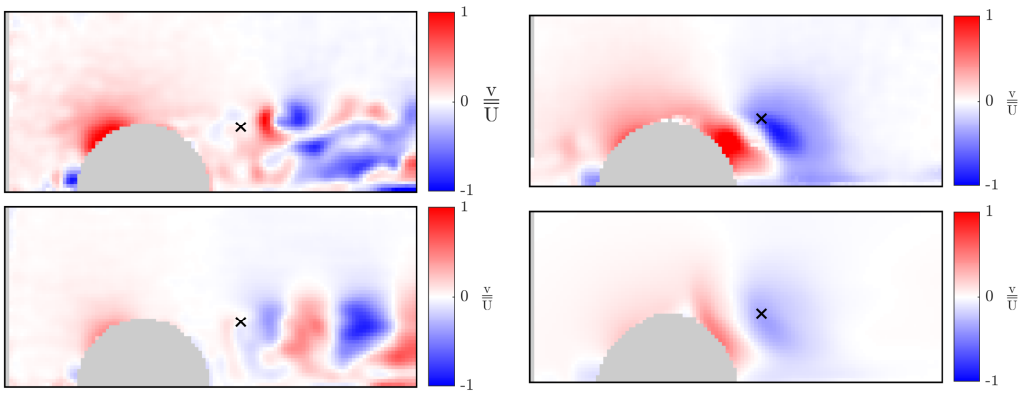

(a) $St_f/St_0 = 0.05$ (b) $St_f/St_0 = 0.5$

Figure 5.17: Snapshot of full flowfield (top) and flow reconstruction (bottom) using a small subset of DMD modes, $t/\tau_f = 0.75$.

In this chapter, the wake of the surface-mounted hemisphere was analyzed for the case corresponding to a highly pulsatile freestream. Whereas the unforced case sheds hairpins at a constant frequency, pulsatile forcing significantly altered wake dynamics and led to frequency-modulated shedding. In addition, an unsteady rear arch vortex developed at certain phases in the forcing cycle. The subsequent analysis aimed to reduce complexity associated with hairpin shedding, as it is an important phenomena also observed in the unforced system. To this end, quasi-steady time scaling was used to normalize the shedding frequency and reduce system complexity, resulting in a spectral peak at the unforced shedding frequency in the DMD spectrum. This facilitated the generation of a simple flow reconstruction to model the frequency-modulated shedding observed in the full system. In addition, sparse sensor placement after time scaling generated sensor locations in fewer dynamically significant regions of the flow, alluding to reduced system complexity.

It was shown that time scaling resulted in quasi-steady hairpin shedding and enabled comparison with the analogous unforced system. Furthermore, it facilitated the development of a reduced-order model that exhibited shedding analogous to the full system. Although the analysis performed here using a two-dimensional slice of the flowfield captured hairpin shedding in the wake, additional factors can be explored in future work to generate a reduced-order model that captures dynamics beyond the hairpins alone. For example, certain structures in the full flowfield, including the rear arch vortex, are highly three-dimensional. The presence of additional vortical structures associated with the rear arch vortex can introduce new time scales to the flow which are not accounted for when considering hairpins alone. Similarly,

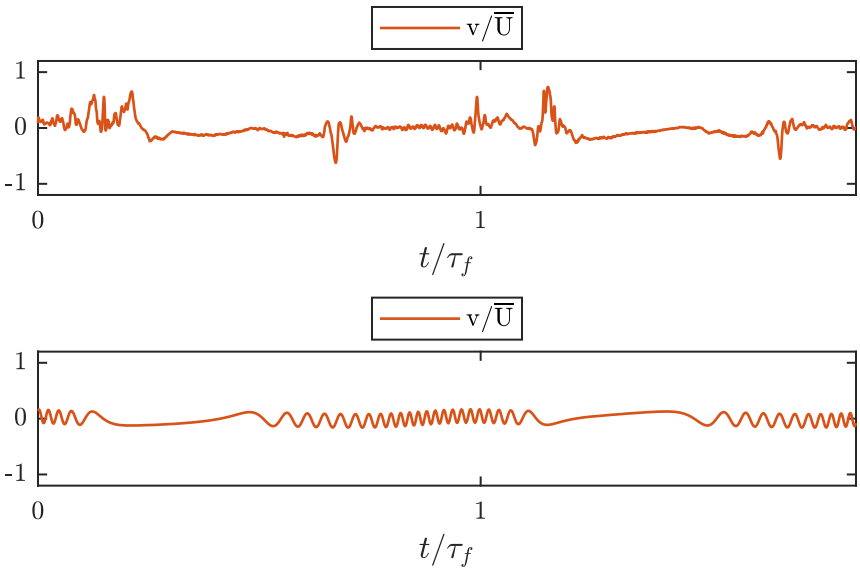

(a) $St_f\,/St_0 = 0.05$

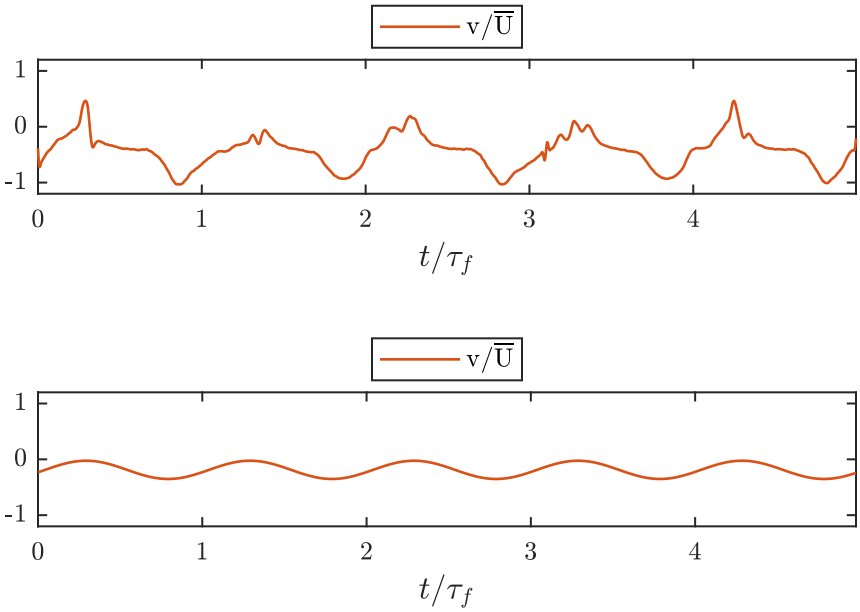

(b) $St_f\,/St_0 = 0.5$

Figure 5.18: Time trace of velocity measured at interrogation point in full flowfield (top) and flow reconstruction (bottom).

Acarlar and Smith (1987) note that multiple secondary flow instabilities can develop in the wake, leading to the generation of additional structures. While not considered here explicitly, these structures can include the development of secondary hairpins around the primary ones analyzed here. Thus, consideration of secondary and three-dimensional flow structures in future work could lead to a more comprehensive model of the system.

Chapter 6

CONCLUSION

The prevalence of fluid-structure interaction in the world around us warrants a deeper understanding of the underlying physics. To this end, the work in this thesis aimed to bridge the gap between forced and unforced fluid structure systems. In particular, the overlap between system dynamics, both with and without forcing, was explored, and a framework to reduce complexity was developed. The major findings and significant contributions of the research contained in this thesis are summarized below, followed by a brief overview of avenues forward in future work.

6.1 Summary

In Chapter 2, the experimental methods and analytical approach employed in the thesis were summarized. In particular, Dynamic Mode Decomposition (DMD), the primary modal analysis technique employed in the thesis, was outlined and the quasi-steady time scaling framework was developed. Within this framework, the quasisteadiness parameter, Ω, was presented. For a forced, periodic system, it was shown that $\Omega \gg 1$ alluded to slowly varying, quasi-steady dynamics while $\Omega \ll 1$ was a sign of unsteady behavior. If the system permitted development of quasi-steady dynamics, a time scaling was presented to transform the system and relate it to the analogous unforced system.

In Chapter 3, the wake of the streamwise-oscillating cylinder was analyzed for mean Reynolds number $Re_0 = 900$. Focus was placed on forcing frequencies considerably lower than the stationary vortex shedding frequency, a regime largely overlooked in previous studies. Forcing amplitudes were such that the instantaneous Reynolds number remained above the critical value at all times. Experimental flowfields showed the development of both amplitude and frequency modulation in the wake. Frequency modulation arose from modulated shedding due to the time-varying instantaneous Reynolds number and was evident from the DMD spectra which contained spatially similar shedding modes distributed over a range of frequencies. Furthermore, Welch's method showed the development of two spectral peaks as a result of the observed frequency modulation. Amplitude modulation, on the other hand, was shown to arise from symmetric reorganization of the wake. Dye flow visualization and phase-averaged velocity fields both highlighted the development of

two symmetric starting vortices at the downstream turnaround point. Consequently, vortex shedding and oscillatory behavior in the wake were suppressed at that phase in the forcing cycle.

Chapter 4 studied the effect of quasi-steady time scaling on the oscillating cylinder's wake. It was shown that peaks in Ω corresponded to segments of quasi-steady vortex shedding in the wake, similar to the stationary cylinder. It was also shown that the two dominant peaks observed in the interrogation point spectra corresponded to vortex shedding in regions of the forcing cycle corresponding to $\Omega \gg 1$. On the other hand, the generation of starting vortices and consequent reduction in oscillatory behavior overlapped with regions of the forcing cycle where $\Omega \ll 1$. Time scaling was used to transform the forced system such that resulting dynamics resembled the stationary case. The absence of frequency modulation resulted in a more meaningful Dynamic Mode Decomposition, alluding to reduced system complexity. As such, a simple flow reconstruction was achieved using the decomposition of the time-scaled system. It was shown that using only three DMD modes, the flow reconstruction exhibited frequency-modulated shedding similar to the full system.

The wake of a surface-mounted hemisphere subject to a highly pulsatile freestream was analyzed in Chapter 5. Flowfields corresponding to a nominal mean Reynolds number $\overline{Re}_R = 1000$ were considered at two forcing frequencies. Pulsatile forcing frequencies much lower than the unforced hairpin shedding frequency permitted the development of frequency-modulated hairpin shedding during various portions of the forcing cycle. This was verified from the extraction of multiple shedding modes over a range of frequencies using DMD. In contrast, when the forcing frequency was of the same order as the shedding frequency, DMD extracted a single, phase-locked structure in the wake, corresponding to the rear arch vortex characterized by Carr et al. (2020). Time scaling was employed to reduce system complexity associated with frequency-modulated hairpin shedding. In contrast to the unscaled case, time scaling resulted in the development of a spectral peak at the stationary shedding frequency. Analysis showed that the peak corresponded to hairpin shedding and thus motivated a path forward for flow reconstruction. A simple reconstruction using three DMD modes from the scaled system reproduced frequency-modulated hairpin shedding analogous to the full system.

6.2 Future Work

Multiple insights regarding the cylinder and hemisphere wakes were achieved in this thesis, yet there remain numerous open questions. In particular, the reduced system complexity achieved here considered two-dimensional flowfields. Future work can consider the reduction in system complexity for full, three-dimensional flowfields. This is particularly relevant for the surface-mounted hemisphere, which contains numerous three-dimensional flow structures in its wake. Beyond the consideration of three-dimensional effects on time scaling, the sampling strategy can also be studied. As outlined in Chapter 2, time scaling was achieved by re-sampling the time-series a posteriori. Future work can consider sampling, whether in experiment or simulation, at a constant rate relative to scaled time.

An additional path forward regards reduced-order modeling of time-scaled systems. It was shown that time scaling enabled the development of simple reduced-order flow reconstructions, but the inclusion of additional modes merits further study. This could lead to the development of a full dynamical model of the system that incorporates time scaling, an interesting question left for future work. In particular, a principled framework for mode selection and reconstruction after time scaling warrants additional attention. Such a framework could lead to the systematic development of robust reduced-order models used to guide both design and control of fluid-structure systems.

Although the work contained in this thesis focused on two specific fluid-structure systems, the quasi-steady time-scaling framework need not be limited to them. As such, future studies can apply the framework contained herein to reduce the complexity of other fluid-structure systems. A particularly interesting question regards systems with multiple characteristic frequencies where a “layered” time scaling approach could be employed. Furthermore, future analysis can expand beyond fluid-structure phenomena and could therefore also benefit other disciplines where forced periodic systems are observed.

BIBLIOGRAPHY

Acarlar, M. S. and Smith, C. R. (1987). "A study of hairpin vortices in a laminar boundary layer. Part 1. Hairpin vortices generated by a hemisphere protuberance". In: *Journal of Fluid Mechanics* 175, pp. 1–41. DOI: 10.1017/S0022112087000272.

Amman, O. H., Karman, T. von, and Woodruff, G. B. (1941). *The Failure of the Tacoma Narrows Bridge*. Technical Report.

Arbabi, H. and Mezic, I. (2017). "Study of dynamics in post-transient flows using Koopman mode decomposition". In: *Physical Review Fluids* 2 (12), p. 124402. DOI: https://doi.org/10.1103/PhysRevFluids.2.124402.

Barbi, C. et al. (1986). "Vortex shedding and lock-on of a circular cylinder in oscillatory flow". In: *Journal of Fluid Mechanics* 170, pp. 527–544.

Beal, D. et al. (2006). "Passive propulsion in vortex wakes". In: *Journal of Fluid Mechanics* 549, pp. 385–402. DOI: 10.1017/S0022112005007925.

Bouard, R. and Coutanceau, M. (1980). "The early stage of development of the wake behind an impulsively started cylinder for $40 < Re < 10^4$". In: *Journal of Fluid Mechanics* 101.3, pp. 583–607. DOI: 10.1017/S0022112080001814.

Carr, I. A. (Aug. 31, 2019). "Wake Dynamics of Surface-Mounted Obstacles in Highly Pulsatile Flow". Doctoral dissertation. George Washington University.

Carr, I. A. and Plesniak, M. W. (2016). "Three-dimensional flow separation over a surfacemounted hemisphere in pulsatile flow". In: *Experiments in Fluids* 57, pp. 1–9. DOI: 10.1007/s00348-015-2099-z.

Carr, I. A. et al. (2020). "Effects of highly pulsatile inflow frequency on surface-mounted bluff body wakes". In: *Journal of Fluid Mechanics* 904, A29. DOI: 10.1017/jfm.2020.659.

Chen, K. K., Tu, J. H., and Rowely, C. W. (2012). "Variants of Dynamic Mode Decomposition: Boundary Condition, Koopman, and Fourier Analyses". In: *Journal of Nonlinear Science* 22, pp. 887–915.

Corke, T. C. and Thomas, F. O. (2015). "Dynamic Stall in Pitching Airfoils: Aerodynamic Damping and Compressibility Effects". In: *Annual Review of Fluid Mechanics* 47.1, pp. 479–505. DOI: 10.1146/annurev-fluid-010814-013632.

Drmac, Z., Mezic, I., and Mohr, R. (2018). "Data Driven Modal Decompositions: Analysis and Enhancements". In: *SIAM Journal on Scientific Computing* 40, A2253–A2285.

Dunne, R. and McKeon, B. J. (2015). "Dynamic stall on a pitching and surging airfoil". In: *Experiments in Fluids* 56. DOI: https://doi.org/10.1007/s00348-015-2028-1.

Fey, U., König, M., and Eckelmann, H. (1998). "A new Strouhal-Reynolds number relationship for the circular cylinder in the range $47 < \mathrm{Re} < 2 \times 10^5$". In: *Physics of Fluids* 10.7, pp. 1547–1549. DOI: http://dx.doi.org/10.1063/1.869675.

Gharib, M. et al. (2006). "Optimal vortex formation as an index of cardiac health". In: *Proceedings of the National Academy of Sciences* 103.16, pp. 6305–6308. DOI: 10.1073/pnas.0600520103.

Glaz, B. et al. (2017). "Quasi-periodic intermittency in oscillating cylinder flow". In: *Journal of Fluid Mechanics* 828, pp. 680–707. DOI: https://doi.org/10.1017/jfm.2017.530.

Graftieaux, L., Michard, M., and Grosjean, N. (2001). "Combining PIV, POD and vortex identification algorithms for the study of unsteady turbulent swirling flows". In: *Measurement Science and Technology* 12.9, pp. 1422–1429. DOI: 10.1088/0957-0233/12/9/307.

Griffin, O. and Ramberg, S. (1976). "Vortex shedding from a cylinder vibrating in line with an incident uniform flow". In: *Journal of Fluid Mechanics* 75, pp. 257–271.

Hansen, A. C. and Butterfield, C. P. (1993). "Aerodynamics of Horizontal-Axis Wind Turbines". In: *Annual Review of Fluid Mechanics* 25.1, pp. 115–149. DOI: 10.1146/annurev.fl.25.010193.000555.

Haykin, S. (2001). "Communication Systems". In: New York, New York: John Wiley & Sons, pp. 107–111.

Jeon, D. and Gharib, M. (2004). "On the relationship between the vortex formation process and cylinder wake vortex patterns". In: *Journal of Fluid Mechanics* 519, pp. 161–181.

Konstantinidis, E., Dorogi, D., and Baranyi, L. (2020). "Resonance in vortex-induced in-line vibration at low Reynolds numbers". In: *Journal of Fluid Mechanics* 907, A34-1–A34-35. DOI: https://doi.org/10.1017/jfm.2020.850.

Koopman, B. O. (1931). "Hamiltonian Systems and Transformation in Hilbert Space". In: *Proceedings of the National Academy of Sciences* 17.

Leontini, J., Jacono, D., and Thompson, M. (2013). "Wake states and frequency selection of a streamwise oscillating cylinder". In: *Journal of Fluid Mechanics* 730, pp. 162–192.

Leontini, J., Jacono, D., and Thompson, M. (2011). "A numerical study of an inline oscillating cylinder in a freestream". In: *Journal of Fluid Mechanics* 688, pp. 551–568.

Manohar, K. et al. (2018). "Data-Driven Sparse Sensor Placement for Reconstruction: Demonstrating the Benefits of Exploiting Known Patterns". In: *IEEE Control Systems Magazine* 38.3, pp. 63–86. DOI: 10.1109/MCS.2018.2810460.

McCroskey, W. (1981). *The Phenomenon of Dynamic Stall*. Technical Memorandum. National Aeronautics and Space Administration.

McKeon, B. J. and Sharma, A. S. (2010). "A critical-layer framework for turbulent pipe flow". In: *Journal of Fluid Mechanics* 658, pp. 336–382. DOI: 10.1017/S002211201000176X.

Mezic, I. (2005). "Spectral Properties of Dynamical Systems, Model Reduction, and Decomposition". In: *Nonlinear Dynamics* 41, pp. 309–325.

Mittal, R., Erath, B. D., and Plesniak, M. W. (2013). "Fluid Dynamics of Human Phonation and Speech". In: *Annual Review of Fluid Mechanics* 45.1, pp. 437–467. DOI: 10.1146/annurev-fluid-011212-140636.

Rowley, C. W. and Dawson, S. T. (2017). "Model Reduction for Flow Analysis and Control". In: *Annual Review of Fluid Mechanics* 49, pp. 387–417.

Rowley, C. W. et al. (2009). "Spectral analysis of nonlinear flows". In: *Journal of Fluid Mechanics* 641, pp. 115–127. DOI: https://doi.org/10.1017/S0022112009992059.

Sane, S. P. and Dickinson, M. H. (2002). "The aerodynamic effects of wing rotation and a revised quasi-steady model of flapping flight". In: *Journal of Experimental Biology* 205.8, pp. 1087–1096. ISSN: 0022-0949. URL: https://jeb.biologists.org/content/205/8/1087.

Schmid, P. J. (2010). "Dynamic mode decomposition of numerical and experimental data". In: *Journal of Fluid Mechanics* 656, pp. 5–28. DOI: https://doi.org/10.1017/S0022112010001217.

Segel, L. A. and Slemrod, M. (1989). "The Quasi-Steady-State Assumption: A Case Study in Perturbation". In: *SIAM Review* 31.3, pp. 446–477. DOI: 10.1137/1031091.

Shamai, M., Dawson, S. T. M., Mezic, I., and McKeon, B. J. (2021). "Unsteady dynamics in the streamwise-oscillating cylinder wake for forcing frequencies below lock-on". In: *Physical Review Fluids*. DOI: 10.1103/PhysRevFluids.00.004700.

Simao Ferreira, C. J. et al. (2010). "Simulating dynamic stall in a two-dimensional vertical-axis wind turbine: verification and validation with particle image velocimetry data". In: *Wind Energy* 13.1, pp. 1–17. DOI: https://doi.org/10.1002/we.330.

Simpson, R. L. (2001). "Junction Flows". In: *Annual Review of Fluid Mechanics* 33.1, pp. 415–443. DOI: 10.1146/annurev.fluid.33.1.415.

Taira, K. et al. (2017). "Modal Analysis of Fluid Flows: An Overview". In: *AIAA Journal* 55.12, pp. 4013–4041.

Tamai, N., Asaeda, T., and Tanaka, N. (1987). "Vortex Structures Around a Hemispheric Hump". In: *Boundary-Layer Meteorology* 39, pp. 301–314. DOI: 10.1007/BF00116124.

Tinevez, J.-Y. (2019). *simpletracker - A simple particle tracking algorithm for MATLAB that can deal with gaps.* URL: https://github.com/tinevez/simpletracker.

Tu, J. H. et al. (2014). "On dynamic mode decomposition: Theory and applications". In: *Journal of Computational Dynamics* 1.2, pp. 391–421. DOI: http://dx.doi.org/10.3934/jcd.2014.1.391.

Van Atta, C. and Gharib, M. (1987). "Ordered and chaotic vortex streets behind circular cylinders at low Reynolds numbers". In: *Journal of Fluid Mechanics* 174, pp. 113–133. DOI: 10.1017/S0022112087000065.

Van Cutsem, T. and Vournas, C. (1998). "Voltage Stability of Electric Power Systems". In: New York, New York: Springer US, pp. 166–167.

Welch, P. (1967). "The use of fast Fourier transform for the estimation of power spectra: A method based on time averaging over short, modified periodograms". In: *IEEE Transactions on Audio and Electroacoustics* 15.2, pp. 70–73. DOI: 10.1109/TAU.1967.1161901.

Williamson, C. H. (1996). "Vortex Dynamics in the Cylinder Wake". In: *Annual Review of Fluid Mechanics* 28.1, pp. 477–539. DOI: 10.1146/annurev.fl.28.010196.002401.

Williamson, C. H. and Govardhan, R. (2004). "Vortex-Induced Vibrations". In: *Annual Review of Fluid Mechanics* 36, pp. 413–455. DOI: https://doi.org/10.1146/annurev.fluid.36.050802.122128.

Williamson, C. H. and Roshko, A. (1988). "Vortex Formation in the Wake of an Oscillating Cylinder". In: *Journal of Fluids and Structures* 2.7, pp. 351–381. DOI: https://doi.org/10.1016/S0889-9746(88)90058.